Combustion Simulations in Diesel Engines using Reduced Reaction Mechanisms

D I S S E R T A T I O N

submitted to the

Combined Faculties for the Natural Sciences and for Mathematics

of the Rupertus Carola University of Heidelberg, Germany

for the degree of

Doctor of Natural Sciences

presented by

Chrys Correa, M.S. (Chem. Eng.)

born in Bombay

Examiners: Prof. Dr. Dr. h.c. Jürgen Warnatz
Prof. Dr. Bernhard Schramm

Heidelberg, June 30, 2000

Interdisziplinäres Zentrum für Wissenschaftliches Rechnen
Ruprecht - Karls - Universität Heidelberg
2000

D I S S E R T A T I O N

submitted to the

Combined Faculties for the Natural Sciences and for Mathematics

of the Rupertus Carola University of

Heidelberg, Germany

for the degree of

Doctor of Natural Sciences

presented by

Chrys Correa, M.S. (Chem. Eng.)

born in Bombay

Heidelberg, June 30, 2000

Title

Combustion Simulations in Diesel Engines using Reduced Reaction Mechanisms

Examiners: Prof. Dr. Dr. h.c. Jürgen Warnatz
Prof. Dr. Bernhard Schramm

Summary

The simulation of combustion in internal combustion engines is important in order to make computer-aided design possible, and also to be able to predict pollutant formation and gain a better understanding of the coupling between the various physical and chemical processes. Accurate simulations of Diesel engines require models for the various processes, such as spray dynamics, ignition, chemistry, heat transfer, etc. as well as the interactions between them, such as chemistry-turbulence interactions, etc.

A standard finite-volume CFD (computational fluid dynamics) code, KIVA III, which is capable of simulating two-phase engine flows was used. KIVA solves the three-dimensional Navier-Stokes equations, which are Favre-averaged, with a k-ϵ turbulence model. The spray dynamics are handled using a discrete droplet model (DDM) along with sub-models for collision, breakup, evaporation, etc. Three areas were identified, where KIVA sub-models either do not exist, or are insufficiently detailed for pollutant formation prediction: ignition, chemistry and radiation heat transfer. New models were developed and implemented for these three processes, which contain more physics and chemistry than the previous models, but which are computationally within limits for simulating a three-dimensional engine.

Ignition modeling in Diesel engines is very important to identify the ignition delay and the location of auto-ignition. As soon as the fuel is injected into the engine, low-temperature reactions occur leading to the formation of a radical pool. The concentration of this radical pool then increases during the ignition delay period due to chain reactions, eventually leading to ignition. Ignition chemistry can be described by means of a detailed chemical mechanism, which however cannot be used in a practical engine simulation due to the large number of species involved. In this thesis, ignition was tracked by means of a representative species (here CO), whose concentration remains almost zero during the ignition period and which shows a sharp increase at ignition. The reaction rate of CO was obtained from the detailed mechanism as a function of a few variables. In order to use this approach in turbulent flows, the reaction rate was integrated over a presumed probability density function (pdf) to account for the interactions between chemistry and turbulence.

Chemistry models used in Diesel engines should be capable of predicting intermediate and minor species in order to accurately capture the flame propagation and predict pollutant formation. The intrinsic low-dimensional manifold (ILDM) method was used in this thesis. It is an automatic reduction of a detailed chemical mechanism based on a local time scale analysis. Here, chemical processes which are fast in comparison to the turbulent mixing time scale are assumed to be in dynamic equilibrium. This allows the chemistry to be expressed only in terms of a few progress variables. Here, with n-heptane as a model diesel fuel, a one-dimensional ILDM with the CO_2 concentration as the progress variable. This chemistry model was also combined with a presumed probability density function (pdf) method in order to enable its use in turbulent flames. NO_x and soot were identified as the main pollutants and were predicted using a Zeldovich model and a phenomenological two-equation model, respectively with the NO

and soot precursors obtained from the ILDM chemistry.

Radiation could be an important mode of heat transfer in diesel engines where the soot concentration is high. The six-dimensional radiative transfer equation (RTE) needs to be solved for the radiative intensity along with models describing the variation of the radiative properties (e.g., absorption coefficients) with wavelength. The radiative properties of the gases (CO_2 and H_2O) were described with a weighted sum of grey gases model (WSGGM), where the total emissivity of a non-grey gas is represented by the weighted sum of the emissivities of a small number of grey gases. The radiative properties of soot were described by a grey model. The RTE was solved using the discrete ordinates method (DOM), which involves solving the RTE in discrete directions to describe the angular dependence of the intensity. Turbulence-radiation interactions were described using a presumed pdf.

The ignition and chemistry models were implemented in KIVA and used to simulate the combustion in a Caterpillar Diesel engine, for which experimental data were available. Simulations were carried out for several injection timings. In all simulations, ignition was observed to occur at the edge of the spray, in the lean-to-stoichiometric region where the temperatures are higher. Thermal NO formation was seen in the stoichiometric region at high temperatures, while soot formation was seen in the richer region where the temperatures are low. Simulated pressure curves were compared to experimental data and showed good agreement. The mean NO at the end of the cycle was compared to experimental values and also showed reasonable agreement (a maximum deviation of about 20% was observed). The mean soot at the end of the cycle was strongly under-predicted due to the inability to identify the one-dimensional manifold in the rich region where the formation of soot precursors is dominant. The DOM radiation model was tested in a furnace with a known temperature and absorption coefficient distribution, and the wall fluxes were compared to analytical data. It was not used in the engine due to low quantities of soot predicted. Instead, an optically thin model along with the WSGGM was used in the engine and the radiative losses were seen to be negligible.

Contents

1 Introduction

Combustion processes are very important in our day-to-day lives and also in industrial processes. About 90% of our energy requirements (e.g., in electrical power generation, heating, chemical industry, etc.) is provided by combustion. In spite of this importance, the fundamental processes occurring in combustion and their interactions with each other are not completely understood. Commonly used fuels in the industry are hydrocarbons and coal. These fuels are not available in unlimited amounts, hence there exists a need to run combustion processes more economically. Additionally, there exists the need to optimize either the operating or the geometrical parameters of the process in order to minimize environmental risks, e.g., the emission of unburnt hydrocarbons which are carcinogenic.

Since the experimental design of complex practical combustion devices is difficult and expensive, numerical simulations provide an attractive alternative for practical design. Mathematical modeling of reactive flows has gained increasing importance in the last decades. A large variety of models describing the several processes occurring in combustion, e.g., chemistry, turbulence, etc. and a variety of numerical tools required to solve the underlying equation systems have been developed. The progress of computer technology has also made it possible to simulate these practical devices. Detailed models for physical processes, such as detailed chemical mechanisms or detailed transport, are possible either in laminar flames [1–3] or in turbulent flames with simple geometries [4]. However, in practical three-dimensional complex geometries, the use of very simplified models in order to keep the computational requirements affordable is common. These models usually represent simplified versions of the real physical processes, and hence their use requires the specification of several parameters. These parameters usually need to be adjusted for different applications, making the whole process empirical. The aim of this thesis is to develop and use models for physical processes which are more detailed and have more physics than commonly used models, but at the same time are computationally feasible for use in practical geometries.

Several practical flames are diffusion flames, i.e., the fuel and the oxidizer enter the combustion chamber separately. Liquid fuels are also common in internal combustion engines, aircraft motors, etc. In order to maximize the surface area per unit mass of the fuel, and thus increase the reaction rates, the liquid fuel is often injected under high pressures. Thus, combustion chambers where liquid fuel is directly injected into the chamber under high pressure are relatively common. These diffusion flames need to be modeled accurately in order to enable the use of the simulation results in practice.

Compression ignition engines are used in a variety of applications - automobile, truck, locomotive, marine, power generation, etc. Here, air alone is inducted into the cylinder, and load control is achieved by varying the amount of fuel injected. The operation of a typical compression ignition engine is illustrated in Figure 1.1. The compression ratio of Diesels is much higher than typical spark ignition engines, and is in the range of 12 to 24. Air at close to atmospheric pressure is inducted at bottom-dead-center (BDC) where the piston is in its lowest position, and compressed to a pressure of about 4

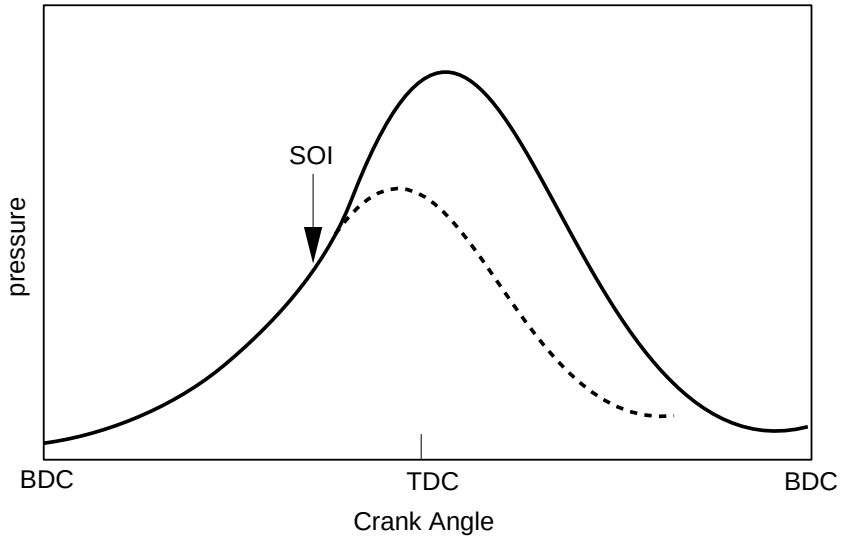

Figure 1.1: Cylinder pressure versus crank angle during compression, combustion and expansion in a typical Diesel cycle (solid line: firing cycle, dashed line: motored cycle)

MPa and temperature of about 800 K during the compression stroke. At about 20° before top-dead-center (TDC), where the piston is in its highest position, fuel injection commences (start of injection, SOI). The air temperature and pressure are above the fuels ignition point, and after a short delay period, spontaneous ignition of the mixture occurs, and the cylinder pressure (solid line in Figure 1.1) rises beyond the non-firing engine level (dashed line in Figure 1.1). The cylinder pressure then decreases due to expansion.

Internal combustion engines are generally more complex to model than other combustion chambers due to the following reasons:

- While most combustion processes occur at atmospheric pressure, very high pressures are present in engines.
- The presence of two phases, the liquid fuel phase and the gaseous phase, and the important interactions between them requires good models for both phases.
- Most flames do not involve ignition processes which are difficult to model.
- Most combustion chambers have no moving parts, unlike internal combustion engines, where the piston movement needs moving grids.

Most practical flames are turbulent due to the high velocities and large dimensions involved. Thus, the simulation of a general turbulent flame requires models for the different underlying processes involved, i.e., chemistry, turbulence, heat transfer through several modes (e.g. conduction, radiation), mass transfer through several modes (e.g., convection, diffusion), etc. and the complex interactions between the processes. All these processes are highly nonlinear and efficient numerical methods need to be used

in order to solve the underlying equations. Partial differential equations can be formulated for the balance of mass, momentum and energy. These form a non-linear, elliptical, coupled system of equations which can be solved with standard methods if all the length and time scales involved are resolved. Turbulent flows contain a large range of length scales, ranging from the largest scale dependent on the geometry of the system (the integral length scale) to the smallest scale (the Kolmogorov length scale). Resolving all these scales is possible, at present, only for a few low Reynolds-number systems [5]. However, these equations can be averaged and equations can be solved for averaged quantities.

The spray in the system is modeled by using a discrete particle method [6], where the probability distribution of the location, velocity, size and temperature of the droplets is solved for. This model accounts for the break-up, union and collision of the individual droplets. This phase is coupled with the gas phase through an exchange of mass, energy and momentum.

The prediction of the ignition location and its timing is especially important in Diesel engines as the flame propagation that follows is dependent on it. Auto-ignition results due to several low-temperature chain reactions which lead to the formation of a radical pool. The prediction of this radical pool formation without the use of empirical parameters is only possible with the help of detailed chemical mechanisms. In order to enable the use of such mechanisms in a three-dimensional computational fluid dynamics (CFD) program, the reaction rates were tabulated and a representative species was chosen to track the buildup of the radical pool.

Chemistry models in engines are usually simplified, e.g., with global reaction assumptions or equilibrium assumptions. These are computationally cheap, however they cannot accurately predict pollutant formation [7]. On the other hand, detailed chemical mechanisms have been found to show good agreement with experimental data in laminar flames [8]. However, these mechanisms involve many species and reactions and thus their use in three-dimensional turbulent flames is limited. In this thesis, a method called the intrinsic low-dimensional manifold (ILDM) [9,10] was used, which is an automatic reduction of a detailed chemical mechanism based on a local eigenvalue analysis. This method enables the prediction of major species as well as minor radicals using only a few progress variables.

The above mentioned averaging of the balance equations leads to unclosed terms in these equations. One of the most difficult terms to close is the chemical source term in the species equation. This term represents the interaction between chemistry and turbulence and can be closed using statistical methods. The presumed-pdf method [11] was employed in this work. Here, the shape of the probability density function (pdf) is assumed and the chemical source terms are then integrated over this pdf to give their mean.

A mode of heat transfer often neglected in combustion simulations is radiation. This could have an effect on the quantity of pollutants predicted, as pollutant formation is especially sensitive to the temperature. Radiation is difficult to model due to the six-dimensional integro-differential equation that needs to solved for the radiative intensity

distribution [12]. The discrete ordinates method [13] solves this problem by solving the equation in discrete directions. The radiative properties of the gases and the soot also need to be accurately modeled. Since detailed wavelength-dependent calculations are very expensive, a weighted sum of grey gases model (WSGGM) [14] was used, where the non-grey medium is replaced by a small number of grey media with constant absorption coefficients.

The aim of this thesis is to simulate a turbulent spray diffusion flame with pollutant formation in a realistic Diesel engine. For this, an existing three-dimensional code KIVA-III [6] with existing spray models was used. The above mentioned models were implemented and used to describe the ignition, chemistry, chemistry-turbulence interactions and radiation. The resulting code was tested with a direct-injection Diesel engine for five different injection timings. The turbulent flow with compression, fuel injection, spray dynamics, mixing, ignition, flame propagation with pollutant formation and heat transfer, and expansion was simulated and the results were compared with experimental data. On the basis of this comparison, the use of these models and the improvements required can be discussed.

Chapter 2 discusses the basic equations used for turbulent, reactive flows with sprays. Chapter 3 discusses the new ignition model, the chemistry model, the pdf model and the radiation model used. Chapter 4 discusses in brief the numerical methods used in KIVA and the coupling between the new models in Chapter 3 and the equations in Chapter 2. Chapter 5 presents results from the simulations and compares them with experimental data, and Chapter 6 presents conclusions and recommendations.

2 Equations for turbulent reactive flows with sprays

2.1 Gas-phase equations

The fluid flow in internal combustion engines is unsteady, turbulent and compressible. These flows can be mathematically described by the Navier- Stokes equations [15]. In these equations, it is assumed that equations of continuum mechanics are valid, which is valid when the smallest turbulent eddy is larger than the mean free length of the molecules [16]. These equations describe the balance of mass, energy, and momentum. A general balance equation for variable ϕ contains terms due to convection, diffusion, source terms and unsteady terms, and looks like

$$\underbrace{\partial(\rho\phi)/\partial t}_{Accumulation} + \underbrace{\mathrm{div}(\rho\vec{u}\phi)}_{Convection} = \underbrace{\mathrm{div}(\Gamma_\phi \,\mathrm{grad}\,\phi)}_{Diffusion} + \underbrace{S_\phi}_{Source} \quad , \tag{2.1}$$

where ρ is the density, $\vec{u}$ is the velocity vector, Γ_ϕ is the diffusion coefficient and S_ϕ is the source/sink term.

2.1.1 Species mass balance

The species balance equation in terms of the species density ρ_i is given by

$$\frac{\partial \rho_i}{\partial t} + \mathrm{div}(\rho_i \vec{u}) = \mathrm{div}(\rho D \,\mathrm{grad}(\frac{\rho_i}{\rho})) + \dot{\rho_i}^{\mathrm{C}} + \dot{\rho_i}^{\mathrm{S}} \quad , \tag{2.2}$$

where $\dot{\rho_i}^{\mathrm{C}}$ is the source term due to chemistry (see Section 2.5) and $\dot{\rho_i}^{\mathrm{S}}$ is the source term due to the spray (see Section 2.4). The spray source term applies only to the fuel (always species number 1 in KIVA). The diffusion coefficient Γ_ϕ has the form ρD here. It is assumed that all the species have equal diffusivities, given by

$$D = \frac{\mu}{\rho Sc} \quad , \tag{2.3}$$

where μ is the dynamic viscosity (see Section 2.3) and Sc is the Schmidt number (the dimensionless number describing the relationship between viscosity and diffusivity).

2.1.2 Total mass balance

Adding the species transport equations (Equation (2.2)) for all species, one gets the total mass balance equation. Since mass cannot be produced or destroyed in chemical reactions, the only source term is one due to the addition of the fuel spray:

$$\frac{\partial \rho}{\partial t} + \operatorname{div}(\rho \vec{u}) = \dot{\rho_1}^{\mathrm{S}} \ . \tag{2.4}$$

2.1.3 Momentum balance

A balance of momentum $m\vec{u}$ gives the equation

$$\frac{\partial (\rho \vec{u})}{\partial t} + \operatorname{div}(\rho \vec{u}\vec{u}) = \operatorname{div} \bar{\bar{\sigma}} - \operatorname{grad} p + \vec{F}^{\mathrm{S}} + \rho \vec{g} \ , \tag{2.5}$$

where p is the fluid pressure. The viscous stress tensor $\bar{\bar{\sigma}}$ for a Newtonian fluid is

$$\bar{\bar{\sigma}} = \mu[\operatorname{grad} u + (\operatorname{grad} u)^{\mathrm{T}}] - \frac{2}{3}\mu(\operatorname{div} \vec{u})\bar{\bar{I}} \ , \tag{2.6}$$

where the exponent T stands for the transpose and $\bar{\bar{I}}$ is the identity tensor. $\vec{F}^{\mathrm{S}}$ is the rate of momentum gain per unit volume due to the spray (see Section 2.4).

2.1.4 Energy balance

The equation for the specific internal energy E, excluding the heats of formation of the species involved, is

$$\frac{\partial (\rho E)}{\partial t} + \operatorname{div}(\rho \vec{u} E) = -p \operatorname{div}(\vec{u}) - \operatorname{div} \vec{J} + \rho\epsilon + \dot{Q}^{\mathrm{C}} + \dot{Q}^{\mathrm{S}} \ . \tag{2.7}$$

The heat flux vector $\vec{J}$ is the sum of contributions due to heat conduction and enthalpy diffusion,

$$J = -K \operatorname{grad} T - \rho D \sum_i h_i \operatorname{grad}(\rho_i/\rho) \ , \tag{2.8}$$

where T is the fluid temperature, K is the thermal conductivity and h_i is the specific enthalpy of species i. K is calculated from the Prandtl number Pr and the specific heat at constant pressure c_{p} using

$$K = \frac{\mu c_{\mathrm{p}}}{Pr} \ , \tag{2.9}$$

where the specific heat of the mixture is calculated using

$$c_{\mathrm{p}}(T) = \sum_i \frac{\rho_i}{\rho} c_{\mathrm{p}i}(T) \ . \tag{2.10}$$

The specific heats of the species $c_{\mathrm{p}i}$ as well as the specific enthalpies h_i in Equation (2.8) are obtained from the JANAF tables [17] as functions of temperature. The term $\rho\epsilon$ represents the energy source due to turbulence, where ϵ is the dissipation rate of the turbulent kinetic energy. Two source terms arise in Equation (2.7): $\dot{Q}^{\mathrm{C}}$ due to the chemistry (see Section 2.5) and $\dot{Q}^{\mathrm{S}}$ due to the spray (see Section 2.4).

2.1.5 State relations

The state relations are assumed to be of an ideal gas, giving equations for the temperature and the pressure as

$$T = \frac{1}{R_0} \sum_i M_i [h_i(T) - \frac{\rho_i}{\rho} E(T)] \ , \tag{2.11}$$

$$p = R_0 T \sum_i \frac{\rho_i}{M_i} \ , \tag{2.12}$$

where M_i is the molar mass of species i and R_0 is the ideal gas constant.

2.2 Averaging of the gas phase equations

The gas phase equations defined in Section 2.1 can be directly solved in a deterministic manner for all the unknowns. In order to do this, all the length and time scales involved need to be resolved. In turbulent flows, a number of length scales exist that characterize different aspects of the flow behavior. The integral length scale represents the largest length scale and is governed by the dimensions of the system (about 0.1 m in an engine). The smallest scales are limited by molecular diffusion and are about 10^{-5} m [7] in length. To resolve them, one needs about 10^4 mesh points in each direction, i.e. about 10^{12} points in the three-dimensional engine. The smallest time scales are of the order of 10^{-6} s and a complete combustion cycle lasts about 50 ms for a speed of 2000 rpm [18], so that about 50,000 time steps are required. About 5×10^4 floating-point operations are required at each time step at each mesh point. This means that 2.5×10^{21} operations are needed for the entire problem, which can take 350,000 CPU-years on a computer with 300 MFLOPS.

However, since we are only interested in the mean values and not in the instantaneous fluctuations, an averaging of the equations defined in Section 2.1 can be carried out by

splitting each variable into its mean and its fluctuating component and then averaging. Thus, statistical methods are used to describe the random flow. Several different types of averaging procedures are possible, e.g., time averaging, where the variable is averaged over a definite time interval,

$$\overline{\phi(t)} = \frac{1}{t - t_0} \int_{t_0}^{t} \phi(t') \mathrm{d}t' \ . \tag{2.13}$$

In engines, the application of these turbulence concepts is complicated by the fact that there are cycle-to-cycle variations in the mean flow at any point in the cycle, as well turbulent fluctuations about that specific cycles mean flow [7]. An approach used in such quasi-periodic flows is ensemble averaging, where the variable is averaged over several N_{cyc} cycles. This averaging process is performed at several crank angle locations to get the ensemble-averaged variable over the entire cycle,

$$\overline{\phi_{N_{\mathrm{cyc}}}} = \frac{1}{N_{\mathrm{cyc}}} \sum_{n=1}^{N_{\mathrm{cyc}}} \phi_n \ . \tag{2.14}$$

Figure 2.1 shows this approach applied to an engine with small and large cycle-to-cycle variations [7].

Thus, each variable can be split into its mean $\overline{\phi}$ and its fluctuation ϕ',

$$\phi = \overline{\phi} + \phi' \ . \tag{2.15}$$

The mean of the fluctuations ϕ' disappears using

$$\overline{\phi'} = 0 \ . \tag{2.16}$$

The mean of the square of the fluctuations is called the variance and can be calculated by

$$\overline{\phi'^2} = \overline{\phi^2} - \overline{\phi}^2 \ . \tag{2.17}$$

However, since large density variations are common in combustion processes due to large temperature differences, it is useful to introduce a density-weighted average, called the Favre average $\tilde{\phi}$, in order to avoid terms involving density fluctuations,

$$\tilde{\phi} = \frac{\overline{\rho\phi}}{\overline{\rho}} \ . \tag{2.18}$$

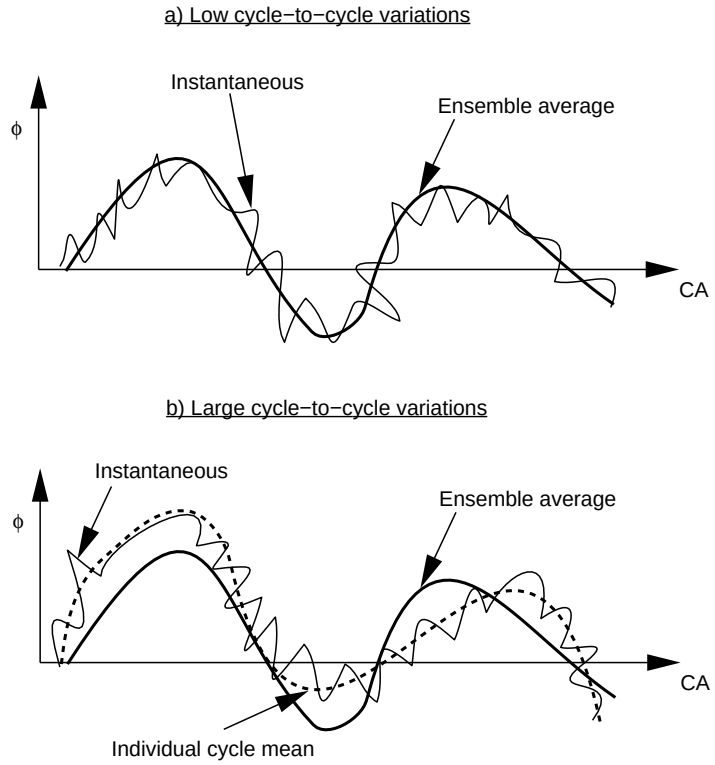

Figure 2.1: Ensemble averaging of variable ϕ as a function of the crank angle for a) Small cycle-to-cycle variations, and b) Large cycle-to-cycle variations [7]

Using Favre averaging, a variable ϕ can now be split into

$$\phi = \tilde{\phi} + \phi'' \ . \tag{2.19}$$

2.2.1 Favre-averaged equations

Substitution of equations (2.15) and (2.18) in the gas phase equations results in the Reynolds-averaged Navier Stokes equations (RANS), i.e., the Navier Stokes equations in terms of the Favre-averaged variables [19]:

Species mass balance (using $\rho_i = \rho Y_i$):

$$\frac{\partial \overline{\rho}\tilde{Y}_i}{\partial t} + \mathrm{div}(\overline{\rho}\tilde{\vec{u}}\tilde{Y}_i) = \mathrm{div}(\overline{\rho D \,\mathrm{grad}\, Y_i} - \overline{\rho \vec{u}'' Y_i''}) + \overline{\dot{\rho Y_i}^{\mathrm{C}}} + \overline{\dot{\rho Y_i}^{\mathrm{S}}} \tag{2.20}$$

Total mass balance:

$$\frac{\partial \overline{\rho}}{\partial t} + \mathrm{div}(\overline{\rho}\tilde{\vec{u}}) = \overline{\dot{\rho_i}^{\mathrm{S}}} \tag{2.21}$$

Momentum balance:

$$\frac{\partial(\overline{\rho}\tilde{\vec{u}})}{\partial t} + \operatorname{div}(\overline{\rho}\tilde{\vec{u}}\tilde{\vec{u}}) = \operatorname{div}(\bar{\bar{\sigma}} - \overline{\rho\vec{u}''\vec{u}''}) - \operatorname{grad}\tilde{p} + \overline{\vec{F}^{\mathrm{S}}} + \overline{\rho}\tilde{\vec{g}} \tag{2.22}$$

Energy balance:

$$\frac{\partial(\overline{\rho}\tilde{E})}{\partial t} + \operatorname{div}(\overline{\rho}\tilde{\vec{u}}\tilde{E}) = -\tilde{p}\operatorname{div}\tilde{\vec{u}} - \operatorname{div}(\overline{\vec{J}} + \overline{\rho\vec{u}''E''}) + \overline{\rho}\tilde{\epsilon} + \overline{\dot{Q}^{\mathrm{C}}} + \overline{\dot{Q}^{\mathrm{S}}} \tag{2.23}$$

State relations:

$$\tilde{T} = \frac{1}{R_0}\sum_i M_i[h_i(\tilde{T}) - \frac{\overline{\rho}_i}{\overline{\rho}}\tilde{E}(\tilde{T})] \tag{2.24}$$

$$\tilde{p} = \frac{\overline{\rho}R_0\tilde{T}}{\overline{M}} \ , \tag{2.25}$$

where the fluctuations in the mean molar mass M are neglected.

The above mean equations contain correlation terms in the form of $\overline{\rho\vec{u}''\phi''}$ which represent the effects of turbulent fluctuations. These new terms generated in the averaging process are not known explicitly as functions of the means, leading to more unknowns than equations (the closure problem in turbulence). These terms need to be modeled using turbulence models (see Section 2.3). The mean sources due to chemistry ($\rho\dot{\underline{Y}_i}^{\mathrm{C}}$ and $\underline{\dot{Q}^{\mathrm{C}}}$) are described in Sections 2.5 and 2.6. The mean sources due to the spray ($\dot{\rho}_i{}^{\mathrm{S}}$, $\vec{F}^{\mathrm{S}}$, $\dot{Q}^{\mathrm{S}}$) are defined in Section 2.4.

2.3 Turbulence models

In order to solve the closure problem, models which describe $\overline{\rho\vec{u}''\phi''}$ in terms of the mean variables are needed. The eddy-viscosity concept [20] is the most commonly used basis for turbulence models. Here, $\overline{\rho\vec{u}''\phi''}$ is interpreted as turbulent transport and is modeled analogous to laminar transport, i.e., by analogy with Fick's law, it is proportional to the gradient of the mean value of the property, but with a turbulent exchange coefficient. The Reynolds stress terms ($\overline{\rho\vec{u}''\vec{u}''}$) in Equation (2.22) is thus,

$$\overline{\rho\vec{u}''\vec{u}''} = -\overline{\rho}\nu_{\mathrm{T}}\operatorname{grad}\tilde{\vec{u}} \ , \tag{2.26}$$

where ν_{T} is the turbulent (or eddy) viscosity.

For the turbulent transport of the scalar quantities (term $\overline{\rho\vec{u}''Y_i''}$ in Equation (2.20), and term $\overline{\rho\vec{u}''E''}$ in Equation (2.23)), an analogous logic is used,

$$\overline{\rho\vec{u}''\phi''} = -\Gamma_{\phi,\mathrm{T}}\operatorname{grad}\tilde{\phi} \ , \tag{2.27}$$

where $\Gamma_{\phi,\mathrm{T}}$ is the turbulent exchange coefficient of ϕ. For mass transfer, $\Gamma_{Y_i,\mathrm{T}} = \overline{\rho} D_\mathrm{T}$, with the turbulent diffusion coefficient D_T given by $D_\mathrm{T} = \mu_\mathrm{T}/(\overline{\rho} Sc_\mathrm{T})$ where Sc_T is the turbulent Schmidt number. For energy transfer, the turbulent exchange coefficient $\Gamma_{E,\mathrm{T}} = K_\mathrm{T}/c_\mathrm{p}$, with the turbulent thermal conductivity K_T given by $K_\mathrm{T} = \mu_\mathrm{T} c_\mathrm{p}/Pr_\mathrm{T}$ where Pr_T is the turbulent Prandtl number.

Values for Sc_T and Pr_T usually used in internal combustion engines, and also in this thesis, are $Sc_\mathrm{T} = Pr_\mathrm{T} = 0.9$ [23].

As can be seen from the above equations, the only variable which is undefined is the turbulent viscosity μ_T. Several models exist with which μ_T can be calculated: algebraic models (e.g. the mixing length model [21]), one-equation models, two-equation models [24], Reynolds-stress models [22], etc. Only one two-equation model, the k-ϵ model, used in this thesis will be described here.

2.3.1 The k-ϵ turbulence model

Two-equation models use two partial differential equations for the determination of the turbulent viscosity. In the standard k-ϵ model, equations are solved for the turbulent kinetic energy $\tilde{k}$ and its dissipation rate $\tilde{\epsilon}$ [20, 24]. These are related to the primitive variables through

$$\tilde{k} = \frac{1}{2}\widetilde{u''^2} \tag{2.28}$$

and

$$\tilde{\epsilon} = \nu \overline{\operatorname{grad} \vec{u}''^{\mathrm{T}} : \operatorname{grad} \vec{u}''} \ , \tag{2.29}$$

where $\nu = \mu/\rho$ is the laminar viscosity. The turbulent viscosity can then be calculated using the Prandtl-Kolmogorov equation,

$$\nu_T = C_\nu \frac{\tilde{k}^2}{\tilde{\epsilon}} \ , \tag{2.30}$$

where C_ν is an empirically determined constant ($C_\nu = 0.09$).

The equation for $\tilde{k}$ can be mathematically derived from the momentum balance equation using Equations (2.22) and (2.28) [25] giving

$$\frac{\partial(\overline{\rho}\tilde{k})}{\partial t} + \operatorname{div}(\overline{\rho}\tilde{\vec{u}}\tilde{k}) = -\frac{2}{3}\overline{\rho}\tilde{k} \operatorname{div} \tilde{\vec{u}} + \tilde{\bar{\bar{\sigma}}} : \operatorname{grad} \tilde{\vec{u}} + \operatorname{div}\left(\frac{\mu_\mathrm{eff}}{Pr_\mathrm{k}} \operatorname{grad} \tilde{k}\right) - \overline{\rho}\tilde{\epsilon} + \overline{\dot{W}^\mathrm{S}} \ , \tag{2.31}$$

Constant	c_{ϵ_1}	c_{ϵ_2}	c_{ϵ_3}	c_{s}	Pr_{k}	Pr_{ϵ}
Value	1.44	1.92	-1.0	1.5	1.0	1.3

Table 2.1: Values of the k-ϵ model constants

where μ_{eff} is the effective dynamic viscosity and is the sum of the laminar and the turbulent dynamic viscosities, i.e. $\mu_{\mathrm{eff}} = \mu_{\mathrm{L}} + \mu_{\mathrm{T}}$.

The equation for $\tilde{\epsilon}$ follows from analogous assumptions and is

$$\frac{\partial(\overline{\rho}\tilde{\epsilon})}{\partial t} + \operatorname{div}(\overline{\rho}\tilde{\vec{u}}\tilde{\epsilon}) = -\left(\frac{2}{3}c_{\epsilon_1} - c_{\epsilon_3}\right)\overline{\rho}\tilde{\epsilon}\operatorname{div}\tilde{\vec{u}} + \operatorname{div}\left(\frac{\mu_{\mathrm{eff}}}{Pr_{\epsilon}}\operatorname{grad}\tilde{\epsilon}\right) + \frac{\tilde{\epsilon}}{\tilde{k}}\left(c_{\epsilon_1}\tilde{\overline{\sigma}} : \operatorname{grad}\tilde{\vec{u}} - c_{\epsilon_2}\overline{\rho}\tilde{\epsilon} + c_{\mathrm{s}}\overline{\dot{W}^{\mathrm{S}}}\right) \ . \tag{2.32}$$

Equations (2.31) and (2.32) are the standard k-ϵ equations with some added terms. The extra terms are those containing $\overline{\dot{W}^{\mathrm{S}}}$ which account for the spray interactions (defined in Section 2.4), and the term $(\frac{2}{3}c_{\epsilon_1} - c_{\epsilon_3})\overline{\rho}\tilde{\epsilon}\operatorname{div}\tilde{\vec{u}}$ in Equation (2.32) which accounts for length scale changes when there is velocity dilation [6]. The quantities c_{ϵ_1}, c_{ϵ_2}, c_{ϵ_3}, c_{s}, Pr_{k} and Pr_{ϵ} are constants whose values are determined from experiments and some theoretical considerations. Standard values of these constants are listed in Table 2.1 [6].

The k-ϵ model has a few drawbacks. The constants in the model depend on the geometry and the flow considered and the gradient transport assumption (Equation 2.26) is not theoretically sound. It is also unable to deal with strongly swirling flows and has been shown to be inferior to Reynolds stress models in engines [26]. However, the Reynolds stress model [22] in its basic form requires the solution of seven partial differential equations for the six stress components and the dissipation rate ϵ. This imposes a much larger computing burden compared with the two-equation k-ϵ model.

2.4 Spray modeling

The engine cylinder pressure at injection is typically in the range of 50 to 100 atm, while fuel injection pressures in the range of 200 to 1700 atm are used. These large pressure differences across the injector nozzle are required so that the liquid fuel jet enters the combustion chamber at a sufficiently high velocity to atomize into small-sized droplets to enable rapid evaporation and so that the droplets can traverse the combustion chamber in the time available [7]. The fuel spray produces an inhomogeneous fuel-air mixture, the spray interacts and strongly affects the flow patterns and temperature distribution in the cylinder. The fuel is injected as a liquid, it atomizes into a large number of small droplets with a wide spectrum of sizes, the droplets disperse and vaporize as the spray moves through the surrounding air, droplet coalescence and

separation can occur, gaseous mixing of fuel vapor and air then takes place, followed finally by combustion [7].

Spray models explicitly treat the two-phase structure of the spray. Two such classes of models exist, the continuum droplet model (CDM) and the discrete droplet model (DDM). The CDM attempts to represent the motion of all droplets via an Eulerian partial differential spray probability equation.The DDM uses a statistical approach; a representative sample of individual droplets, each droplet being a member of a group of identical non-interacting droplets termed a "parcel", is tracked in a Lagrangian fashion from its origin at the injector. A DDM is used for the spray in KIVA. Droplet parcels are introduced continuously throughout the fuel injection process, with specified initial conditions of position, size, velocity, number of droplets prescribed with an assumed distribution, initial spray angle and temperature. They are then tracked in a Lagrangian fashion through the computational mesh.

2.4.1 Spray equations

The spray is represented by a Monte Carlo-based discrete particle technique [27, 28]. Here, the spray is described by a droplet probability distribution function f. Each discrete droplet represents a group or parcel of droplets. f has ten independent variables in addition to time:

- The three spatial coordinates, $\vec{x}$
- The three velocity components, $\vec{v}$
- The equilibrium radius (the radius the droplet would have if it were spherical), r
- The temperature, T_d which is assumed to be uniform within the drop
- The distortion from sphericity, y, and
- The time rate of change, $\dot{y} = \mathrm{d}y/\mathrm{d}t$

The droplet distribution function f is defined in such a way that

$$f(\vec{x}, \vec{v}, r, T_\mathrm{d}, y, \dot{y}, t)\, \mathrm{d}\vec{v}\, \mathrm{d}r\, \mathrm{d}T_\mathrm{d}\, \mathrm{d}y\, \mathrm{d}\dot{y} \tag{2.33}$$

is the probable number of droplets per unit volume at position $\vec{x}$ and time t with velocities in the interval $(\vec{v}, \vec{v} + \mathrm{d}\vec{v})$, radii in the interval $(r, r + \mathrm{d}r)$, temperatures in the interval $(T_\mathrm{d}, T_\mathrm{d} + \mathrm{d}T_\mathrm{d})$, and displacement parameters in the intervals $(y, y + \mathrm{d}y)$ and $(\dot{y}, \dot{y} + \mathrm{d}\dot{y})$. The time evolution of f is obtained by solving a form of the spray equation [6]

$$\frac{\partial f}{\partial t} + \mathrm{div}_{\vec{x}}(f\vec{v}) + \mathrm{div}_{\vec{v}}(f\vec{F}) + \frac{\partial}{\partial r}(fR) + \frac{\partial}{\partial T_\mathrm{d}}(f\dot{T}_\mathrm{d}) + \frac{\partial}{\partial y}(f\dot{y}) + \frac{\partial}{\partial \dot{y}}(f\ddot{y}) = \dot{f}_\mathrm{coll} + \dot{f}_\mathrm{bu} \ . \tag{2.34}$$

The quantities F, R, $\dot{T}_\mathrm{d}$ and $\ddot{y}$ are the time rates of change, following an individual drop, of its velocity, radius, temperature and oscillation velocity respectively. The terms $\dot{f}_\mathrm{coll}$ and $\dot{f}_\mathrm{bu}$ are sources due to droplet collisions and breakups, defined in Section 2.4.2 and 2.4.3 respectively.

2.4.2 Collision

Two droplets (labeled 1 and 2) can collide only if they are in the same numerical mesh cell. Two types of collisions can be accounted for:

- The two droplets can coalesce to give a single droplet. In this case, the temperature and velocity of the new droplet is calculated using a mass averaging procedure. The new droplet size can be calculated from the droplet volume.
- No mass and energy transfer between the two droplets takes place. They maintain their sizes and temperatures, but undergo velocity changes.

In order to decide what type of collision takes place, a collision impact parameter, b is compared to the critical impact parameter, b_cr which is given by

$$b_\mathrm{cr} = \frac{1}{We}[(\frac{r_2}{r_1})^3 - 2.4(\frac{r_2}{r_1})^2 + 2.7(\frac{r_2}{r_1})] \ , \tag{2.35}$$

where the Weber number We is given by

$$We = \frac{\rho_\mathrm{d}|\vec{v}_1 - \vec{v}_2|r_1}{\alpha_\mathrm{d}(\overline{T}_\mathrm{d})} \quad \text{with} \quad \overline{T}_\mathrm{d} = \frac{{r_1}^3 T_{\mathrm{d}_1} + {r_2}^3 T_{\mathrm{d}_2}}{{r_1}^3 + {r_2}^3} \tag{2.36}$$

with ρ_d being the liquid density and α_d being the liquid surface tension coefficient. If $b < b_\mathrm{cr}$, then coalescence takes place. Thus, a collision probability density function σ can be obtained which gives the probable number of droplets resulting from a collision between droplet 1 and 2 [29],

$$\begin{aligned}\sigma =& \frac{{b_\mathrm{cr}}^2}{(r_1+r_2)^2}\delta[r - ({r_1}^3 + {r_2}^3)^{\frac{1}{3}}]\delta[\vec{v} - \frac{{r_1}^3\vec{v}_1 + {r_2}^3\vec{v}_2}{{r_1}^3 + {r_2}^3}]\delta[T_\mathrm{d} - \overline{T}_\mathrm{d}]\delta(y - y_2)\delta(\dot{y} - \dot{y}_2) \\ &+ \frac{2}{(r_1+r_2)^2}\int_{b_\mathrm{cr}}^{r_1+r_2}[\delta(r - r_1)\delta(\vec{v} - \vec{v_1})\delta(T_\mathrm{d} - T_{\mathrm{d}_1})\delta(y - y_1)\delta(\dot{y} - \dot{y}_1) \\ &+ \delta(r - r_2)\delta(\vec{v} - \vec{v_2})\delta(T_\mathrm{d} - T_{\mathrm{d}_1})\delta(y - y_2)\delta(\dot{y} - \dot{y}_2)]\, b\, \mathrm{d}b\end{aligned} \tag{2.37}$$

with

$$\hat{\vec{v}_1} = \frac{{r_1}^3\vec{v}_1 + {r_2}^3\vec{v}_2 + {r_2}^3(\vec{v}_1 - \vec{v}_2)\frac{b-b_{\mathrm{cr}}}{(r_1+r_2-b_{\mathrm{cr}})}}{{r_1}^3 + {r_2}^3}$$

and

$$\hat{\vec{v}_2} = \frac{{r_1}^3\vec{v}_1 + {r_2}^3\vec{v}_2 + {r_1}^3(\vec{v}_2 - \vec{v}_1)\frac{b-b_{\mathrm{cr}}}{(r_1+r_2-b_{\mathrm{cr}})}}{{r_1}^3 + {r_2}^3} \quad .$$

The source term due to collisions in Equation (2.34) is now given by

$$\begin{aligned}\dot{f}_{\mathrm{coll}} =& \frac{1}{2}\int\int f(\vec{x},\vec{v}_1,r_1,T_{\mathrm{d}_1},y_1,\dot{y}_1,t) f(\vec{x},\vec{v}_2,r_2,T_{\mathrm{d}_2},y_2,\dot{y}_2,t)\pi(r_1+r_2)^2|\vec{v}_1-\vec{v}_2| \\ & [\sigma(\vec{v},r,T_{\mathrm{d}},y,\dot{y},\vec{v_1},r_1,T_{\mathrm{d}_1},y_1,\dot{y}_1,\vec{v_2},r_2,T_{\mathrm{d}_2},y_2,\dot{y}_2) \\ & -\delta(\vec{v}-\vec{v}_1)\delta(r-r_1)\delta(T_{\mathrm{d}}-T_{\mathrm{d}_1})\delta(y-y_1)\delta(\dot{y}-\dot{y}_1)] \\ & -\delta(\vec{v}-\vec{v}_2)\delta(r-r_2)\delta(T_{\mathrm{d}}-T_{\mathrm{d}_2})\delta(y-y_2)\delta(\dot{y}-\dot{y}_2) \\ & \mathrm{d}\vec{v}_1\,\mathrm{d}r_1\,\mathrm{d}T_{\mathrm{d}_1}\,\mathrm{d}y_1\,\mathrm{d}\dot{y}_1\,\mathrm{d}\vec{v}_2\,\mathrm{d}r_2\,\mathrm{d}T_{\mathrm{d}_2}\,\mathrm{d}y_2\,\mathrm{d}\dot{y}_2 \quad . \end{aligned} \tag{2.38}$$

The above equations imply that droplets with large differences in radius or velocity have a larger probability of collision.

2.4.3 Breakup

Under Diesel engine injection conditions, the fuel jet usually forms a cone-shaped spray at the nozzle exit. This type of behavior is classified as the atomization breakup regime, and it produces droplets with sizes much less than the nozzle exit diameter. Breakup results from the unstable growth of surface waves caused by the relative motion between the liquid and the surrounding air [7]. Thus, the injected drop's size decreases with time due to breakup and new droplets are added to the computation which can further undergo breakup. The size of the product drops is determined from the wavelength of unstable waves on the surface of the droplet. The primary droplet breakup is described by a Kelvin-Helmholtz (KH) wave model [30]. Liquid breakup is modeled by postulating that new drops are formed (with drop radius r_{c}) from a parent drop (with radius r) with

$$r_{\mathrm{c}} = B_0 \Lambda_{\mathrm{KH}} \quad , \tag{2.39}$$

where B_0 is a constant ($B_0 = 0.61$), and Λ_{KH} is the wavelength corresponding to the frequency of the fastest growing KH wave, Ω_{KH}. The Ω_{KH} and Λ_{KH} values are given by a curve fit using

$$\Omega_{\mathrm{KH}} = \frac{0.34 + 0.38\,We^{1.5}}{(1+Z)(1+1.4\,Ta^{0.6})}\sqrt{\frac{\sigma}{\rho_{\mathrm{l}} r^3}} \tag{2.40}$$

$$\Lambda_{\mathrm{KH}} = \frac{9.02r(1+0.45\sqrt{Z})(1+0.4\,Ta^{0.7})}{(1+0.865\,We^{1.67})^{0.6}} \tag{2.41}$$

where $We = \rho {u_{\mathrm{r}}}^2 r/\sigma$ is the Weber number for the gas, $Z = \sqrt{We_{\mathrm{l}}}/Re_{\mathrm{l}}$ is the Ohnesorge number and $Ta = Z\sqrt{We}$ is the Taylor number. u_{r} is the magnitude of the relative velocity, We_{l} is the liquid Weber number which is similar to We except that the liquid density is used, and $Re_{\mathrm{l}} = u_{\mathrm{r}} r \rho_{\mathrm{l}}/\mu_{\mathrm{l}}$ is the liquid Reynolds number.

The rate of change of drop radius due to breakup is given by [31]

$$\frac{\mathrm{d}r}{\mathrm{d}t} = \frac{r - r_{\mathrm{c}}}{\tau} \quad \text{with} \quad \tau = \frac{3.788 B_1 r}{\Omega \Lambda} \tag{2.42}$$

where B_1 is a breakup time constant and can take values between 10-60 [32]. A value of 10 was used in all the computations presented here. A new parcel containing product drops of size r_{c} is created and added to the computations when sufficient product drops have accumulated. This is done when the mass of the liquid to be removed from the parent reaches or exceeds 3 % of the average injected mass and if the number of product drops is greater than or equal to the number of parent drops. Following each breakup event, the product drops are given the same temperature, physical location and velocity magnitude in the direction of the parent, as the parent.

The probability function B of the broken droplets is [6]

$$B = g(r)\delta(T - T_{\mathrm{d_1}})\delta(y)\delta(\dot{y})\frac{1}{2\pi}\int \delta[\vec{v} - (\vec{v}_1 + \omega\vec{n})]\mathrm{d}\vec{n} \tag{2.43}$$

where $g(r)$ is the size distribution and ω is the magnitude of the velocity of the resulting droplets.

The breakup source term in Equation (2.34) is now

$$\dot{f}_{\mathrm{bu}} = \int f(\vec{x}, \vec{v}_1, r_1, T_{\mathrm{d_1}}, 1, \dot{y}_1, t)\dot{y}_1 B(\vec{v}_1, r, T_{\mathrm{d}}, \dot{y}_1, \vec{x}, t)\,\mathrm{d}\vec{v}_1\,\mathrm{d}r_1\,\mathrm{d}T_{\mathrm{d_1}}\,\mathrm{d}\dot{y}_1 \tag{2.44}$$

2.4.4 Evaporation

The injected liquid fuel, atomized into small drops near the nozzle exit to form a spray, must evaporate before it can mix with the air and burn. The fuel is at a lower

temperature than the compressed air it is injected into. As the droplet temperature increases due to heat transfer, the fuel vapor pressure increases and the evaporation rate increases. However, as the mass transfer rate away from the drop increases, the heat available to the drop to further increase the drop temperature, decreases, causing a decrease in the evaporation rate with time [7]. To quantify the fuel evaporation rate, a balance equation for the energy flux on the surface of the droplet is written, giving a differential equation for the droplet temperature T_d,

$$4\pi r^2 \dot{Q}_\mathrm{d} = \rho_\mathrm{d} \frac{4}{3}\pi r^3 c_\mathrm{pl} \dot{T}_\mathrm{d} - \rho_\mathrm{d} 4\pi r^2 R L(T_\mathrm{d}) \ , \tag{2.45}$$

where c_pl is the liquid specific heat, $L(T_\mathrm{d})$ is the latent heat of vaporization and $\dot{Q}_\mathrm{d}$ is the heat conduction rate to the droplet surface per unit area. Equation (2.45) is a statement that the energy conducted to the droplet either heats up the droplet or supplies heat for vaporization. The heat conduction rate $\dot{Q}_\mathrm{d}$ is given by the Ranz-Marshall correlation

$$\dot{Q}_\mathrm{d} = \frac{K_\mathrm{air}(\hat{T})(T - T_\mathrm{d})}{2r} Nu_\mathrm{d} \quad \text{with} \quad \hat{T} = \frac{2}{3}T_\mathrm{d} + \frac{1}{3}T \ . \tag{2.46}$$

Convection to the drop is represented by the Nusselt number Nu_d,

$$Nu_\mathrm{d} = (2 + 0.6 {Re_\mathrm{d}}^{\frac{1}{2}} {Pr_\mathrm{d}}^{\frac{1}{3}}) \frac{\ln(1 + B_\mathrm{d})}{B_\mathrm{d}} \ , \tag{2.47}$$

which can be calculated from the Reynolds number of the droplet Re_d,

$$Re_\mathrm{d} = \frac{2\rho|\vec{u} - \vec{u''} - \vec{v}|r}{\mu_\mathrm{air}(\hat{T})} \quad \text{with} \quad \mu_\mathrm{air}(\hat{T}) = \frac{A_1 \hat{T}^{\frac{3}{2}}}{\hat{T} + A_2} (A_1 = 1.457 \times 10^{-5}; A_2 = 110) \ , \tag{2.48}$$

from the Prandtl number of the droplet Pr_d,

$$Pr_\mathrm{d} = \frac{\mu_\mathrm{air}(\hat{T}) c_\mathrm{p}(\hat{T})}{K_\mathrm{air}(\hat{T})} \quad \text{with} \quad K_\mathrm{air}(\hat{T}) = \frac{K_1 \hat{T}^{\frac{3}{2}}}{\hat{T} + K_2} (K_1 = 252; A_2 = 200) \tag{2.49}$$

and from the Spalding transfer number Br_d,

$$Br_\mathrm{d} = \frac{{Y_1}^* - Y_1}{1 - {Y_1}^*} \ . \tag{2.50}$$

This represents the gradients at the droplet surface. Y_1 is the mass fraction of the fuel in the gas phase and $Y_1{}^*$ is the mass fraction on the surface (assuming equilibrium vapor pressure at the surface),

$$Y_1{}^*(T_\mathrm{d}) = \frac{M_1}{M_1 + M_0(\frac{p}{p_v(T_\mathrm{d})} - 1)} \ , \tag{2.51}$$

where M_1 is the molar mass of the fuel, M_0 the mean molar mass without the fuel and $p_v(T_\mathrm{d})$ the equilibrium vapor pressure. Thus, the heat conduction rate $\dot{Q}_\mathrm{d}$ can be calculated using Equation (2.46). In order to solve Equation (2.45), the latent heat of vaporization $L(T_\mathrm{d})$ is required and is obtained from

$$L(T_\mathrm{d}) = E_1(T_\mathrm{d}) + RT_\mathrm{d}/M_1 - E_\mathrm{l}(T_\mathrm{d}) - p_\mathrm{v}(T_\mathrm{d})/\rho_\mathrm{d} \ . \tag{2.52}$$

R represents here the rate of change of droplet radius, given by the Frossling correlation,

$$R = -\frac{(\rho D)_\mathrm{air}(\hat{T})}{2\rho_\mathrm{d} r} B_\mathrm{d} Sh_\mathrm{d} \ , \tag{2.53}$$

where the Sherwood number Sh_d is given by

$$Sh_\mathrm{d} = (2 + 0.6 {Re_\mathrm{d}}^{\frac{1}{2}} {Sc_\mathrm{d}}^{\frac{1}{3}}) \frac{\ln(1 + B_\mathrm{d})}{B_\mathrm{d}} \quad \text{with} \quad Sc_\mathrm{d} = \frac{\mu_\mathrm{air}(\hat{T})}{\rho D_\mathrm{air}(\hat{T})} \ . \tag{2.54}$$

2.4.5 Droplet acceleration

The droplet acceleration term F has contributions due to aerodynamic drag and gravitational force:

$$F = \frac{3}{8}\frac{\rho}{\rho_\mathrm{d}} \frac{|\vec{u} + \vec{u''} - \vec{v}|}{r} (\vec{u} + \vec{u''} - \vec{v}) C_\mathrm{D} + \vec{g} \ , \tag{2.55}$$

where the drag coefficient C_D is given by

$$\begin{aligned} C_\mathrm{D} &= \frac{24}{Re_\mathrm{d}}(1 + \frac{1}{6} {Re_\mathrm{d}}^{\frac{2}{3}}) \quad \text{for} \quad Re_\mathrm{d} < 1000 \\ &= 0.424 \quad \text{for} \quad Re_\mathrm{d} > 1000 \ . \end{aligned} \tag{2.56}$$

The gas turbulence velocity $\vec{u''}$ is obtained by assuming that each component follows a Gaussian distribution with mean square deviation $2/3k$, i.e.,

$$G(\vec{u''}) = (\frac{4}{3}\pi k)^{-\frac{3}{2}} e^{(-\frac{3|\vec{u''}|^2}{4k})} \quad . \tag{2.57}$$

2.4.6 Gas-spray interaction terms

The spray phase interacts with the gas phase equations defined in Sections 2.2.1 and 2.3 in the following manner:

$$\overline{\rho \dot{Y}_i^{\mathrm{S}}} = -\int f \rho_{\mathrm{d}} 4\pi r^2 R \, \mathrm{d}\vec{v} \, \mathrm{d}r \, \mathrm{d}T_{\mathrm{d}} \, \mathrm{d}y \, \mathrm{d}\dot{y} \quad ,$$

$$\overline{\vec{F}^{\mathrm{S}}} = -\int f \rho_{\mathrm{d}} (4/3\pi r^3 \vec{F} + 4\pi r^2 R \vec{v}) \, \mathrm{d}\vec{v} \, \mathrm{d}r \, \mathrm{d}T_{\mathrm{d}} \, \mathrm{d}y \, \mathrm{d}\dot{y} \quad ,$$

$$\overline{\dot{Q}^{\mathrm{S}}} = -\int f \rho_{\mathrm{d}} (4\pi r^2 R[E_{\mathrm{l}}(T_{\mathrm{d}}) + \frac{1}{2}(\vec{v} - \vec{u})^2 + \frac{4}{3}\pi r^3 [c_{\mathrm{pl}} \dot{T}_{\mathrm{d}} + \vec{F}(\vec{v} - \vec{u} - \vec{u''})]]) \mathrm{d}\vec{v} \mathrm{d}r \mathrm{d}T_{\mathrm{d}} \mathrm{d}y \mathrm{d}\dot{y} \quad ,$$

$$\overline{\dot{W}^{\mathrm{S}}} = -\int f \rho_{\mathrm{d}} \frac{4}{3}\pi r^3 \vec{F} \vec{u''} \, \mathrm{d}\vec{v} \, \mathrm{d}r \, \mathrm{d}T_{\mathrm{d}} \, \mathrm{d}y \, \mathrm{d}\dot{y} \quad . \tag{2.58}$$

2.5 Chemistry modeling

In numerical calculations of reacting flows, computer time and storage constraints place severe restrictions on the complexity of the reaction mechanism that can be incorporated. While it is feasible to include detailed chemical mechanisms for the combustion of hydrocarbon-air mixtures in one-dimensional and two-dimensional laminar flows [1,2], their use in not possible with current computational facilities in three-dimensional turbulent unsteady flows, like those found in engines. Accordingly, engine calculations have been traditionally done with highly simplified schemes [32–35]. Several chemistry models are available in the literature and only a few will be outlined here. The model actually used in this thesis will be presented in Chapter 3.2.

2.5.1 Detailed reaction mechanisms

Detailed reaction mechanisms describe the chemistry how it occurs on a molecular level (i.e. with elementary reactions). A general reaction set can be represented by

$$\sum_i a_{ir} x_i \rightleftharpoons \sum_i b_{ir} x_i \ , \tag{2.59}$$

where x_i represents one mole of species i, and a_{ir} and b_{ir} are integral stoichiometric coefficients for reaction r. Reaction r proceeds at a rate $\dot{\omega}_r$ given by

$$\dot{\omega}_r = k_{\mathrm{f}_r} \prod_i (\rho_i / M_i)^{a_{ir}} - k_{\mathrm{b}_r} \prod_i (\rho_i / M_i)^{b_{ir}} \ . \tag{2.60}$$

Here, the forward and backward reaction rates, k_{f_r} and k_{b_r} respectively are assumed to be of the generalized Arrhenius form.

$$\begin{aligned} k_{\mathrm{f}_r} &= A_{\mathrm{f}_r} T^{n_{\mathrm{f}_r}} \exp(\frac{-E_{\mathrm{f}_r}}{R_0 T}) \\ k_{\mathrm{b}_r} &= A_{\mathrm{b}_r} T^{n_{\mathrm{b}_r}} \exp(\frac{-E_{\mathrm{b}_r}}{R_0 T}) \ , \end{aligned} \tag{2.61}$$

where A is the pre-exponential factor, n is the temperature exponent and E is the activation energy. The source terms in the un-averaged species equation (Equation 2.2) and in the un-averaged energy equation (Equation 2.7) can now be defined as:

$$\begin{aligned} \dot{\rho_i}^{\mathrm{C}} &= M_i \sum_r (b_{ir} - a_{ir}) \dot{\omega}_r \ , \\ \dot{Q}^{\mathrm{C}} &= \sum_r \dot{\omega}_r \sum_i (a_{ir} - b_{ir}) (\Delta {h_{\mathrm{f}}}^0)_i \ , \end{aligned} \tag{2.62}$$

where $(\Delta {h_{\mathrm{f}}}^0)_i$ is the standard heat of formation of species i.

This concept has many advantages: The reaction order is always constant and can be determined easily by looking at the molecularity of the reaction. Thus, rate laws can always be specified for elementary reaction mechanisms. If the reaction mechanism is composed of all the possible elementary reactions in the system, the mechanism is valid for all conditions (i.e. temperatures and mixture compositions). The parameters, such as A, n and E are obtained from experimental data [36, 38].

2.5.2 Global reaction mechanisms

Global reaction mechanisms simplify a detailed chemical mechanism into a mechanism containing a few non-elementary steps. The most common practice has been to assume that the combustion process

$$\begin{array}{ccccc} \text{Fuel} & + & \text{Oxidizer} & \longrightarrow & \text{Products} \\ \text{e.g., } \mathrm{C_7H_{16}} & + & 11\ \mathrm{O_2} & \longrightarrow & 7\ \mathrm{CO_2} + 8\ \mathrm{H_2O} \end{array}$$

can be represented by a single rate equation of an Arrhenius form [37]:

$$\begin{aligned} \frac{\mathrm{d[Fuel]}}{\mathrm{d}t} &= AT^n \mathrm{e}^{\frac{-E_\mathrm{A}}{R_0 T}} [\mathrm{Fuel}]^a [\mathrm{Oxidizer}]^b \\ \text{e.g., } \frac{\mathrm{d[C_7H_{16}]}}{\mathrm{d}t} &= 4.6 \times 10^{11} \mathrm{e}^{\frac{-15780\mathrm{K}}{T}} [\mathrm{C_7H_{16}}]^{0.25} [\mathrm{O_2}]^{1.5} \quad 1/\mathrm{s} \quad , \end{aligned} \tag{2.63}$$

where [Fuel] and [Oxidizer] denote mass fractions of the fuel and oxidizer respectively, A is the pre-exponential factor, n is the temperature exponent and E_A is the activation energy. Since the above reaction is non-elementary, these constants have no evident physical meaning and are usually obtained by matching experimental results. This approach has a few major problems [7]:

- The assumption that the complex hydrocarbon fuel oxidation process can be represented by a single overall reaction gives no information about the intermediate products which can be pollutant precursors.
- The parameters in Equation (2.63) need to be adjusted as the engine design and the parameters change.

Instead of only one global reaction, several global (non-elementary) reactions of the form Equation (2.63) can be used [32]. This however means that several sets of values of A, n and E_A need to be specified, which is mostly empirical. The source terms in the species and energy equations remain the same and are defined in Section 2.5.1.

2.5.3 Equilibrium chemistry

The chemistry can be greatly simplified if it is assumed that the species react to equilibrium as soon as they mix. With this assumption, all that remains to be described is how the fuel mixes with the oxidizer. The mixing problem is simplified by assuming that the diffusivities of all the scalars is that same. Since species are consumed or produced, it is better to track the mixing of elements since they are unchanged by chemical reaction. Hence, a mixture fraction ξ can be defined as

$$\xi = \frac{Z_i - Z_{i2}}{Z_{i1} - Z_{i2}} \ , \tag{2.64}$$

where Z_i denotes the mass fraction of element i, Z_{i1} and Z_{i2} being the mass fractions of element i in the fuel and the oxidizer streams respectively. A conservation equation for ξ can be written similar to Equation (2.1) and after Favre-averaging, one gets

$$\frac{\partial \overline{\rho}\tilde{\xi}}{\partial t} + \mathrm{div}(\overline{\rho}\tilde{\vec{u}}\tilde{\xi}) = \mathrm{div}(\overline{\rho} D_{\mathrm{T}} \,\mathrm{grad}\,\tilde{\xi}) + \overline{\rho\dot{\xi}^{\mathrm{S}}} \ , \tag{2.65}$$

where $\overline{\rho\dot{\xi}^{\mathrm{S}}}$ is the source term to the mixture fraction due to the spray. Equation (2.65) has no chemical source term as ξ is a conserved scalar. Defining ξ using Equation (2.64) with C as element i, the spray source can be defined as

$$\overline{\rho\dot{\xi}^{\mathrm{S}}} = \overline{\dot{\rho}^{\mathrm{S}}} Z_{\mathrm{C,fuel}} \ , \tag{2.66}$$

where $Z_{\mathrm{C,fuel}}$ is the mass fraction of element C in the fuel. For an adiabatic mixture, the enthalpy h is also a conserved scalar and is uniquely determined from ξ. In a non-adiabatic case (like an engine), all scalar variables are unique functions of the mixture fraction and the enthalpy, defined through the equilibrium relationship [38] (obtained by minimizing the Gibbs free energy of the mixture).

Since explicit rates are not available to calculate the chemical source terms in Equations (2.2) and (2.7), they are calculated as follows:

$$\begin{aligned} \dot{\rho}_i{}^{\mathrm{C}} &= (\rho_i{}^{\mathrm{eq}} - \rho_i{}^{\mathrm{old}})/\Delta t \\ \dot{Q}^{\mathrm{C}} &= -\sum_i \dot{\rho}_i{}^{\mathrm{C}} (\Delta h_{\mathrm{f}}{}^0)_i \end{aligned} \tag{2.67}$$

where $\rho_i{}^{\mathrm{eq}}$ is the equilibrium species density, $\rho_i{}^{\mathrm{old}}$ is the species density before chemistry and Δt is the CFD time step.

2.6 Chemistry-turbulence interactions

Section 2.5 described chemistry models which give the reaction rates and source terms for the un-averaged Navier-Stokes equations described in Section 2.1. Turbulent flows are however characterized by strong fluctuations in species concentrations, temperature, density, etc. Hence, here the Reynolds-averaged Navier-Stokes equations (see Section 2.2.1) need to be solved which require mean reaction rates and mean source terms. Mean reaction rates can be obtained in several ways.

2.6.1 Mean reaction rates using mean values

This approach is used in the original KIVA code. It simply calculates the mean reaction rate using mean values of concentrations and temperatures. This approach is valid if the source terms are linear functions of the concentrations and the temperatures. However, the non-linearity inherent in chemistry leads to large errors with this assumption. For

example, the simple case of a bi-molecular reaction between two species A and B (A + B $\longrightarrow$ Products), has reaction rates

$$\dot{\omega}_{\mathrm{A}} = \dot{\omega}_{\mathrm{B}} = -k_{\mathrm{c}} Y_{\mathrm{A}} Y_{\mathrm{B}} \tag{2.68}$$

assuming that k_{c} is a constant. The mean reaction rates are then

$$\overline{\dot{\omega}_{\mathrm{A}}} = -k_{\mathrm{c}} \overline{Y_{\mathrm{A}} Y_{\mathrm{B}}} = -k_{\mathrm{c}} \overline{Y}_{\mathrm{A}} \overline{Y}_{\mathrm{B}} - k_{\mathrm{c}} \overline{Y_{\mathrm{A}}' Y_{\mathrm{B}}'} \ . \tag{2.69}$$

If Y_{A} and Y_{B} are fluctuating in phase opposition, the relations $\overline{Y_{\mathrm{A}}' Y_{\mathrm{B}}'} < 0$ and $\overline{Y_{\mathrm{A}} Y_{\mathrm{B}}} < \overline{Y}_{\mathrm{A}} \overline{Y}_{\mathrm{B}}$ are true, while relations $\overline{Y_{\mathrm{A}}' Y_{\mathrm{B}}'} > 0$ and $\overline{Y_{\mathrm{A}} Y_{\mathrm{B}}} > \overline{Y}_{\mathrm{A}} \overline{Y}_{\mathrm{B}}$ hold if they are fluctuating in phase. In the limiting case shown in Figure 2.2, where $\overline{Y_{\mathrm{A}} Y_{\mathrm{B}}} = 0$ and $\overline{Y}_{\mathrm{A}}$ and $\overline{Y}_{\mathrm{B}} \neq 0$, the mean reaction rate is zero, although $\overline{Y}_{\mathrm{A}} \overline{Y}_{\mathrm{B}}$ is not zero, because the reaction cannot proceed if the reactants are not at the same place at the same time [39].

In the above example, k_{c} was considered constant. Temperature fluctuations also play an important role in combustion due to the actual nonlinear dependence of the rate constant on temperature through the Arrhenius equation (Equation (2.61)). Thus, $\overline{k_{\mathrm{c}}(T)}$ cannot be approximated by $k_{\mathrm{c}}(\overline{T})$. For periodic fluctuations, $\overline{k_{\mathrm{c}}(T)}$ has been shown to be significantly larger than $k_{\mathrm{c}}(\overline{T})$ [40].

2.6.2 Mean reaction rates using pdfs

A common approach to get the mean reaction rates is a statistical approach. Here, the fluctuations associated with a turbulent process are quantified in terms of a probability density function (pdf). In general, the reaction rate is a highly non-linear function of the temperature and scalar concentrations. In a turbulent-mixing flow, the temperature and scalar concentrations are random functions of space and time. Evaluation of the moments (e.g., the mean) of a non-linear function of several random variables requires

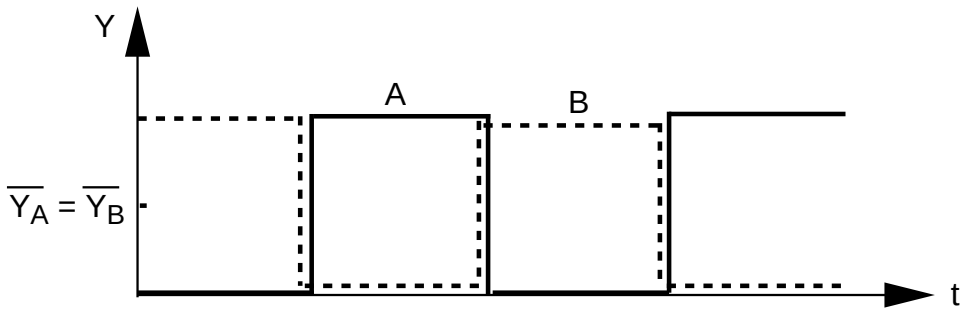

Figure 2.2: Hypothetical time behavior of A and B - Reaction is prevented due to fluctuations [39]

that the joint pdf of these variables is known. There are several ways of obtaining this pdf:

- The full pdf method [41–44] involves solving a transport equation either for the velocity-composition joint pdf or just the composition joint pdf. Monte-Carlo algorithms are usually used to solve this transport equation due to the large dimensionality of the joint pdf. The equation is an exact unclosed equation, where the chemical production term appears in exact and closed form. This is the main advantage of this approach. However, the molecular mixing term appears in unclosed term and requires modeling. As a consequence, it has been argued that the classical closure problem associated with turbulent combustion, which manifests itself as the mean reaction rate, is simply re-expressed in terms of the molecular mixing term in pdf closures [44]. Though theoretically sound, these methods require substantial computer resources, and the effort required to solve the transport equation is usually incommensurate with the information sought [45]. However, rapid progress has been made with the molecular mixing models, and this approach is very promising.

- Many combustion calculations adopt a simpler, less expensive approach. The functional form of the pdf is assumed *a priori*, and the parameters of such a presumed pdf are determined using the moments calculated from their respective transport equations [45]. For, e.g., an adiabatic flame, where equilibrium chemistry is used, the chemistry model is only a function of the mixture fraction (see Section 2.5.3). Thus, the mean reaction rate is given by

$$\tilde{\dot{\omega}} = \int \dot{\omega}(\xi)\tilde{P}(\xi)\mathrm{d}\xi \ . \tag{2.70}$$

  In the presumed pdf method, the shape of the pdf is assumed to be, e.g., Gaussian functions [46], beta functions [47] or Dirac-delta functions [48]. The parameters of the pdf are then calculated from the moments of the mixture fraction. The mean ($\tilde{\xi}$) is given by its transport equation (Equation (2.65)). In order to determine the pdf, the variance of the mixture fraction ($\widetilde{\xi''^2}$) is also needed, and is determined from its transport equation [18],

$$\frac{\partial \overline{\rho}\widetilde{\xi''^2}}{\partial t} + \mathrm{div}(\overline{\rho}\tilde{u}\widetilde{\xi''^2}) = \mathrm{div}(\overline{\rho}D_\mathrm{T}\,\mathrm{grad}\,\widetilde{\xi''^2}) + 2\overline{\rho}D_\mathrm{T}(\mathrm{grad}\,\tilde{\xi})^2 - 2\overline{\rho}\frac{\tilde{\epsilon}}{\tilde{k}}\widetilde{\xi''^2} + 2\overline{\rho}\widetilde{\xi''^2}\frac{\tilde{\dot{\xi}}_\mathrm{S}}{\tilde{\xi}} \ , \tag{2.71}$$

  where the last term accounts for the production of fluctuations due to the spray. This approach was used in this thesis, with the ILDM chemistry model (described in Section 3.2). The shape of the pdf used is described in Section 3.2.4.

3 Models for ignition, chemistry and radiation

3.1 Ignition

The original KIVA code does not have an ignition model, making it difficult to use for Diesel engine simulations. Since ignition is the starting process for combustion in Diesel engines, modeling ignition and accurately predicting the ignition location and timing is of essential importance. In ignition of hydrocarbon mixtures, a temperature increase, and thus an explosion, takes place after a certain induction time (ignition delay time). The ignition delay in a Diesel engine is defined as the time (or crank angle) interval between the start of ignition and the start of combustion. Both physical and chemical processes must take place before a significant fraction of the chemical energy of the injected liquid fuel is released. The physical processes are: atomization of the liquid fuel jet, vaporization of the fuel droplets and mixing of the fuel vapor with air. The chemical processes are the pre-combustion reactions of the fuel and air which lead to auto-ignition. The physical processes are described in Section 2.4 and representative models for the chemical processes need to be developed.

Auto-ignition (a rapid combustion reaction not initiated by an external ignition source) occurs when the energy released by the reaction as heat is larger than the heat lost to the surroundings; as a result the temperature of the mixture increases, thereby rapidly accelerating the rates of the reactions involved [7]. In complex reacting systems, the "reaction" is not a single- or even a few-step process; the actual chemical mechanism consists of a large number of simultaneous, interdependent chain reactions. During the ignition delay period, the radical pool population increases due to initiation, propagation and chain-branching reactions. The amount of fuel consumed, and hence the amount of heat liberated, is however too small to be detected. Thus, the temperature remains almost constant. When, due to chain-branching reactions, the number of radicals increases sufficiently rapidly, the reaction rate becomes extremely fast and a chain-branching explosion occurs.

3.1.1 Ignition chemistry

Detailed chemical mechanisms are usually available for pure hydrocarbons, and one for Diesel which is a blend of several hydrocarbons is difficult to define. The ignition quality of a fuel is defined by its cetane number. Since the cetane number of n-heptane (approximately 56) is similar to that of Diesel, heptane was used as the model fuel for Diesel. A detailed chemical mechanism containing 200 species involved in about 1200 elementary reactions was proven to accurately reproduce ignition delay times in a heptane-air mixture for a range of equivalence ratios [49] as shown in Figure 3.1.

The use of such mechanisms in a three-dimensional engine simulation is impractical, as transport equations similar to Equation (2.20) would have to solved for each of the 200 species. Hence, an ignition model is needed, which is based on such detailed mechanisms, but which can be easily and economically used in a practical simulation.

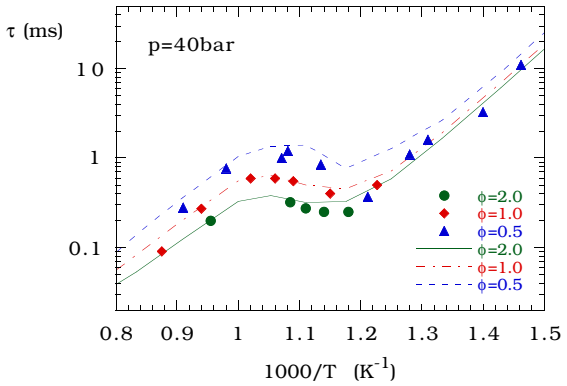

Figure 3.1: Comparison between calculations (lines) and experiments (symbols) of ignition delay times for a range of equivalence ratios ϕ [49]

One way to track the development of the radical pool is not to track all 200 species, but one representative species. This representative species should have the property of monotonically increasing till ignition and then showing a steep increase, so that ignition can be predicted. The species CO has been shown to possess these properties [49] as shown schematically in Figure 3.2.

For this representative species (CO), a transport equation needs to solved, which looks like

$$\frac{\partial \overline{\rho}\widetilde{Y_{\mathrm{CO}}}}{\partial t} + \mathrm{div}(\overline{\rho}\tilde{\vec{u}}\widetilde{Y_{\mathrm{CO}}}) = \mathrm{div}(\overline{\rho}D_{\mathrm{T}}\,\mathrm{grad}\,\widetilde{Y}_{\mathrm{CO}}) + \overline{\rho}\widetilde{\dot{Y}^{\mathrm{C}}_{\mathrm{CO}}} + \overline{\rho}\widetilde{\dot{Y}^{\mathrm{S}}_{\mathrm{CO}}}\ , \tag{3.1}$$

where $\widetilde{\dot{Y}^{\mathrm{C}}_{\mathrm{CO}}}$ and $\widetilde{\dot{Y}^{\mathrm{S}}_{\mathrm{CO}}}$ are the mean source terms due to the chemistry and spray, respectively. These need to be first defined, so that the transport equation (Equation (3.1)) can be solved. Later, an ignition criterion needs to be defined, which predicts the time of ignition.

The chemical source term for CO is obtained from the detailed chemical mechanism

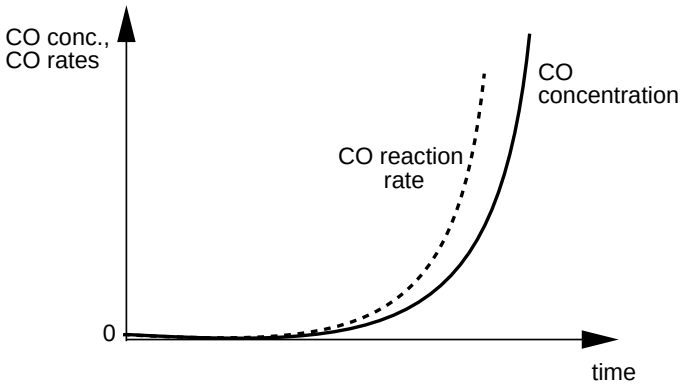

Figure 3.2: Schematic representation of the required properties of CO till ignition

consisting of 200 species and about 1200 elementary reactions. The reaction rates of CO are naturally dependent on the concentrations of all 200 species and on the temperature (due to the Arrhenius dependence of the rate constants). Thus, in a homogeneous, isothermal, isobaric reactor with a starting initial concentration of the 200 species (and thus a given mixture fraction ξ), the CO concentration and the CO reaction rates vary with time, as shown schematically in Figure 3.2. A change in perspective to eliminate the time as a coordinate results in CO reaction rates as a function of the CO concentration for a definite mixture fraction, pressure and temperature. The above isothermal, isobaric, homogeneous reactor calculations can be carried out for a range of mixture fractions, pressures and temperatures. The resulting results can be tabulated, which results in a table consisting of CO reaction rates ($\dot{C}^{\mathrm{C}}_{\mathrm{CO}} = \rho \dot{Y}^{\mathrm{C}}_{\mathrm{CO}}$) as a function of the CO concentration ($C_{\mathrm{CO}} = \rho Y_{\mathrm{CO}}$) for a range of mixture fractions (ξ), pressures (p) and temperatures (T). Thus, the laminar CO reaction rate, i.e. $\dot{C}^{\mathrm{C}}_{\mathrm{CO}}(\xi, T, p, C_{\mathrm{CO}})$ can be obtained. The ranges of ξ, p and T tabulated are based on physical considerations. Ignition usually takes place at pressures between 20 and 100 bar, at temperatures between 600 and 1300 K, and at mixture fractions between 0.025 and 0.5 (with 0.062 being stoichiometric). Hence, CO reaction rates as a function of C_{CO} (with C_{CO} ranging from 0 to 0.1 g/cm^3) are tabulated in this region.

3.1.2 Ignition in turbulent flames

In order to use the above defined rates in turbulent flows, the average reaction rates need to be defined. These can be obtained by averaging the laminar rates using probability density functions or pdfs (see Section 2.6.2). Thus, the mean CO reaction rate is

$$\widetilde{\dot{C}^{\mathrm{C}}_{\mathrm{CO}}} = \int \dot{C}^{\mathrm{C}}_{\mathrm{CO}}(\xi, T, p, C_{\mathrm{CO}}) \tilde{P}(\xi, T, p, C_{\mathrm{CO}}) \, \mathrm{d}\xi \, \mathrm{d}T \, \mathrm{d}p \, \mathrm{d}(C_{\mathrm{CO}}) \ . \tag{3.2}$$

Although the pressure in the cylinder changes with time, it is uniform in space and thus pressure fluctuations can be neglected [7]. Thus, a delta function for the pressure was used. The three dimensional pdf $\tilde{P}(\xi, T, C_{\mathrm{CO}})$ now needs to be specified. Although techniques to deal with multidimensional pdfs exist [52], they are not very suitable for complex systems, as their construction requires not only variances, but also covariances between all the variables. Hence, usually statistical independence of the variables is assumed [18]. This is a simplification which is not completely true as the CO concentration is dependent on the mixture fraction and the temperature. Assuming that ξ, T and C_{CO} are statistically independent, the three-dimensional pdf can now be split into the product of three one-dimensional pdfs,

$$\tilde{P}(\xi, T, C_{\mathrm{CO}}) = \tilde{P}(\xi) \, \tilde{P}(T) \, \tilde{P}(C_{\mathrm{CO}}) \ . \tag{3.3}$$

The shapes of the one-dimensional pdfs can now be assumed, and the pdfs can be constructed based on the mean moments. Several shapes of pdfs are possible, for

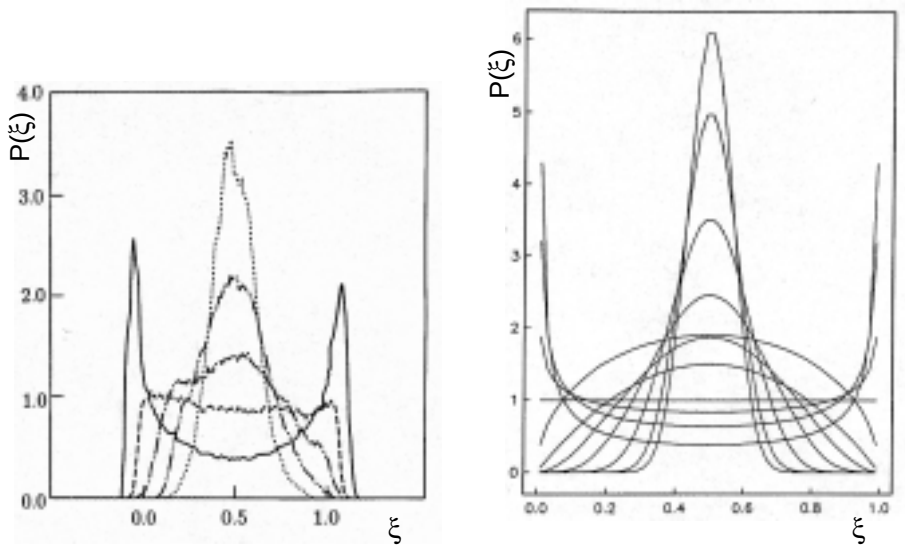

a) Exact pdf (DNS) b) Beta pdf

Figure 3.3: Evolution of the scalar pdf due to mixing a) With DNS data b) Calculated with a beta pdf [45]

e.g. Gaussian functions [46], beta functions [47] or Dirac-delta functions [48]. The choice of the shape of the pdf is arbitrary and does not have a large influence on the calculated means [45, 50, 51]. The scalar pdf has been known from experimental data and direct numerical simulations (DNS) to be Gaussian in the final stages of mixing [45]. However, during the early stages of mixing, the pdf is far from Gaussian and resembles a double-Dirac-delta function. For a case of two-scalar mixing where DNS results are available [53], the beta pdf has been shown to be extremely versatile depending on the value of the variance [45] as shown in Figure 3.3. In the initial stages of mixing (i.e. when the variance is large), the beta pdf resembles a double-Dirac-delta function. In the later stages of mixing (i.e. when the variance is small), the beta pdf resembles a Gaussian pdf in accordance with experimental results.

A beta pdf is also very convenient to use as its parameters are easily determined from the moments of the variable. The beta function of a given variable Z is defined in the interval [0;1] as

$$P(Z) = \gamma \cdot Z^{(a-1)} \cdot (1-Z)^{(b-1)} \quad \text{with} \quad \gamma = \frac{\Gamma(a+b)}{\Gamma(a)\Gamma(b)} \ , \tag{3.4}$$

where Γ denotes the Gamma function. Thus, only two parameters, a and b, need to be determined. The third parameter, γ is usually used as a normalization factor and is determined such that an essential property of the pdf, i.e.,

$$\int_0^1 P(Z)\mathrm{d}Z = 1 \tag{3.5}$$

is satisfied. The parameters, a and b, are determined from the mean ($\overline{Z}$) and variance ($\overline{Z''^2}$) of Z as [25]

$$b = \frac{\overline{Z}(1-\overline{Z})^2}{\overline{Z''^2}} + \overline{Z} - 1 \quad \text{and} \quad a = \frac{b\overline{Z}}{1-\overline{Z}} \ . \tag{3.6}$$

If the Favre mean ($\tilde{Z}$) and variance ($\widetilde{Z''^2}$) are used in the above definitions, the resulting pdf is the required Favre pdf $\tilde{P}(Z)$ [44].

The above method can easily be used to construct the pdf of the mixture fraction, $\tilde{P}(\xi)$, with the mean ($\tilde{\xi}$) and the variance ($\widetilde{\xi''^2}$) given by Equations (2.65) and (2.71) respectively. Also, the mixture fraction is physically defined in the interval [0;1] with 0 being pure air and 1 being pure fuel, making it possible to use beta functions.

In the case of the temperature and the CO concentration, these conditions are not fulfilled. In order to ensure that they are also defined in the interval [0;1], a normalization has to be carried out. This is done using the minimum and maximum values of T and C_{CO} present in the table (mentioned in Section 3.1.1). The means, $\tilde{T}$ and $\widetilde{C_{\mathrm{CO}}} = \overline{\rho}\widetilde{Y}_{\mathrm{CO}}$ are obtained from Equations (2.24) and (3.1) respectively. However, their variances are also required to construct their pdfs. A transport equation for the variance of C_{CO} ($\widetilde{\overline{\rho}Y''^2_{\mathrm{CO}}}$) can be written as [52]

$$\frac{\partial\widetilde{\overline{\rho}Y''^2_{\mathrm{CO}}}}{\partial t} + \mathrm{div}(\overline{\rho}\tilde{\vec{u}}\widetilde{Y''^2_{\mathrm{CO}}}) = \mathrm{div}(\overline{\rho}D_{\mathrm{T}}\,\mathrm{grad}\,\widetilde{Y''^2_{\mathrm{CO}}}) + 2\overline{\rho}D_{\mathrm{T}}(\mathrm{grad}\,\tilde{Y}_{\mathrm{CO}})^2 - 2\overline{\rho}\frac{\tilde{\epsilon}}{\tilde{k}}\widetilde{Y''^2_{\mathrm{CO}}} \ , \tag{3.7}$$

where the fluctuations in the source term have been neglected. Thus, the pdf of C_{CO} ($\tilde{P}(C_{\mathrm{CO}})$) can be constructed. The variance of the temperature is not very easy to solve for. For this, the variance of the internal energy equation needs to be solved for, which has many unclosed terms due to the chemistry source terms. Hence, it can be assumed that the intensity of turbulence is the same for the mixture fraction and the temperature [54], i.e.,

$$\frac{\widetilde{\xi''^2}}{\tilde{\xi}} = \frac{\widetilde{T''^2}}{\tilde{T}} \ , \tag{3.8}$$

from which the temperature variance, $\widetilde{T''^2}$ can be calculated. This approach assumes that the temperature behaves like a conserved scalar, which is not physically reasonable. However, in non-adiabatic, variable-pressure systems like engines, where the enthalpy

is not a unique function of the mixture fraction, a pdf integration over the temperature has to be carried out, and the above equation is an approximation for the variance.

Thus, all the three pdfs, $\tilde{P}(\xi)$, $\tilde{P}(T)$, $\tilde{P}(C_{\mathrm{CO}})$, can be constructed and the mean reaction can be obtained by integrating over the pdf, as in Equation (3.2).

3.1.3 Other ignition considerations

Sections 3.1.1 and 3.1.2 dealt with the mean chemical source term, $\overline{\rho}\widetilde{\dot{Y}^{\mathrm{C}}_{\mathrm{CO}}}$ in the CO transport equation (Equation (3.1)). Another source term present in this equation is the mean source term due to the spray, $\overline{\rho}\dot{Y}^{\mathrm{S}}_{\mathrm{CO}}$, which needs to be defined. Since the reaction rate of CO as a function of the CO concentration is obtained from trajectories in homogeneous reactors where the starting point has no CO, a CO concentration of zero implies a reaction rate of zero. Thus, a starting concentration of CO is needed to start off the ignition process. This is done by assuming that the CO concentration has a spray source term. It is assumed that cells with injected spray have an initial CO mass fraction of $1.0e^{-10}$. This initial mass fraction is arbitrary, it should just be non-zero. It was chosen to be very small so as not to affect the ignition prediction.

The ignition criterion also needs to be defined. The evolution of the CO concentration can be tracked by solving its transport equation (Equation (3.1)), but a criterion is needed which defines ignition. A typical CO trajectory starting at injection looks like the curve shown in Figure 3.2. The CO concentration remains constant and small during the ignition delay time, showing a steep increase at ignition. Ignition can thus be predicted by comparing the CO concentration at each time step to a critical CO concentration. Thus, the ignition criterion used was

$$\text{If} \quad \widetilde{Y_{\mathrm{CO}}} > Y_{\mathrm{CO,crit}} \longrightarrow \text{Ignition} \ . \tag{3.9}$$

Based on homogeneous reactor calculations, a critical CO mass fraction of 0.1 was found to be suitable. The exact coupling between the ignition model and KIVA is discussed in Section 4.3.

3.2 ILDM chemistry

Since detailed chemical mechanisms cannot be used for the simulation of practical three-dimensional turbulent flames, simplified chemical mechanisms are usually used. Usually, assumptions such as partial equilibrium for some reactions or steady-state for some species [55] are used to develop simplified three- or four-step schemes which can be used in CFD calculations. This approach has the following drawbacks [9]:

- For each fuel/oxidizer system, and for each order of the scheme (i.e., two-step, four-step, etc.) considerable human time and labor is required to develop the simplified mechanism.

- The partial-equilibrium and steady-state assumptions are inevitably applied to ranges of compositions and temperatures where they provide poor approximations.

The intrinsic low-dimensional manifold (ILDM) [9, 10, 56] method is free from these drawbacks. It is an automatic reduction of a detailed chemical mechanism into a lower-dimensional mechanism where the number of concentration variables in the simplified mechanism is variable.

3.2.1 Principles behind ILDM

The intrinsic low-dimensional manifold method uses a dynamical systems approach. This method exploits the variety of time scales to systematically simplify a detailed chemical mechanism. As shown in Figure 3.4, chemical processes have a much larger range of time scales than physical processes. Hence, chemical processes which are fast compared to the turbulent mixing time scale can be assumed to be in dynamic equilibrium with the mixing process and with the chemical processes that are slower than the mixing time scale. This assumption, therefore, allows the fast processes to be expressed as combinations of the slow processes and entails considerable reduction in the number of variables required to describe the chemistry [57]. This method is similar in concept to the computational singular perturbation (CSP) method [58], where elementary reactions are grouped into separate reaction groups, each characterized by a single time scale.

For a detailed chemical mechanism with n_s species, n_s different time scales govern the process. If n_f time scales are assumed to be in equilibrium, the system can be described in only $n_r = n_s$-n_f degrees of freedom. An assumption that all the time scales are relaxed results in assuming complete equilibrium (described in Section 2.5.3). Here, the only variables required to describe the chemical system is the mixture composition (i.e. its mixture fraction), the pressure and the mixture enthalpy (or temperature). This results in a zero-dimensional manifold. An assumption that all but n_r time scales

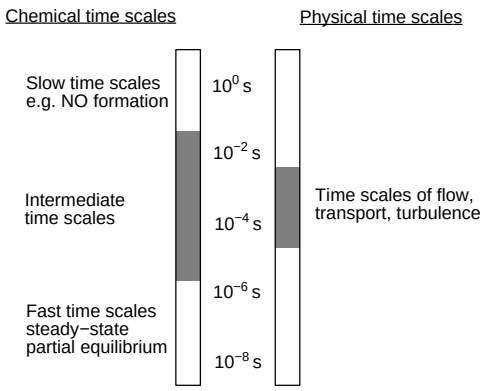

Figure 3.4: Schematic representation of the time scales governing a chemically reacting flow [9]

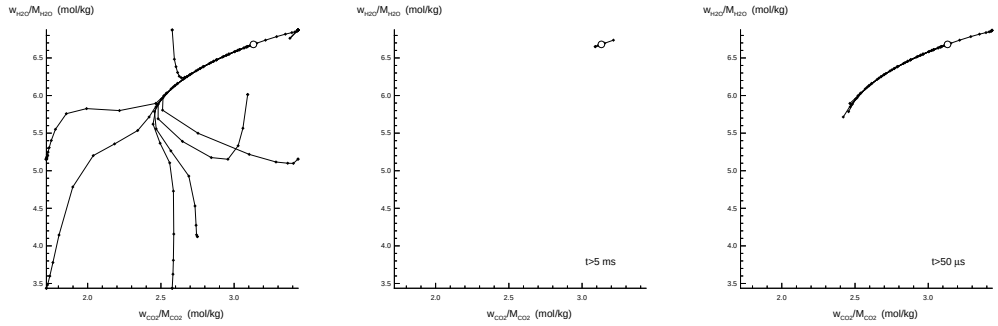

Figure 3.5: Trajectories in a methane-air system. ∘ denotes the equilibrium [38]

are relaxed leads to a system that is described by the mixture fraction, the pressure, the temperature and n_r other parameters (called progress variables). In addition to reducing the number of transport equations that need to be solved, this also reduces the dimension of the pdf that the reaction rate needs to be integrated over in turbulent flows.

The idea behind ILDM can be made clear by observing reaction trajectories in a homogeneous system. Figure 3.5 shows some trajectories for a stoichiometric CH_4-air system, projected onto the H_2O-CO_2 plane [38]. The equilibrium point is marked by a circle. The different trajectories correspond to different initial conditions (chosen such that the equilibrium point is the same). The complete trajectories till equilibrium are shown in Figure 3.5(a). The system takes about 5 ms to reach equilibrium, as shown in Figure 3.5(b). Thus, if the physical processes are slower than 5 ms, the assumption of total equilibrium is justified. However, as seen in Figure 3.4, this is not true. Figure 3.5(c) shows the trajectories after a time of 50 μs. A simple line in the state space is seen as opposed to the complicated curves in Figure 3.5(a). This line corresponds to a one-dimensional manifold in state space. All processes slower than 50 μs (the rate determining processes) are described by the movement along this line. All processes faster than 50 μs can be assumed to be in equilibrium. If one is interested in processes faster than 50 μs, higher dimensional manifolds need to be considered.

3.2.2 Mathematical treatment of ILDM

In the ILDM method, the fast chemical reactions do not need to be identified *a priori*. An eigenvalue analysis of the detailed chemical mechanism needs to be carried out which identifies the fast processes in dynamic equilibrium with the slow processes. A homogeneous, adiabatic, isobaric system is determined by $n = n_s + 2$ variables (n_s species, the pressure and the temperature). The state of the system is given as a point in an n-dimensional state space. The governing equation system can be written as

$$\frac{\partial \vec{\psi}}{\partial t} = \vec{F}(\vec{\psi}) \tag{3.10}$$

with $\vec{\psi} = (T, p, Y_1, Y_2, ..., Y_{n_s})^{\mathrm{T}}$. Since, this equation system is, in general, non-linear, the function $\vec{F}$ can be linearized locally at a point ψ_0 by a Taylor series approximation

$$\frac{\partial \vec{\psi}}{\partial t} = \vec{F}(\vec{\psi}_0) + J(\vec{\psi} - \vec{\psi}_0) \ , \tag{3.11}$$

where J is the Jacobian matrix ($J = \partial \vec{F}/\partial \vec{\psi}$). Local time scale information can be obtained by performing an eigenvector analysis of the Jacobian matrix, J. There exist locally n characteristic time scales and associated with those time scales, n characteristic directions (eigenvalues and eigenvectors of the local Jacobian). The fast relaxation processes (corresponding to eigenvalues $<< 0$) lead the system quickly to points on the state space, where there is equilibrium with respect to the fastest time scales. Mathematically, this is done by doing a Schur decomposition of the Jacobian ($Q^T J Q = N$), such that the eigenvalues appear in the diagonal of N. Then, the low-dimensional manifold is defined as the set of points in the state space for which

$$Q_{\mathrm{L}}^{\mathrm{T}} J = 0 \tag{3.12}$$

where $Q_{\mathrm{L}}^{\mathrm{T}}$ is the matrix obtained from Q^{T} by omitting the first $2+n_{\mathrm{e}}+n_{\mathrm{r}}$ rows (n_{e} being the number of elements), namely the rows corresponding to the conserved (pressure, enthalpy and element composition) and slowly changing variables. Thus, along with Equation (3.12), one needs $2 + n_{\mathrm{e}} + n_{\mathrm{r}}$ parameter equations, i.e., one needs to specify the temperature (T), the pressure (p), the element composition (ξ), and the progress variables. The above equation system can be solved to obtain the reaction rates of the progress variables.

The computation of ILDM points can be expensive, and hence the dependent variables calculated in the ILDM procedure (reaction rates of progress variables, species concentrations, enthalpy, molar mass, etc.) can be tabulated as functions of the progress variables and used in the CFD calculations. An *in-situ* tabulation procedure [59] was used, which enables the calculation of only those points that are needed during the CFD calculation.

3.2.3 Use of ILDM and problems

The principles behind ILDM are very promising, and the method has been tested in homogeneous reactors [56] and laminar premixed flames [60] with very good results. These results, however, almost always have the following characteristics:

- The above systems are usually stoichiometric or near-stoichiometric. The performance of ILDM in this equivalence ratio region is very good. However, the use of the ILDM method in the lean or rich regions has not been investigated.
- The use of ILDM, where the assumption that most of the chemical time scales are relaxed is valid, is justified, i.e., in partially burnt or burnt gases. However, a large number of progress variables may be needed in un-burnt gases or in the early stages of combustion. This is the reason why ILDM was not used as an ignition model in this thesis, as the assumption that the chemical time scales are relaxed is not true for ignition.
- Most of the fuels used are lower hydrocarbons (methane, syngas, etc.). However, higher hydrocarbon (like heptane, dodecane) systems introduce additional stiffness in the equation system. The equilibrium concentrations of radicals are much lower for higher hydrocarbon systems than for lower hydrocarbon systems, making the equation system more difficult to solve.
- Most of the reported systems are at atmospheric pressure. High pressures present in Diesel engines cause the chemical time scales to be much faster, making it more difficult to apply the ILDM theory.

The above problems are also present in internal combustion engines, as a chemistry model needs to cover equivalence ratios from lean to rich in a diffusion flame. Also, even though a different ignition model can be used which can predict the location and timing of ignition, the chemistry model then needs to take over till equilibrium.

Thus, an ILDM table was generated in order to test its applicability. The fuel used was the model Diesel fuel (n-heptane). A detailed chemical mechanism consisting of 43 species and 393 elementary reactions [61] was used. One progress variable (the species CO_2) was used as a progress variable. Thus, a transport equation of the type Equation (2.20) needs to be solved for CO_2:

$$\frac{\partial \overline{\rho}\widetilde{Y_{\mathrm{CO_2}}}}{\partial t} + \mathrm{div}(\overline{\rho}\tilde{\vec{u}}\widetilde{Y_{\mathrm{CO_2}}}) = \mathrm{div}(\overline{\rho} D_{\mathrm{T}} \,\mathrm{grad}\, \widetilde{Y_{\mathrm{CO_2}}}) + \overline{\rho}\widetilde{\dot{Y}^{\mathrm{C}}_{\mathrm{CO_2}}} \quad . \tag{3.13}$$

The instantaneous source term due to chemistry ($\dot{Y}^{\mathrm{C}}_{\mathrm{CO_2}}$) is obtained from ILDM, and this needs to then be integrated over a probability density function in order to get the mean chemical source term (see Section 3.2.4).

Since one progress variable (CO_2) was used, the ILDM table was a three-dimensional table consisting of the CO_2 reaction rate, the other species compositions, enthalpy, density, specific heat, etc. as functions of the three dimensions (the temperature, the mixture fraction and the CO_2 mass fraction). Another parameter that needs to be specified is the pressure. Since in engines, the cylinder pressure varies with time, pressure could be a fourth dimension in the ILDM table. Pressure affects the reaction mechanism through the rate coefficients. The variation of the rate coefficients with

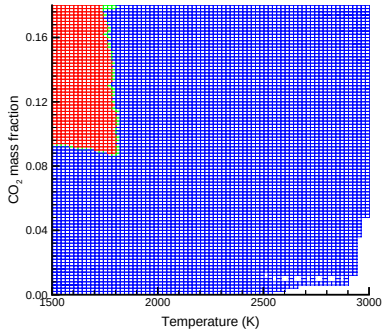

Figure 3.6: Slice of the ILDM table for equivalence ratio of 1 ($\xi = 0.062$)

pressure is described by fall-off curves [38] where the rate coefficient increases with pressure, up to a certain limit, where it then remains almost constant. Although a comparison between reaction rates at 1 bar and 50 bar show a considerable difference, the required pressure range is from about 70 bar to 100 bar in Diesel engines, as injection typically takes place at about 70 bar, and peak pressures of about 100 bar are achieved. In this pressure range, the rate coefficients remain almost constant, and thus, a representative pressure can be used to describe the reaction mechanism. A representative pressure of 80 bar was chosen for Diesel engines, and thus a reaction mechanism at 80 bar pressure was used.

Slices from the 3-D ILDM table can then be looked at, and 2-D pictures of the table (at constant mixture fractions) can be created. Figure 3.6 shows an example of such a slice at an equivalence ratio of 1 (stoichiometric mixture fraction of 0.062). The red cells are cells where ILDM does not work (no solution to the ILDM equations could be found), and the blue cells are cells where ILDM works.

The majority of the cells in the stoichiometric region are blue, indicating that ILDM works well in this regime. However, slices of the ILDM table in the lean (Figure 3.7(a)) and in the rich (Figure 3.7(b)) regions do not look that good. Several red sections are seen in the table, where the ILDM method does not work. In these figures, the CO_2 mass fraction ranges from about zero to the equilibrium value, while the temperature ranges from about 1500 K to about 3000 K. Temperatures lower than 1500 K are not shown, as no ILDM points could be found here. Also, it is seen that, except in the stoichiometric region, ILDM does not work near equilibrium.

The reasons for these problems are not very clear and could be:

- The concept of ILDM may not be valid in these regions, i.e. the assumption that most of the chemical time scales are relaxed may not be true. Mathematically, this means that no significant gap in the eigenvalue spectrum exists. This could be true during the start of the combustion process ($T < 1500$ K) and during ignition.
- The system of ILDM equations (Equation 3.12) is a difficult system to solve, and

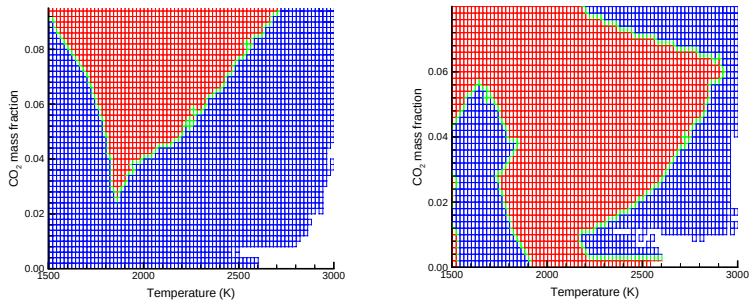

Figure 3.7: Slices of the ILDM table for a) equivalence ratio = 0.5 ($\xi = 0.031$) b) equivalence ratio = 1.5 ($\xi = 0.093$)

the numerical solver may need to be improved.

- At lower temperatures, during the start of combustion and near equilibrium, the reaction rates are nearly zero, and the ILDM method could have problems due to this.

Thus, a strategy needs to be found which can utilize the advantages of ILDM where it works, and uses another method where ILDM fails. Ignition in Diesel engines usually takes place at pressures of around 70 bar (temperatures around 900 K). The development of the the flame then needs to be predicted by the chemistry model. However, ILDM works only above temperatures of 1500 K. Thus, a method is needed which can predict the initial development of the flame. One way to achieve this is to set the ignition cell on the manifold, i.e. to assume that the cell, on igniting, is immediately partially burnt and can be set on the manifold. This can be done by changing the temperature and species composition of the cell, such that the element composition remains unchanged, and such that it lies on the one-dimensional manifold. Another method is to use a secondary chemistry model up to 1500 K, and to then switch to ILDM. The new chemistry model should not be computationally expensive, as most of the pollutant formation takes place at temperatures above 1500 K, and as it is only an intermediate model. The most convenient model to use was a global kinetic approximation as described in Section 2.5.2, i.e., the combustion is described by

$$C_7H_{16} + 11O_2 \longrightarrow 7CO_2 + 8H_2O \tag{3.14}$$

with the first-order rate coefficient given by

$$k = 4.6 \times 10^{11} e^{\frac{-15780\mathrm{K}}{T}} [C_7H_{16}]^{0.25} [O_2]^{1.5} \quad 1/\mathrm{s} \quad . \tag{3.15}$$

The strategy actually used in this thesis is a combination of both. The first cell where ignition is predicted is set on the manifold, i.e., it is assumed that the cell is

partially burnt immediately, which is in accordance with experimental results. The point on the manifold chosen is that corresponding to a temperature of 2200 K and CO_2 mass fraction of 0.1 respectively. However, the ignition model does not need to be discontinued after the first ignition location is found. Knock (spontaneous ignition of the mixture ahead of the flame front) and secondary ignition spots are common in Diesel engines [7]. These new ignition spots were not treated like the first ignition location, which was set immediately on the manifold. In the secondary ignition spots, a combination of the above global kinetic mechanism (upto 1500 K) and ILDM (above 1500 K) was used.

The above strategy takes care of the connection between ignition and ILDM outside the table limits (temperatures less than 1500 K). However, as can be seen from Figures 3.6 and 3.7, there exist regions within the table itself where ILDM fails to deliver a result. Clearly, a strategy is required which delivers a result for these points. A strategy similar to that above, where another chemistry model was used where ILDM does not work, cannot be used within the tabulation limits, because while integrating the chemical reaction rates over a pdf, consistent models need to be used in order to avoid a change in the pdf dimensions. Since ILDM almost always fails when the reaction is very slow, it can be assumed that the reaction rate of the progress variable is zero, i.e.,

$$\dot{Y}^{\mathrm{C}}_{\mathrm{CO_2}} = 0 \ . \tag{3.16}$$

The other species compositions are also required, and these cannot be obtained when ILDM fails. Hence, if the species composition at another point is to be used as an approximation, the following factors need to be considered:

- Due to the assumption that the reaction rate of CO_2 is zero (Equation (3.16)), the CO_2 mass fraction of the approximate point should be the same as that of the original point.
- The element composition cannot change, i.e., the mixture fraction ξ of the approximate point should be the same as that of the original point.
- The only other dimension that can be changed in order to search for an approximate point is the temperature. As can be seen in Figures 3.6 and 3.7, ILDM usually succeeds at higher temperatures.

Hence, whenever a red cell is encountered in the table, the species composition in this cell is approximated by that in another cell with the same CO_2 mass fraction, the same mixture fraction, but at a higher temperature. This approach is shown in Figure 3.8, where cell number 1 is assigned a CO_2 reaction rate of zero, and a species composition of cell number 2.

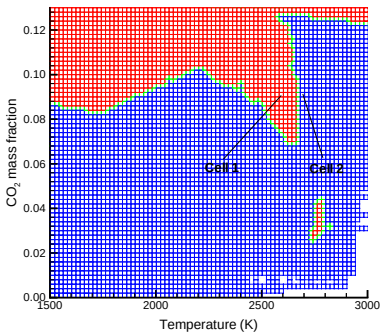

Figure 3.8: Approximation for the species composition in Cell 1 with that in Cell 2. Slice of the table for equivalence ratio = 1.2 ($\xi = 0.075$)

3.2.4 ILDM with pdfs

The above sections described means of obtaining the instantaneous progress variable rates ($\dot{Y}^{\mathrm{C}}_{\mathrm{CO_2}}$) and the instantaneous species compositions (Y_i). The Favre-averaged species equations (Equation (2.20)), however, contain the mean chemical source terms. Thus, as described in Section 2.6.2, the source terms need to be integrated over a probability density function (pdf). As described in Section 3.2.3, a one-dimensional manifold method was used, with the CO_2 mass fraction as the progress variable. The chemical source terms are hence functions of three variables, the mixture fraction, the temperature and the CO_2 mass fraction. They, hence, have to be integrated over a three-dimensional pdf, i.e.,

$$\begin{aligned} \widetilde{\dot{Y}^{\mathrm{C}}_{\mathrm{CO_2}}} &= \int \dot{Y}^{\mathrm{C}}_{\mathrm{CO_2}}(\xi, T, Y_{\mathrm{CO_2}}) \tilde{P}(\xi, T, Y_{\mathrm{CO_2}})\, \mathrm{d}\xi\, \mathrm{d}T\, \mathrm{d}(Y_{\mathrm{CO_2}}) \ , \\ \widetilde{Y_i} &= \int Y_i(\xi, T, Y_{\mathrm{CO_2}}) \tilde{P}(\xi, T, Y_{\mathrm{CO_2}})\, \mathrm{d}\xi\, \mathrm{d}T\, \mathrm{d}(Y_{\mathrm{CO_2}}) \ . \end{aligned} \tag{3.17}$$

The pdf $P(\xi, T, Y_{\mathrm{CO_2}})$ now needs to be determined. Consistent with the assumptions made in Section 3.1.2, the three-dimensional pdf can be split into three one-dimensional pdfs if the statistical independence of the three variables is assumed, i.e.,

$$\tilde{P}(\xi, T, Y_{\mathrm{CO_2}}) = \tilde{P}(\xi)\tilde{P}(T)\tilde{P}(Y_{\mathrm{CO_2}}) \tag{3.18}$$

and the three one-dimensional pdfs now need to be determined. Using the mean and variance of the mixture fraction ($\tilde{\xi}$, $\widetilde{\xi''^2}$) and the temperature ($\tilde{T}$, $\widetilde{T''^2}$), and assuming the shape of the pdfs (beta pdfs for $P(\xi)$ and $P(T)$), the two pdfs, $\tilde{P}(\xi)$ and $\tilde{P}(T)$ can be determined.

The pdf for CO_2 ($\tilde{P}(Y_{\mathrm{CO_2}})$) is more complicated to construct. As the CO_2 mass fraction is dependent on the mixture fraction and the temperature, the assumption of statistical

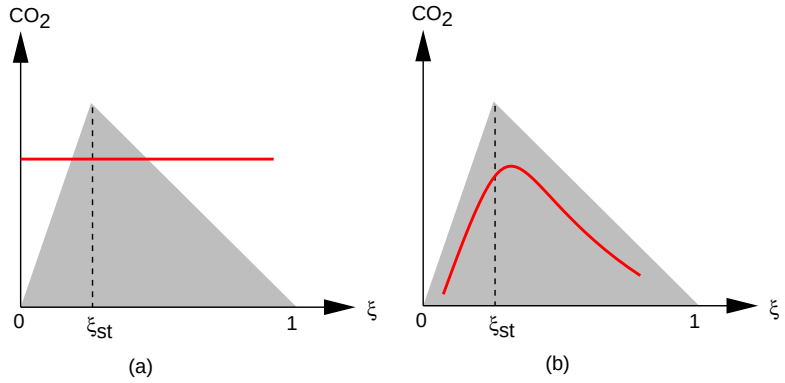

Figure 3.9: Schematic representation of the influence of the pdf variable used. a) A delta function for CO_2 is used b) A delta function for b is used

independence creates problems during the pdf integration. This can be explained by considering a simple chemical mechanism.

Assuming a global one-step reaction, i.e. Fuel + Oxidizer $\longrightarrow$ CO_2 + H_2O, it can be seen that the maximum CO_2 concentration is obtained when the mixture is stoichiometric (with mixture fraction ξ_{st}). In addition, the CO_2 concentration is zero for pure fuel (mixture fraction $\xi = 1$) and for pure air (mixture fraction $\xi = 0$). Thus, a region can be constructed which gives the maximum possible CO_2 concentration as a function of the mixture fraction. This region is in the shape of a triangle (the shaded region in Figure 3.9). All points outside this triangle are not physically possible.

Assuming now that a delta function is used for the CO_2 concentration, then integrating over the mixture fraction will result in integrating along the red line in Figure 3.9(a), as the mixture fraction and CO_2 have been assumed to be independent. Thus, the integration would require chemical source terms outside the triangle, which is not physical.

This problem can be solved by carrying out a normalization of the CO_2 concentration. A new variable, b, can be defined as

$$b = \frac{Y_{CO_2}}{Y_{CO_2,max}} \tag{3.19}$$

and since $Y_{CO_2,max}$ contains some dependence on the mixture fraction and the temperature, it is a better approximation to assume that b, ξ and T are independent of each other. With a change in variables, the pdf $P(\xi, T, Y_{CO_2})$ in Equation (3.17) can now be transformed into $P(\xi, T, b)$, and using statistical independence,

$$\tilde{P}(\xi, T, b) = \tilde{P}(\xi)\tilde{P}(T)\tilde{P}(b) \quad . \tag{3.20}$$

Figure 3.9(b) shows how the pdf of CO_2 looks if now a delta function is assumed for b instead of for CO_2. Integrating over the mixture fraction now results in integrating

over the red curve which remains within the triangle, and thus the CO_2 concentration always remains physical.

The pdf of b now needs to be determined, for which its mean and its variance are needed. The mean of b is given by

$$\tilde{b} = \widetilde{Y_{CO_2}/Y_{CO_2,max}} \quad . \tag{3.21}$$

However, since the resulting fluctuation terms cannot be determined, the mean of b is approximated by

$$\tilde{b} = \frac{\widetilde{Y_{CO_2}}}{\widetilde{Y_{CO_2,max}}} \quad . \tag{3.22}$$

The mean CO_2 concentration ($\widetilde{Y_{CO_2}}$)is obtained from its transport equation (Equation (3.13)). The mean maximum CO_2 concentration ($\widetilde{Y_{CO_2,max}}$) is only a function of the mixture fraction and the temperature (as the equilibrium is a zero-dimensional manifold), and hence needs to be integrated over $P(\xi, T)$:

$$\widetilde{Y_{CO_2,max}} = \int Y_{CO_2,max} \tilde{P}(\xi)\tilde{P}(T)\, \mathrm{d}\xi\, \mathrm{d}T \quad . \tag{3.23}$$

If a beta function for b needs to be used, an equation for its variance is needed. The variance equation would, however, contain even more fluctuation terms which would need to be modeled. In order to avoid this problem, a delta function for b was used, for which only the mean is needed, i.e.,

$$\tilde{P}(b) = \delta(b - \tilde{b}) \tag{3.24}$$

Thus, to summarize, beta functions were used for the mixture fraction and the temperature, while a delta function was used for b. With this pdf, the mean species and the mean chemical source terms can be determined. Only the bounds of the pdf used need to be mentioned. Although ξ and b are physically defined between 0 and 1, and T between 0 and ∞, an integration over the entire range is not possible. Hence, limits for the pdf need to be chosen. Since the ILDM method delivers reasonable results only for ξ between 0.03 and 0.10 (equivalence ratios between 0.48 and 1.6), these were chosen as limits for the mixture fraction. Also, as can been seen from Figures 3.6, 3.7 and 3.8, limits of 1500 K and 3000 K are reasonable for the temperature in order to avoid points where ILDM fails and to take advantage of the regions where it succeeds. Since a delta function was used for b, no range needs to be chosen. However, as can be seen from the table figures, ILDM rarely produces a result near equilibrium. Hence, no integration

was performed for $b > 0.9$ (i.e. the mixture was assumed to be in equilibrium when its CO_2 mass fraction reached 90% of its equilibrium value).

The mean source terms in the Favre-averaged Navier-Stokes equations due to chemistry can now be defined. After the mean species ($\overline{\rho_i} = \overline{\rho}\widetilde{Y}_i$) are obtained from Equation 3.17, the source terms in the species balance equation (Equation (2.20)) and the energy equation (Equation (2.23)) are given by equations similar to Equation (2.67), i.e.

$$\begin{aligned} \overline{\dot{\rho}_i{}^{\mathrm{C}}} &= (\widetilde{\rho}_i - \widetilde{\rho_i{}^{\mathrm{old}}})/\Delta t \ , \\ \overline{\dot{Q}^{\mathrm{C}}} &= -\sum_i \overline{\dot{\rho}_i{}^{\mathrm{C}}}(\Delta h_{\mathrm{f}}{}^0)_i \ , \end{aligned} \tag{3.25}$$

where $\widetilde{\rho_i{}^{\mathrm{old}}}$ are the species densities before chemistry takes place. The exact coupling between the chemistry model and KIVA is discussed in Section 4.3.

3.3 Pollutant formation

One of the main reasons for using sophisticated models for chemistry and turbulence is the accurate prediction of pollutant formation. Diesel engines are a major source of urban air pollution, two main pollutants being nitric oxides (NO_x) and soot.

3.3.1 NO_x formation

NO and NO_2, collectively known as NO_x, are the major pollutants produced by Diesel engines. NO_x is formed by four different routes: the thermal route, the prompt route, the N_2O route and the fuel-bound nitrogen route [62]. All the reactions involved in NO_x formation could theoretically be included in the detailed chemical mechanism used in ILDM. However, as can be seen in Figure 3.4, the time scales involved in NO formation are much slower than those of the other chemical reactions. Thus, if all the NO_x reactions were part of the mechanism, more progress variables would have to used. Hence, NO_x reactions were not part of the mechanism used for the ILDM and a separate NO_x model was used to predict the NO_x formation. Out of the four routes, the fuel-bound nitrogen route is important only for coal combustion, and the N_2O route is not a significant source of NO [38]. Prompt NO results from a reaction between CH and N_2, and due to the low activation energies of the reactions involved, it is favored at lower temperatures (about 1000 K). On the other hand, thermal NO is favored at higher temperatures and is therefore the most significant source of NO_x. Hence, only thermal NO was modeled in this thesis.

Thermal NO or Zeldovich NO is formed by the elementary reactions

$$\begin{array}{lllllllll} \mathrm{O} & + & \mathrm{N_2} & \overset{k_1}{\rightarrow} & \mathrm{NO} & + & \mathrm{N} & k_1 = 1.8 \cdot 10^{14} & \exp(\text{-318 kJ mol}^{-1}/\ (RT)) & \mathrm{cm^3/(mol\ s)} \\ \mathrm{N} & + & \mathrm{O_2} & \overset{k_2}{\rightarrow} & \mathrm{NO} & + & \mathrm{O} & k_2 = 9.0 \cdot 10^{9} & \exp(\text{-27 kJ mol}^{-1}/(RT)) & \mathrm{cm^3/(mol\ s)} \\ \mathrm{N} & + & \mathrm{OH} & \overset{k_3}{\rightarrow} & \mathrm{NO} & + & \mathrm{H} & k_3 = 2.8 \cdot 10^{13} & & \mathrm{cm^3/(mol\ s)} \end{array} \tag{3.26}$$

The name "thermal" is used, as the first reaction has a very high activation energy due to the strong triple bond in the N_2 molecule, and is fast only at higher temperatures. This reaction is hence the rate-limiting reaction in the formation of thermal NO. The rate of formation of NO is

$$\frac{\mathrm{d[NO]}}{\mathrm{d}t} = k_1[\mathrm{O}][\mathrm{N_2}] + k_2[\mathrm{N}][\mathrm{O_2}] + k_3[\mathrm{N}][\mathrm{OH}] \ . \tag{3.27}$$

Assuming that the nitrogen atoms are in quasi-steady state (as the first reaction is the rate-determining step),

$$\frac{\mathrm{d[N]}}{\mathrm{d}t} = k_1[\mathrm{O}][\mathrm{N_2}] - k_2[\mathrm{N}][\mathrm{O_2}] - k_3[\mathrm{N}][\mathrm{OH}] \approx 0 \tag{3.28}$$

one obtains for the rate of NO formation

$$\frac{\mathrm{d[NO]}}{\mathrm{d}t} = 2k_1[\mathrm{O}][\mathrm{N_2}] \ . \tag{3.29}$$

The above equation gives the chemical source term for the NO equation. For the mean source term, the above equation needs to be integrated over a pdf. The rate constant, k_1 is a function of temperature, and the species concentrations, [O] and [N_2], are functions of ξ, T and b through the ILDM method. Thus, the NO source term needs to be integrated over the same pdf introduced in Section 3.2.4, i.e.

$$\widetilde{\frac{\mathrm{d[NO]}}{\mathrm{d}t}} = \int \frac{\mathrm{d[NO]}}{\mathrm{d}t} \tilde{P}(\xi)\tilde{P}(T)\tilde{P}(b)\,\mathrm{d}\xi\,\mathrm{d}T\,\mathrm{d}b \tag{3.30}$$

3.3.2 Soot formation

Soot is another major pollutant produced by Diesel engines. Most of the particulates result from the incomplete combustion of fuel hydrocarbons. Prediction of soot formation and oxidation is one of the biggest challenges in combustion modeling [63, 64]. A variety of soot models, ranging from simple empirical correlations relating the amount

of particulates in the exhaust to the engine operating parameters [65], to very detailed descriptions of pre-particle chemistry and soot particle dynamics [66–68] have been proposed for engine simulations. The former are valid only for certain geometries and the latter are not only too computationally expensive to use, but also not warranted due to uncertainties in the other models involved, such as the spray model and the turbulence model. In this thesis, a semi-empirical model is used, where the complex process of soot formation and oxidation is described in terms of several global steps.

Soot formation involves the following steps:

- Particle formation via soot precursors, called polycyclic aromatic hydrocarbons (PAH). These compounds are usually formed under fuel-rich conditions. PAH formation usually starts with C_3H_3 formation, which can form the first ring (benzene C_6H_6) after recombination to an aliphatic C_6H_6 and rearrangement [38, 69].
- Particle growth, which includes surface growth and coagulation. Surface growth involves the attachment of gas-phase species (mostly C_2H_2) to the surface of the particles and their incorporation into the particulate phase. Soot coagulation involves the "sticking" of two particles to form a larger particle.
- Soot oxidation, where the oxidizing species can be O, OH or O_2, with the main oxidizing species being OH.

In semi-empirical models, the soot formation process is described in terms of a small number of variables, usually the soot volume fraction (f_v, the volume of soot/total volume), the soot number density (N_s, the number of soot particles per unit volume) and the soot diameter (d_s). f_v, N_s and d_s are mutually dependent, and for spherical particles,

$$f_\mathrm{v} = \frac{\pi}{6} N_\mathrm{s} d_\mathrm{s}^3 \ . \tag{3.31}$$

Another variable possible is the soot concentration (C_s), which is related to the number density by

$$N_\mathrm{s} = C_\mathrm{s} N_\mathrm{A} \ , \tag{3.32}$$

where N_A is Avogadro's number. f_v and N_s (or C_s) are usually used as the independent variables, since they relate to the different stages of soot particle generation (the source of C_s) and soot particle growth (the source of f_v) [7]. The model used in this thesis is based on the simplified representation of the different processes in the balance equations for f_v and C_s [70–75].

Balance equations for their Favre means, $\widetilde{f}_\mathrm{v}$ and $\widetilde{C}_\mathrm{s}$, similar to Equation (2.20) are solved for. Only the source terms need to be defined. Although the source terms are

based on physical considerations, the coefficients in the model need to be determined empirically and were determined by matching experimental data for heptane in a shock tube [76, 77].

Soot Concentration:

The source term for the soot concentration has terms due to nucleation (NC) and coagulation (CO). Coagulation decreases the soot number density (and hence the concentration), while nucleation increases the soot concentration. Surface growth leaves the number of particles unchanged. It is assumed that the soot particles are not completely burned, so that oxidation has no effect on the number density,

$$\frac{\mathrm{d}C_\mathrm{s}}{\mathrm{d}t} = \left.\frac{\mathrm{d}C_\mathrm{s}}{\mathrm{d}t}\right|_\mathrm{NC} + \left.\frac{\mathrm{d}C_\mathrm{s}}{\mathrm{d}t}\right|_\mathrm{CO} \quad . \tag{3.33}$$

The starting point of soot formation is nucleation by the reaction $C_3H_3{+}C_3H_3 \rightleftharpoons C_6H_6$, which leads to benzene after rearrangement of the C_6H_6. Accordingly, the nucleation term is the rate α of this reaction

$$\left.\frac{\mathrm{d}C_\mathrm{s}}{\mathrm{d}t}\right|_\mathrm{NC} = \frac{\alpha}{10} \quad . \tag{3.34}$$

The factor of 10 in the nucleation term results from the assumption that at least 10 benzene molecules are needed to build one soot particle. Coagulation of soot particles is described by a collision number β [78],

$$\left.\frac{\mathrm{d}C_\mathrm{s}}{\mathrm{d}t}\right|_\mathrm{CO} = -\beta \cdot C_\mathrm{s}^2 \quad . \tag{3.35}$$

The coefficients are:

$$\begin{aligned} \alpha &= 2.0 \times 10^6 \frac{\mathrm{mol}}{\mathrm{m^3 \cdot s}} \cdot \left(\frac{[\mathrm{C_3H_3}]}{\mathrm{mol/m^3}}\right)^2 \quad , \\ \beta &= 1.0 \times 10^7 \frac{\mathrm{m^3}}{\mathrm{mol \cdot s}} \cdot \left(\frac{T}{\mathrm{K}}\right)^{1/2} \quad . \end{aligned} \tag{3.36}$$

Thus, for the temporal change of the soot particle concentration, we have

$$\frac{\mathrm{d}C_\mathrm{s}}{\mathrm{d}t} = \frac{\alpha}{10} - \beta \cdot C_\mathrm{s}^2 \tag{3.37}$$

with α and β determined from Equation (3.36).

Soot volume fraction:

The soot volume fraction f_v has source terms due to nucleation, surface growth (SG) and oxidation (OX). Nucleation and surface growth increase the volume fraction, and oxidation reduces it; coagulation has no effect on the volume fraction,

$$\frac{\mathrm{d}f_v}{\mathrm{d}t} = \left.\frac{\mathrm{d}f_v}{\mathrm{d}t}\right|_{NC} + \left.\frac{\mathrm{d}f_v}{\mathrm{d}t}\right|_{SG} + \left.\frac{\mathrm{d}f_v}{\mathrm{d}t}\right|_{OX} \quad . \tag{3.38}$$

The source term due to nucleation is given by

$$\left.\frac{\mathrm{d}f_v}{\mathrm{d}t}\right|_{NC} = \delta = V_{NC} \cdot \alpha \quad [1/\mathrm{s}] \quad , \tag{3.39}$$

where V_{NC} is the volume of a nucleation species (m^3/mol) and is given by

$$V_{NC} = \frac{m_{soot}}{\rho_{soot}} \ , \tag{3.40}$$

where m_{soot} is the molar mass of soot (taken to be that of $C_{60}H_{60}$) and ρ_{soot} is the density of soot (taken to be 1.8 g/cm^3).

Surface growth results from the attachment of C_2H_2 onto the surface of the particles. The source term due to surface growth is derived from gas kinetics and gives the first order growth law suggested in the literature [78] and is given by [77]

$$\left.\frac{\mathrm{d}f_v}{\mathrm{d}t}\right|_{SG} = \gamma \cdot f_v^{2/3} \cdot C_s^{1/3} \cdot N_A^{1/3} \cdot \frac{f_{v\infty} - f_v}{f_{v\infty}} \ , \tag{3.41}$$

where $f_{v\infty}$ is the maximum volume fraction and γ is given by

$$\gamma \ = \ \frac{\sigma_{SG}}{\rho_{soot}} \sqrt{\frac{N_A R_0 m_G}{2\pi}} (36\pi)^{1/3} T^{1/2} C_G \ , \tag{3.42}$$

where m_G is the mass of the growth species (C_2H_2), and C_G is its concentration. Substituting known values, the result is

$$\gamma \ = \ \sigma_{SG} \cdot 4.97 \times 10^{-4} \cdot \left(\frac{T}{\mathrm{K}}\right)^{1/2} \cdot \left(\frac{[C_2H_2]}{\mathrm{mol/m}^3}\right) \quad [\frac{\mathrm{m}}{\mathrm{s}}] \quad , \tag{3.43}$$

where σ_{SG} is the sticking coefficient of C_2H_2 on the surface ($\sigma_{\mathrm{SG}} = 1.4 \times 10^{-3}$). In order to obtain the maximum volume fraction, a curve fit was used [77], which gives the maximum volume fraction as a function of the excess C atom concentration, C_{surplus} ($10^{18}/\mathrm{cm}^3$) as

$$f_{\mathrm{v}\infty} = 1.453 \times 10^{-6} C_{\mathrm{surplus}}^{1.7} \quad . \tag{3.44}$$

The excess C atom concentration can be obtained by computing the excess C atoms available over a critical C/O ratio. This critical C/O ratio differs for different fuels and with pressure. A ratio of 0.5 was used in this thesis [79].

The source term due to oxidation is similar to that of surface growth, as it involves the "sticking" of OH on the surface of the soot, instead of C_2H_2. Only one oxidation reaction is considered, namely

$$\mathrm{SOOT\text{-}C} + \mathrm{OH} \rightarrow \mathrm{SOOT} + \mathrm{CHO} \quad .$$

The source term is given by

$$\left.\frac{\mathrm{d}f_{\mathrm{v}}}{\mathrm{d}t}\right|_{\mathrm{OX}} = \varepsilon \cdot f_{\mathrm{v}}^{2/3} \cdot C_{\mathrm{s}}^{1/3} \cdot N_{\mathrm{A}}^{1/3} \tag{3.45}$$

with ε given by (similar to Equation (3.42), but using values for OH instead of for C_2H_2)

$$\varepsilon = \sigma_{\mathrm{OX}} \cdot 3.4 \times 10^{-4} \cdot \left(\frac{T}{\mathrm{K}}\right)^{1/2} \cdot \left(\frac{[\mathrm{OH}]}{\mathrm{mol/m^3}}\right) \; [\frac{\mathrm{m}}{\mathrm{s}}] \; , \tag{3.46}$$

where σ_{OX} is the sticking coefficient of OH on the surface ($\sigma_{\mathrm{OX}} = 0.1$ [38]).

Thus, for the temporal change of the soot volume fraction, one has

$$\frac{\mathrm{d}f_{\mathrm{v}}}{\mathrm{d}t} = \delta + \gamma \cdot f_{\mathrm{v}}^{2/3} \cdot C_{\mathrm{s}}^{1/3} \cdot N_{\mathrm{A}}^{1/3} \cdot \frac{f_{\mathrm{v}\infty} - f_{\mathrm{v}}}{f_{\mathrm{v}\infty}} - \varepsilon \cdot f_{\mathrm{v}}^{2/3} \cdot C_{\mathrm{s}}^{1/3} \cdot N_{\mathrm{A}}^{1/3} \tag{3.47}$$

with δ, γ and ε determined from Equations (3.39), (3.43) and (3.46) respectively.

In order to get the averaged source terms for the soot concentration and the volume fraction, the source terms given by Equations (3.37) and (3.47) have to be integrated over a pdf (the same pdf described in Section 3.2.4). Since the source terms are however, themselves functions of f_{v} and C_{s}, delta functions for these quantities are assumed.

$$\widetilde{\frac{\mathrm{d}C_\mathrm{s}}{\mathrm{d}t}} = \int \frac{\mathrm{d}C_\mathrm{s}}{\mathrm{d}t} \tilde{P}(\xi, T, b)\, \mathrm{d}\xi\, \mathrm{d}T\, \mathrm{d}b \ ,$$
$$\widetilde{\frac{\mathrm{d}f_\mathrm{v}}{\mathrm{d}t}} = \int \frac{\mathrm{d}f_\mathrm{v}}{\mathrm{d}t} \tilde{P}(\xi, T, b)\, \mathrm{d}\xi\, \mathrm{d}T\, \mathrm{d}b \ . \tag{3.48}$$

3.4 Radiation heat transfer

Radiation heat transfer in engine combustion chambers derives from two sources: gas radiation and particulate cloud radiation. For homogeneous charge (spark ignition) engines, the amount of soot produced is small and thus, only gas radiation is significant. Computations for spark ignition engines based on gas radiation indicate that gas radiation is small (less than 10 %) compared to convection and can be neglected [80]. In Diesel engines, gas radiation is also a small fraction of the total heat transfer, but particulate radiation is important. Thus, in order to predict pollutant formation accurately, accurate temperature distributions in the engine cylinder are required, since the chemical kinetics involved are extremely temperature dependent. If radiation plays an important role in engine heat transfer, a suitable method needs to be found, which can model its effects on the temperature and concentration fields in the combustion chamber.

Radiation does not contribute any terms to the conservation of mass, momentum and species concentration. The classical conservation of energy equation (Equation (2.7)) is modified by a contribution which accounts for radiation heat transfer. The heat flux vector $\vec{J}$ in Equation (2.8) now also has a contribution due to radiation, i.e.,

$$J = -K \operatorname{grad} T + \vec{F} - \rho D \sum_i h_i \operatorname{grad}(\rho_i/\rho) \ , \tag{3.49}$$

where $\vec{F}$ is the radiation heat flux vector. The divergence of the radiative heat flux vector ($\operatorname{div} \vec{F}$) which appears in the energy equation now needs to be determined. The radiative transfer equation (RTE) forms the basis for quantitative study of the transfer of radiant energy in a participating medium. It can be derived by an application of an energy balance on an elementary volume taken along the direction of a pencil of rays and confined within an elementary solid angle [81],

$$(\nabla \cdot \vec{\Omega}) I_\lambda = -k_{\mathrm{a},\lambda} I_\lambda + k_{\mathrm{s},\lambda} I_\lambda + k_{\mathrm{a},\lambda} I_{\mathrm{b},\lambda} + \frac{k_{\mathrm{s},\lambda}}{4\pi} \int_0^{4\pi} P(\Omega', \Omega) I_\lambda \, \mathrm{d}\Omega' \ . \tag{3.50}$$

The quantity to be determined is the spectral intensity, I_λ, which is defined as the energy emitted per unit time per unit small wavelength interval around λ, per unit elemental projected surface area normal to the $\vec{\Omega}$ direction and into a unit elemental

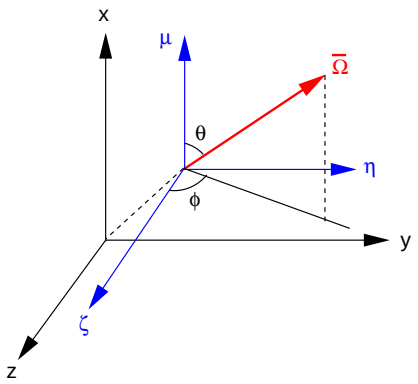

Figure 3.10: Direction cosines in the Cartesian coordinate system

solid angle centered around the direction $\vec{\Omega}$ [12]. The left-hand side of the equation represents the gradient of the intensity in the direction of propagation ($\vec{\Omega}$). The first two terms on the right-hand side represent the attenuation of directional intensity due to absorption and out-scattering, with $k_{a,\lambda}$ and $k_{s,\lambda}$ being the spectral absorption and scattering coefficients, respectively. The third term represents the augmentation of the intensity due to emission, where $I_{b,\lambda}$ is the black-body intensity. The fourth term represents the contribution to directional intensity due to in-scattering from the surrounding medium. $P(\Omega', \Omega)$ is the probability that radiation propagating in direction Ω' is scattered into direction Ω. This equation is an integrodifferential equation, which is difficult to solve in multidimensional geometries.

An approximation often made in radiation calculations is assuming that the scattering of radiation is negligible. Typical soot particle diameters are between 30 nm and 65 nm, and due to their small sizes, scattering is negligible in comparison to absorption, as can be shown by the Mie theory [82,83]. Scattering of radiation becomes important for flames with larger particles such as pulverized coal, char, fly-ash etc. Thus, a scattering coefficient of zero ($k_{s,\lambda} = 0$) can be assumed. The RTE then reduces to a differential equation, which is easier to solve than an integrodifferential equation.

Also, as shown in Figure 3.10, a direction $\vec{\Omega}$ can be expressed in terms of its direction cosines (ζ, η, μ), which are defined as

$$\zeta = \sin\theta\cos\phi \quad , \quad \eta = \sin\theta\sin\phi \quad , \quad \mu = \cos\theta \ . \tag{3.51}$$

The RTE in Cartesian coordinates can now be expressed as

$$\mu\frac{\partial I_\lambda}{\partial x} + \eta\frac{\partial I_\lambda}{\partial y} + \zeta\frac{\partial I_\lambda}{\partial z} = -k_{a,\lambda}I_\lambda + k_{a,\lambda}I_{b,\lambda} \ . \tag{3.52}$$

Thus, in general, the intensity is a function of three spatial coordinates, two angles and the wavelength. Once the intensity distribution is solved for, the divergence of the radiative flux vector can be obtained as

$$\operatorname{div}\vec{F} = \int_0^\infty k_{\mathrm{a},\lambda}[4\pi I_{\mathrm{b},\lambda} - G_\lambda]\mathrm{d}\lambda \quad \text{with} \quad G_\lambda = \int_{\Omega=0}^{4\pi} I_\lambda \mathrm{d}\Omega \tag{3.53}$$

where the term $4\pi k_{\mathrm{a},\lambda} I_{\mathrm{b},\lambda}$ represents the local rate of emission, and $k_{\mathrm{a},\lambda} G_\lambda$ represents the local rate of absorption per unit volume. G_λ is called the irradiance and is obtained by integrating the intensity over all directions. Since $I_{\mathrm{b},\lambda}$ and G_λ are spectral quantities, the above equation involves integration over the entire spectrum.

The optical thickness (X_λ) of a medium is defined as

$$X_\lambda = k_{\mathrm{a},\lambda}.L_{\mathrm{e}} \ , \tag{3.54}$$

where L_{e} is the beam length. Since the different rays have different beam lengths, depending on how they pass through the flame, a mean beam length can be defined [12]. If the optical thick is smaller than 1, the medium is called optically thin, and if X_λ is much greater than 1, the medium is optically thick. Optically thin media do not absorb much radiation, and hence the irradiance G_λ can be assumed to be zero. The source term in the energy equation for optically thin media is much simplified and is

$$\operatorname{div}\vec{F} = \int_0^\infty 4\pi k_{\mathrm{a},\lambda} I_{\mathrm{b},\lambda}\mathrm{d}\lambda \ , \tag{3.55}$$

which does not depend on the radiative intensity I_λ. Since the black body intensity $I_{\mathrm{b},\lambda}$ is only a function of the temperature, no RTE needs to be solved. The optically thin assumption overestimates the radiative heat loss in the medium, as the medium is only assumed to emit radiation, without re-absorbing [84]. However, in order to determine the optical thickness, the absorption coefficients $k_{\mathrm{a},\lambda}$ need to be determined for all the radiating species. These are themselves highly dependent on the temperature, which cannot be obtained without a good radiation model. Thus, a radiation model needs to be used before it the optical thickness of the medium can be calculated.

The solution of the RTE (Equation (3.52)) presents two major problems: determination of the radiative properties (absorption coefficients) and solution methods for the differential equation. Also, the effects of turbulence on radiation need to be taken into account.

3.4.1 Radiative properties

Combustion products such as CO_2, H_2O and soot are strong absorbers and emitters of radiant energy. Prediction of their radiative properties is not an easy task due to the wavelength dependence of these properties and uncertainties about the volume fractions, sizes and concentrations. There exist several levels of sophistication

of prediction methods in the literature, but it should be consistent with the level of sophistication of other models used (such as the chemistry or turbulence model) and should be compatible with the models used to solve the RTE. Non-luminous flame radiation is concentrated in gaseous absorption bands in the infrared spectrum, produced by various types of transitions between the molecular energy states, particularly the vibration-rotation states. In luminous flames, a continuum radiation in the visible and infrared spectrum is emitted by soot which contributes to the luminosity of the flame [85]. Several models exist, which can predict radiative properties of gases. A brief introduction to the main ones will be given and only the model used here will be described in some detail.

Radiative properties of gases:

Gaseous radiation occurs along discrete lines in the spectrum due to the transitions between energy levels. Exact results can be obtained by line-by-line calculations which require the analysis of each discrete absorption-emission line, which is impractical for practical flames. In practical systems, pressure-broadening of spectral lines results in bands. Theoretical models known as narrow-band models (NBM) describe the spectral emissivity over a small wavelength range for each band [91]. They require an intensive and detailed library of input data and large computational effort. Although narrow-band models together with line-by-line models are the most general and accurate models to predict radiative properties of mixtures of gases, they are too computationally expensive to be practical. Narrow-band models have been used in simple laminar flames [92, 93], but the RTE needs to be solved several hundred times depending on the number of bands involved [94].

The exponential wide band model (EWBM) [96] involves dividing the spectrum into wide bands (of the order of 20 for a CO_2-H_2O mixture) and prescribing an exponential variation of spectral parameters within the wide band. It requires a much smaller database as compared to the NBM, but it still requires solving the RTE a minimum of 11 times [94]. Engine simulations are time-dependent and since the RTE is a complicated equation to solve, it is expected to be computationally expensive to solve it for a single wavelength. Hence, the number of times the RTE needs to be solved has to be kept to a minimum in order to keep the model feasible for engine simulations.

The minimum number of times the RTE needs to be solved is once per time step: if the medium is assumed to be grey, its radiative properties are independent of the wavelength. The emissivities of the gases are then usually given by polynomials which are determined by comparison with more detailed models [97]. These correlations are not as accurate as the NBM or the EWBM, but are computationally feasible enough to be used in engine calculations.

The weighted sum of grey gases model (WSGGM) is a good bridge between the more detailed models like the NBM and the EWBM and the simplified grey gas models. Here, the total emissivity of a non-grey gas can be represented by the weighted sum of the emissivities of a small number of grey gases [98], i.e.,

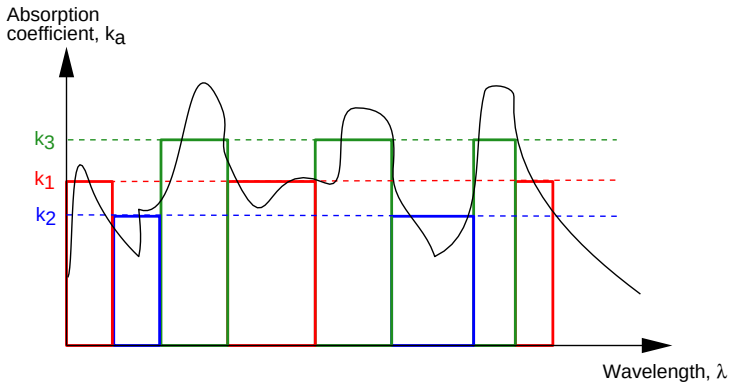

Figure 3.11: Schematic representation of the treatment of the spectral dependence of the absorption coefficient using the WSGGM with three grey gases

$$\varepsilon = \sum_{i=1}^{N_\mathrm{g}} w_i(T) \cdot (1 - \exp^{-k_{i,p} p L_\mathrm{e}}) \ , \tag{3.56}$$

where w_i are the weights as functions of the temperature, $k_{i,p}$ are the constant coefficients, p is the partial pressure of the radiating gas (in case of more gases, it is the sum of the partial pressures of the radiating gases), and L_e is the beam length. The product $k_{i,p}p$ is the absorption coefficient of grey gas i.

This equation can be interpreted as follows: The emission-absorption spectrum of a non-grey gas can be divided into N_g absorption bands over which the absorption coefficient ($k_i = k_{i,p}p$) is taken to be constant. Each band emits a fraction of the total spectrum blackbody radiation, and this fraction is the weighting factor w_i. Figure 3.11 shows a schematic representation of this method for $N_\mathrm{g} = 3$. The three bands (represented by different colors) have constant absorption coefficients k_1, k_2 and k_3. Since the absorption coefficients are considered constant, the band limits can change. The parameters $k_{i,p}$ and w_i are obtained by fitting the data obtained from the NBM or the EWBM. Thus, although the WSGGM equation (Equation (3.56)) is mathematically a non-linear quadrature curve fitting, its coefficients can be related to physical quantities [94].

The RTE can now be solved for each of the bands with the constant absorption coefficient k_i and black-body emissive power weighted by w_i [14, 95, 99]. For each band i, the RTE is written as

$$\mu \frac{\partial I_i}{\partial x} + \eta \frac{\partial I_i}{\partial y} + \zeta \frac{\partial I_i}{\partial z} = -k_i \cdot I_i + k_i w_i I_\mathrm{b} \ , \tag{3.57}$$

and the total intensity over the entire spectrum is given by summing the individual contributions over all the bands (or grey gases N_g),

i	$k_{i,p}$	$b_{i,1} \times 10^1$	$b_{i,2} \times 10^4$	$b_{i,3} \times 10^7$	$b_{i,4} \times 10^{11}$
			$p_w/p_c = 1$		
1	0.4303	5.150	-2.303	0.9779	-1.494
2	7.055	0.7749	3.399	-2.297	3.770
3	178.1	1.907	-1.824	0.5608	-0.5122
			$p_w/p_c = 2$		
1	0.4201	6.508	-5.551	3.029	-5.353
2	6.516	-0.2504	6.112	-3.882	6.528
3	131.9	2.718	-3.118	1.221	-1.612

Table 3.1: Coefficients for the WSGGM for a CO_2-H_2O mixture

$$I = \sum_i^{N_g} I_i \ . \tag{3.58}$$

The total black body intensity I_b over the entire spectrum is given by

$$I_b = \frac{\sigma}{\pi} T^4 \ , \tag{3.59}$$

where σ is the Stefan-Boltzmann constant ($\sigma = 5.67 \times 10^{-8}$ W/(m^2 K^4)). Several values of $k_{i,p}$ and w_i are available in the literature [100–102]. The temperature dependence of w_i is usually expressed in terms of a polynomial,

$$w_i = \sum_{j=1}^{J} b_{i,j} T^{j-1} \ . \tag{3.60}$$

Typical values of $k_{i,p}$ and $b_{i,j}$ are given in Table 3.1 for 2 values of the ratio of the H_2O partial pressure (p_w) to the CO_2 partial pressure (p_c).

A comparison between the WSGGM and the NBM has been reported in the literature for simple systems [103]. Minor differences in the calculated radiative fluxes were observed and the NBM was 50 times more expensive than the WSGGM, as about 200 narrow bands were used in NBM, while only three grey gases were used in the WSGGM.

Radiative properties of soot:

Soot emits mostly continuum radiation in the infrared and visible spectrum. Accurate prediction of the soot emissivity can be obtained if information on the optical properties, size distribution and shape is known. A classical model used to predict the

radiative properties of particles is the Mie theory [82], named after Mie's exact solution of Maxwell's equations for the scattering of an incident plane wave on a sphere. From the Mie theory, the radiative properties of soot depend on the size parameter, $\alpha = \pi d_s/\lambda$ (where d_s is the soot diameter) and the optical constants n and κ, which themselves depend somewhat on the wavelength. For soot particles which are small, the Mie theory implies that the scattering cross section depends on α^4 and the absorption cross section depends on α to the first power. Thus, scattering is very small compared to absorption.

In the limit of $\alpha << 1$, the Mie equation reduces to the Rayleigh limit, and the absorption coefficient of soot is given by [85]

$$k_{\text{soot},\lambda} = \frac{36\pi n\kappa}{(n^2-\kappa^2+2)^2+4n^2\kappa^2} \cdot \frac{f_v}{\lambda} \ . \tag{3.61}$$

However, experimental investigations have demonstrated that soot emission is largely wavelength independent [104]. Thus, by choosing appropriate values of n and κ, the above equation can be approximated as [105]

$$k_{\text{soot},\lambda} = \frac{C_0}{\lambda} \cdot f_v \ , \tag{3.62}$$

where C_0 is a constant. Integrating this over the entire spectrum, the grey soot absorption coefficient can be obtained as

$$k_{\text{soot}} = \frac{1}{\sigma T^4} \int_0^\infty k_{\text{soot},\lambda} e_{b,\lambda} \mathrm{d}\lambda = 3.6 \frac{C_0}{C_2} f_v T \ , \tag{3.63}$$

where $e_{b,\lambda}$ is the black body emissive power and C_2 is Planck's second constant ($C_2 = 1.4388$ cm.K).

C_0 is actually a function of the wavelength, but can be assumed to be constant. A value of $C_0 = 4.64$ has been suggested [106, 107].

Based on this absorption coefficient, the emissivity can be obtained as

$$\varepsilon_s = 1 - \exp^{-k_{\text{soot}} L_e} \ . \tag{3.64}$$

Figure 3.12 shows a comparison between soot emissivities calculated by this method and detailed wavelength dependent calculations reported in the literature [108]. One sees a very good comparison with a reduction in computational time.

In order to account for gaseous and soot radiation, the RTE (Equation (3.57)) has to be modified. Since soot radiates in a grey manner, its absorption coefficient is the same in each of the gas bands, and the final RTE in each band can be written as

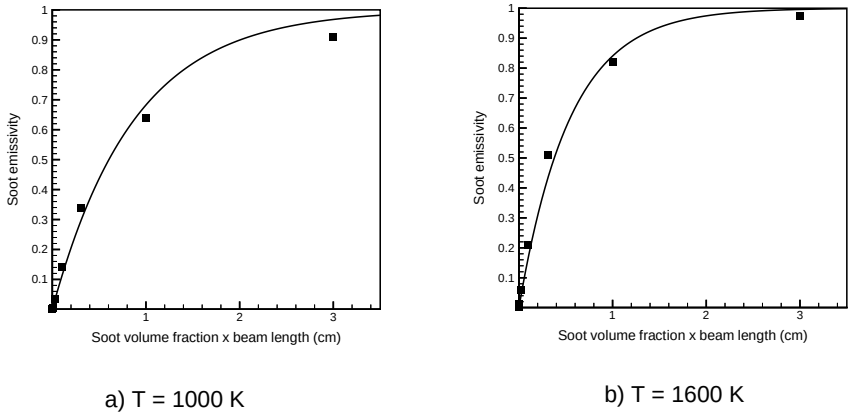

Figure 3.12: Comparison of soot emissivities using the simplified grey model (lines, Equation 3.63) and using detailed spectral calculations [108] (symbols) for a) $T = 1000$ K and b) $T = 1600$ K

$$\mu\frac{\partial I_i}{\partial x} + \eta\frac{\partial I_i}{\partial y} + \zeta\frac{\partial I_i}{\partial z} = -(k_i + k_{\text{soot}}) \cdot I_i + (k_i + k_{\text{soot}}) w_i I_{\text{b}} \ . \tag{3.65}$$

3.4.2 Solution methods for the RTE

Solution of the RTE is difficult due to its spectral and angular dependence. The first general numerical procedure for handling the radiative transfer equation was Hottel's zone method [98]. Here, the surface and volume of the enclosure is divided into a number of zones, each assumed to have a uniform distribution of temperature and radiative properties. The direct exchange areas between the surface and the volume elements are evaluated and a set of nonlinear algebraic equations are solved. Hence, the zonal method cannot be readily adopted for complicated geometries, since numerous exchange factors need to evaluated and stored. The zonal method can be computationally prohibitive if the same grid scheme used in the CFD code is used, making it difficult to couple it with the CFD code. Statistical methods, like the Monte-Carlo method [109, 110] are widely regarded as accurate. The method consists of simulating a finite number of photon histories. Each photon history is started by assigning a set of values to the photon, its initial energy, position and direction. Then, the absorption and scattering coefficients are sampled and it is determined whether the photon is absorbed or scattered by the gas or soot. If it is absorbed, the history is terminated. If scattered, the distribution of scattering angles is sampled and a new direction is assigned to the photon. However, this method is slow and is not justified in applications where radiative heat transfer is not the governing heat transfer mode.

Flux methods, also known as differential approximations, offer a high degree of computational accuracy and have been widely used in combustion simulations [111]. The angular dependence of the radiative intensity is the major source of complications in

the RTE as all possible directions need to be taken into account. It is, therefore, desirable to separate the angular dependence from its spatial dependence to simplify the governing equations. If it is assumed that the intensity is uniform on given intervals of the solid angle, then the RTE would be reduced to a series of coupled linear differential equations. This procedure yields the flux methods. Examples of flux methods are the discrete ordinates method [13] and the spherical harmonics method [112]. The discrete ordinates method has been used in several combustion simulations and has been shown to be very efficient and accurate [14, 113–117].

In the discrete ordinates method, the solid angle of 4π is divided into several divisions, the size of which is determined from quadrature schemes. The exact transport equation is then solved for this set of discrete directions spanning the 4π solid angle. Each direction is represented by a set of direction cosines. Thus, the RTE (Equation (3.65)) is replaced by a set of equations for each direction m,

$$\mu_m \frac{\partial I_{i,m}}{\partial x} + \eta_m \frac{\partial I_{i,m}}{\partial y} + \zeta_m \frac{\partial I_{i,m}}{\partial z} = -(k_i + k_{\text{soot}}) \cdot I_{i,m} + (k_i + k_{\text{soot}}) w_i I_{\text{b}} \ , \tag{3.66}$$

where the index i represents the grey gases in the WSGGM, and the index m represents the direction. The overall intensity for each grey gas is given by a summation over all directions (N_{d}) with a weighting factor (W_m) for each direction,

$$\int_0^{4\pi} I_i(\Omega) \mathrm{d}\Omega = \sum_0^{N_{\text{d}}} W_m I_{i,m} \ . \tag{3.67}$$

The accuracy of the scheme depends on the number of discrete directions used, which depends on the order of the discrete ordinates approximation. A unit sphere is constructed around each point in space, and the number of quadrature points used between [-1;1] is counted. Since intensities along both positive and negative directions need to be solved for, this number (n) is always even. In a three-dimensional problem, each octant of this sphere contains $(n/2) + [(n/2) - 1] + [n/2) - 2] + ... + 1 = n(n + 2)/8$ quadrature points. For the eight octants, there is a total of $N_{\text{d}} = n(n + 2)$ ordinates [119]. Figure 3.13 shows one such discrete representation in one octant for $n = 6$. Thus, $n(n+2)$ equations need to be solved simultaneously at each node. Depending on the value of n (and hence N_{d}) chosen, different orders of approximation are obtained. $n = 2$ results in 8 directions (called the S_2 method), $n = 4$ results in 24 directions (called the S_4 method), $n = 6$ results in 48 directions (called the S_6 method), etc. The higher the approximation order, the more the number of directions to be solved for, and the higher is the accuracy of the scheme.

The direction cosines used in this thesis are shown in Table 3.2 [114].

The above equation can now be spatially discretized using the control-volume method and can, thus, be easily coupled with CFD codes which are also based on the control-volume discretizing schemes. Multiplying Equation (3.66) with $\mathrm{d}x\mathrm{d}y\mathrm{d}z$ and integrating over volume elements, one gets

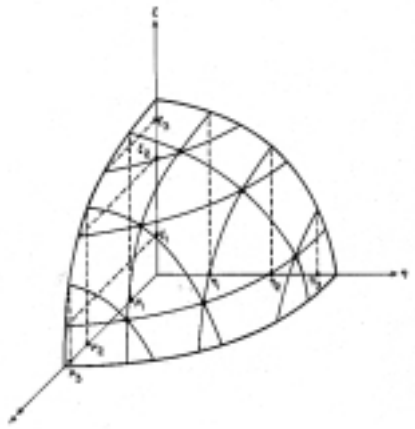

Figure 3.13: Discrete directions for $n = 6$ [118]

Method	μ_m	η_m	ζ_m	W_m
S_2	0.57735	0.57735	0.57735	$\pi/2$
S_4	0.29588	0.90825	0.29588	$\pi/6$
	0.90825	0.29588	0.29588	$\pi/6$
	0.29588	0.29588	0.90825	$\pi/6$
S_6	0.18387	0.96560	0.18387	0.16095
	0.69505	0.69505	0.18387	0.36265
	0.96560	0.18387	0.18387	0.16095
	0.18387	0.69505	0.69505	0.36265
	0.69505	0.18387	0.69505	0.36265
	0.18387	0.18387	0.96560	0.16095

Table 3.2: Quadratures for all the directions in each octant in the discrete ordinates method [114]

$$\mu_m(A^{\mathrm{E}}I^{\mathrm{E}}_{i,m} - A^{\mathrm{W}}I^{\mathrm{W}}_{i,m}) + \eta_m(A^{\mathrm{N}}I^{\mathrm{N}}_{i,m} - A^{\mathrm{S}}I^{\mathrm{S}}_{i,m}) + \zeta_m(A^{\mathrm{T}}I^{\mathrm{T}}_{i,m} - A^{\mathrm{B}}I^{\mathrm{B}}_{i,m}) = -(k_i + k_{\mathrm{soot}}) \cdot V \cdot I_{i,m} + V(k_i + k_{\mathrm{soot}})w_i I_{\mathrm{b}} \ , \tag{3.68}$$

where the superscripts N, S, E, W, T, and B denote the north, south, east, west, top and bottom faces of a control volume as shown in Figure 3.14, A denotes the area of a face and V the volume.

The intensities at the faces can be expressed in terms of the intensity at the center ($I_{i,m}$) using

$$(1 + f)I_{i,m} = I^{\mathrm{E}}_{i,m} + fI^{\mathrm{W}}_{i,m} = I^{\mathrm{N}}_{i,m} + fI^{\mathrm{S}}_{i,m} = I^{\mathrm{T}}_{i,m} + fI^{\mathrm{B}}_{i,m} \ , \tag{3.69}$$

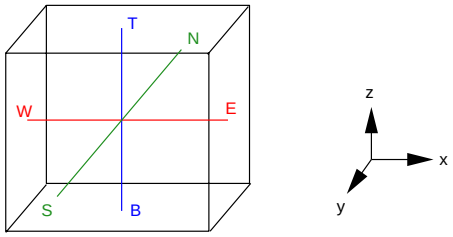

Figure 3.14: A typical control volume

where $f = 1/2$ results in the diamond-difference scheme [119], $f = 0$ results in an upwind scheme and $f = 1$ results in a central-difference scheme. Thus, the intensity at the center of the volume element can be written in terms of known quantities as

$$I_{i,m} = \frac{\mu_m A I_{i,m}^{\mathrm{W}} + \eta_m B I_{i,m}^{\mathrm{S}} + \zeta_m C I_{i,m}^{\mathrm{B}} + V(k_i + k_{\mathrm{soot}}) w_i I_{\mathrm{b}}}{\mu_m A + \eta_m B + \zeta_m C + V(k_i + k_{\mathrm{soot}})} \tag{3.70}$$

with

$$A = A^{\mathrm{W}} + f A^{\mathrm{E}} \quad , \quad B = A^{\mathrm{S}} + f A^{\mathrm{N}} \quad , \quad C = A^{\mathrm{B}} + f A^{\mathrm{T}} \ . \tag{3.71}$$

In order to solve these equations, boundary conditions are needed. These are generated by expressing the intensity leaving the surface along the ordinate direction m as the sum of the emitted and reflected intensities,

$$I_i(\vec{\Omega}^+) = \varepsilon_{\mathrm{w}} I_{\mathrm{b,w}}(\vec{\Omega}^+) + \frac{(1-\varepsilon_{\mathrm{w}})}{\pi} \int_0^{2\pi} I_i(\vec{\Omega}^-) \cdot (\vec{n}, \vec{\Omega}^-) \mathrm{d}\Omega^- \tag{3.72}$$

where the subscript w stands for the wall. ε_{w} is the emissivity of the wall and $I_{\mathrm{b,w}}$ is the black body intensity at the wall temperature. $\vec{\Omega}^+$ indicates vectors which are directed into the inside of the chamber, while $\vec{\Omega}^-$ denotes vectors which point towards the wall. The above equation was written assuming that the walls are diffusely emitting-reflecting. The term "diffuse" means that the intensity of the reflected radiation is the same in all directions. This assumption has been proven to be valid, both in experimental and theoretical studies [12]. This can be shown schematically in Figure 3.15 where the radiation falling on the wall (denoted by $\vec{\Omega}^-$) has an intensity that is direction-dependent, while the reflected and emitted intensity (denoted by $\vec{\Omega}^+$) is diffuse.

The boundary condition is written in the discrete form using

$$I_{i,m} = \varepsilon_{\mathrm{w}} I_{\mathrm{b,w}} + \frac{(1-\varepsilon_{\mathrm{w}})}{\pi} \sum_{N_d} l_m W_m I_{i,m} \ , \tag{3.73}$$

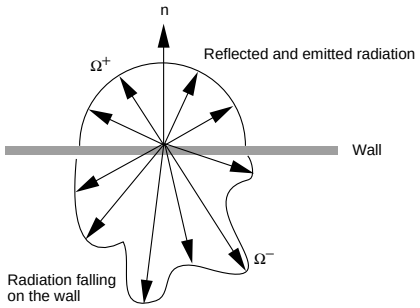

Figure 3.15: Boundary conditions for the discrete ordinates method [112]

where l_m is the direction cosine between m and the coordinate direction normal to the surface. Equation (3.70) is written for each volume element and Equation (3.73) is written for each boundary element. This provides a set of linear differential equations and boundary conditions sufficient to solve for the unknown $I_{i,m}$. The local energy flux for each grey gas i is then given by

$$q_{i,\mathrm{rad}} = \sum_{N_d} l_m W_m I_{i,m} \quad . \tag{3.74}$$

The solution procedure is iterative as the boundary conditions are themselves functions of the dependent variable (the intensity). It can be outlined as follows:

1. Calculations are initiated by assuming the radiative flux at the wall (usually assumed to be zero).
2. Using Equation (3.73), and using the assumed flux, the intensities at the walls are calculated.
3. Using Equation (3.70) for the cell center intensity ($I_{i,m}$) and Equation (3.69) for the downstream and upstream intensities ($I^{\mathrm{E}}_{i,m}$, $I^{\mathrm{W}}_{i,m}$, $I^{\mathrm{N}}_{i,m}$, $I^{\mathrm{S}}_{i,m}$, $I^{\mathrm{T}}_{i,m}$ and $I^{\mathrm{B}}_{i,m}$), the intensities from wall to wall for each direction m can be found.
4. Using these new intensities, the wall flux can be obtained using Equation (3.74) and with these fluxes, new boundary conditions can be obtained.
5. If the fluxes calculated are equal to the assumed fluxes, the procedure has converged. If not, the assumed fluxes are set equal to the calculated flux and the procedure (from 2. onwards) is repeated.

Lastly, the differencing factor (f) in Equation (3.69) needs to be chosen. Setting $f = 0$ leads to upwind differencing which always leads to non-negative intensities. Central differencing ($f = 1$) may lead to non-physical negative intensities due to the extrapolation in Equation (3.69), but it is more accurate than upwind differencing [114]. Hence, calculations are always initiated with $f = 1$. In case negative intensities are encountered, the value of f is reduced globally till negative intensities are removed.

3.4.3 Turbulence-radiation interactions

Turbulence-radiation interactions need to be taken care of in flames, similar to turbulence-chemistry coupling. The interactions and coupled effects are more important for luminous (sooty) flames than for non-luminous flames [86]. Turbulence can affect radiative transfer through fluctuations in temperature, species and soot concentrations, which in turn cause fluctuations in the absorption coefficients. Traditional modeling of radiative heat transfer has ignored these interactions, i.e., all radiative intensities, fluxes and properties have been based on mean properties [87, 88]. However, experimental [89] and modeling [86] work indicate that this assumption can cause large errors. Hence, the RTE needs to be averaged to give

$$\mu\frac{\partial\overline{I}_\lambda}{\partial x}+\eta\frac{\partial\overline{I}_\lambda}{\partial y}+\zeta\frac{\partial\overline{I}_\lambda}{\partial z}=-\overline{k_{\mathrm{a},\lambda}I_\lambda}+\overline{k_{\mathrm{a},\lambda}I_{\mathrm{b},\lambda}}\ . \tag{3.75}$$

The first term on the right-hand side is difficult to evaluate as it involves the fluctuating directional intensity which is dependent on both the local and the far-field properties. These fluctuations can be ignored to first-order accuracy, if the radiance at a local point is assumed to be negligibly affected by the local turbulent fluctuations of the absorption coefficient [86, 90]. The equation reduces to

$$\mu\frac{\partial\overline{I}_\lambda}{\partial x}+\eta\frac{\partial\overline{I}_\lambda}{\partial y}+\zeta\frac{\partial\overline{I}_\lambda}{\partial z}=-\overline{k_{\mathrm{a},\lambda}}\cdot\overline{I_\lambda}+\overline{k_{\mathrm{a},\lambda}I_{\mathrm{b},\lambda}}\ . \tag{3.76}$$

The mean emissive term and the mean absorption coefficients are functions of the local temperature and species concentrations, which themselves are functions of the mixture fraction (ξ), the temperature (T) and b through the ILDM chemistry model (see Section 3.2). They can be calculated by integrating over a pdf, similar to the one used in the chemistry model (see Section 3.2.4), i.e.,

$$\begin{aligned}\overline{k_{\mathrm{a},\lambda}}&=\int k_{\mathrm{a},\lambda}\tilde{P}(\xi,T,b)\,\mathrm{d}\xi\,\mathrm{d}T\,\mathrm{d}b\ ,\\ \overline{k_{\mathrm{a},\lambda}I_{\mathrm{b},\lambda}}&=\int k_{\mathrm{a},\lambda}I_{\mathrm{b},\lambda}\tilde{P}(\xi,T,b)\,\mathrm{d}\xi\,\mathrm{d}T\,\mathrm{d}b\ .\end{aligned} \tag{3.77}$$

With these mean quantities, the averaged RTE can then be solved for the mean radiative intensity. The exact coupling between the radiation model and KIVA is discussed in Section 4.3.

4 Numerical simulation with KIVA

The previous chapters described the concepts and principles behind the different models. This chapter describes the numerical methods used in KIVA to solve the non-linear coupled system of differential equations, and the coupling between the new models and KIVA.

4.1 Temporal differencing

The temporal differencing is performed with respect to a sequence of discrete times t^n $(n = 0, 1, 2, ...)$. The time interval $\Delta t^n = t^{n+1} - t^n$ is the time step and the integer n is the cycle number. In KIVA, a cycle is performed in three stages or phases. Phase A and B constitute a Lagrangian calculation in which the computational cells move with the fluid. In Phase C, the flow field is frozen and re-mapped onto a new computational mesh in order to account for compression or expansion.

Phase A involves the calculation of the spray droplet collision and breakup terms, the mass and energy source terms due to the chemistry and the spray. The calculation of the droplet processes is done sequentially, always using the most recently obtained droplet properties for calculating changes due to the next physical effect. Droplet oscillation and breakup calculations are done first, followed by droplet collision calculations. The Phase A calculation is completed with updates of particle radii and temperatures due to evaporation and the addition of gravitational acceleration terms to the particle velocities. The source terms for the mass and energy balance equations due to chemistry are also calculated in Phase A. Thus, integration of the source terms over a pdf are also performed here. Since chemistry is handled in an explicit manner in Phase A, the time step Δt used is of importance. For, e.g., the CO_2 mass fraction at time t^{n+1} is calculated as

$$Y_{CO_2}^{n+1} = Y_{CO_2}^{n} + \dot{Y}_{CO_2}^{C,n} \cdot \Delta t^n \quad . \tag{4.1}$$

Due to the explicit time-stepping, the time step Δt^n should not be larger than the smallest chemical time scale. In order to avoid this limitation of the CFD time steps due to chemistry, which could lead to very small time steps increasing the computational time, the above equation is used in a cyclic manner. The smallest chemical time scale at a particular point in state space can be obtained by ILDM using an eigenvalue analysis (Δt^{ILDM}). Thus, the CO_2 mass fraction at each sub-cycle i can be calculated using

$$Y_{CO_2}^{i+1} = Y_{CO_2}^{i} + \dot{Y}_{CO_2}^{C,i} \cdot \Delta t_i^{\mathrm{ILDM}} \tag{4.2}$$

and continuing this process k times till the total time step equals the CFD time step, i.e., until the following equation is satisfied:

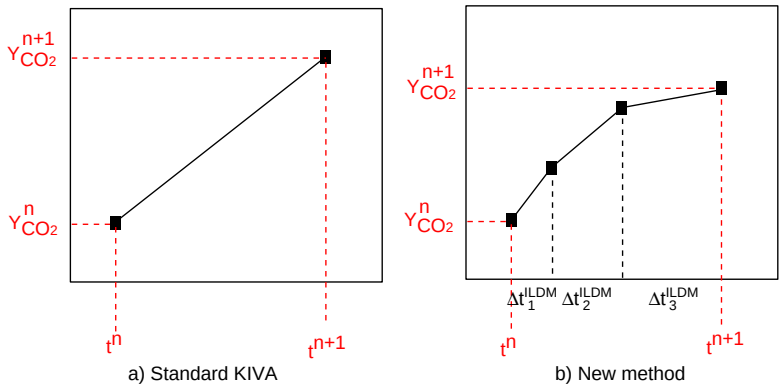

Figure 4.1: Time stepping used for chemistry a) Standard KIVA method and b) New method

$$\sum_{i=1}^{k} \Delta t_i^{\mathrm{ILDM}} = \Delta t^n \quad . \tag{4.3}$$

This process is shown schematically in Figure 4.1. Figure 4.1(a) shows the standard KIVA explicit time stepping, while Figure 4.1(b) shows the new time stepping with smaller time steps.

Phase B calculates in a coupled, implicit fashion the pressure gradient in the momentum equation, the velocity dilation terms in the mass and energy equations, the spray momentum source term, and the terms due to diffusion of mass, momentum and energy. Phase B also calculates the remaining source terms in the turbulence equations. The solution method is based on the SIMPLE (Semi-Implicit Method for Pressure-Linked Equations) [121]. This is an iterative method, where the pressure is frozen and the other flow quantities such as the velocities and the temperatures are solved for. These terms are then frozen and a corrected pressure field is solved for. The pressure fields are then compared and the process is repeated till convergence. Since the species and the turbulence equations are weakly coupled to the flow field solution, these are not included in the SIMPLE iteration loop, and are solved independently.

Phase C is the rezone phase, where the convective transport associated with moving the mesh relative to the fluid is calculated. At the end of Phase C, the cell temperatures and pressures are calculated from the state relations, while the density is calculated by summing the individual species densities, i.e.,

$$\overline{\rho} = \sum_i \overline{\rho}_i \tag{4.4}$$

Thus, the KIVA code expects a certain number of transport equations to be solved for all the species involved. These are used not only to calculate the density, but also

to calculate the temperature from the internal energy. Since all these operations are carried out in different phases (chemistry in Phase A, diffusion of species in Phase B and final calculation of the density and the temperature in Phase C), transport equations need to be solved for a certain number of species. The ILDM method only requires that a transport equation for the progress variable should be solved. However, the KIVA code structure prevents that, e.g., solving only for the progress variable and freezing the other species obtained in Phase A with ILDM throughout Phase B and C amounts to neglecting the effects of diffusion and convection. However, as mentioned in Chapter 3.2, the detailed mechanism involves 43 species, and solving for all 43 species is too computationally expensive in an engine. Hence, a select number of species is solved for (here 11, C_7H_{16}, O_2, N_2, CO_2, H_2O, H, H_2, O, OH, CO and NO) which make up the majority of the mixture. All thermodynamic calculations were done by KIVA using these species.

4.2 Spatial differencing

The spatial differencing in KIVA is based on a finite volume method called the ALE (arbitrary Lagrangian Eulerian) [120] method. Spatial differences are formed on a mesh that subdivides the computational region into a number of small hexahedrons. The corners of the cells, or vertices, can be assigned positions that are arbitrarily specified functions of time, thereby allowing a Lagrangian, Eulerian, or mixed description. The mesh can conform to curved boundaries and can move to follow changes in the combustion chamber geometry [6]. The conservation equations are spatially differenced using the control volume method. A typical cell is shown in Figure 4.2. The vertices are conventionally numbered as shown. The cells are indexed by integers (i, j, k), which are its coordinates in logical space. The indices (i, j, k) also label the vertices, such that vertex (i, j, k) is vertex 4 of cell (i, j, k).

Auxiliary cells are also defined which are centered about the vertices. These cells are called momentum cells as their main use is in differencing the momentum equations. The momentum cell (i, j, k) is centered about vertex (i, j, k).

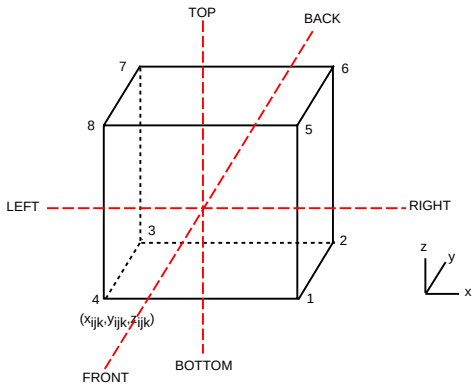

Figure 4.2: A typical KIVA cell

In the ALE method, the velocities are located at the vertices, which is convenient because no interpolation is required when determining vertex motion in the Lagrangian phase of the calculation. Thermodynamic quantities such as temperature, species concentrations, etc. are located at cell centers. Spatial differences are performed by integrating the differential term over the volume of a typical cell. The general transport equation

$$\mathrm{div}(\rho\vec{u}\phi) = \mathrm{div}(\Gamma_\phi \,\mathrm{grad}\,\phi) + S_\phi \tag{4.5}$$

can be integrated over the control volume,

$$\int_V \mathrm{div}(\rho\vec{u}\phi)\mathrm{d}V = \int_V \mathrm{div}(\Gamma_\phi \,\mathrm{grad}\,\phi)\mathrm{d}V + \int_V S_\phi \mathrm{d}V \ . \tag{4.6}$$

Using the Gauss theorem, the volume integral can be converted into surface integrals to obtain

$$\int_A \rho\phi(\vec{u}\mathrm{d}\vec{A}) = \int_A \Gamma_\phi(\mathrm{grad}\,\phi\mathrm{d}\vec{A}) + \int_V S_\phi \mathrm{d}V \tag{4.7}$$

Assuming that ρ, Γ, $\vec{u}$ and ϕ are homogeneous on the surfaces, the integral can be converted into a summation over the cell faces A_j, i.e.,

$$\sum_j [(\rho\phi)_j \cdot (u_j A_j)] = \sum_j [\Gamma_{\phi,j} \cdot ((\mathrm{grad}\,\phi)_j A_j)] + \int_V S_\phi \mathrm{d}V \ . \tag{4.8}$$

Here, u_j are the velocity components which are perpendicular to the surfaces A_j.

Figure 4.3 shows the general flow diagram for the KIVA program. The approximate order in which the equations are solved and the different phases are shown.

4.3 Coupling between KIVA and new models

Figures 4.4, 4.5 and 4.6 show the coupling between KIVA and the new models for ignition, chemistry and radiation described in Chapter 3. Since all these physical processes are handled in Phase A, only this phase is shown, i.e., the influence of diffusion (in Phase B) and convection (in Phase C) is not shown.

The ignition model requires as input the means of the mixture fraction ($\tilde{\xi}$), the mixture fraction variance ($\widetilde{\xi''^2}$), the temperature ($\tilde{T}$), the pressure ($\overline{p}$), the CO concentration ($\widetilde{C_{\mathrm{CO}}}$) and the variance of the CO concentration ($\widetilde{C''^2_{\mathrm{CO}}}$). These parameters enter a pdf

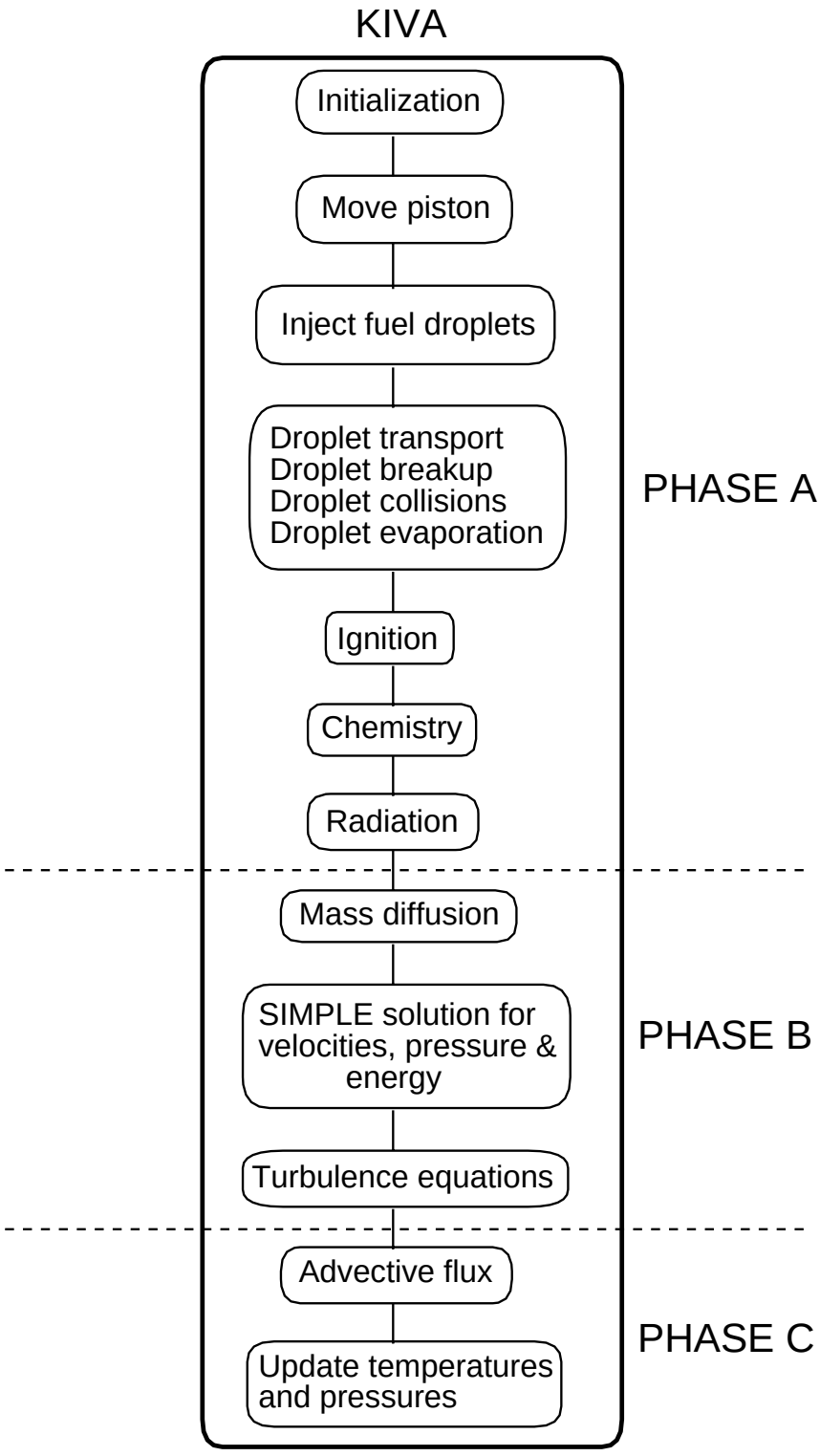

Figure 4.3: General flow diagram for KIVA

module which constructs the pdf $\tilde{P}(\xi, T, C_{\mathrm{CO}})$ and integrates the CO reaction rate over this pdf. Values of the laminar reaction rate as a function of ξ, T, p and C_{CO} are read

from an ignition table. Using this reaction rate, the new CO concentration is found in an explicit manner, and is compared to a critical concentration to determine where ignition occurs.

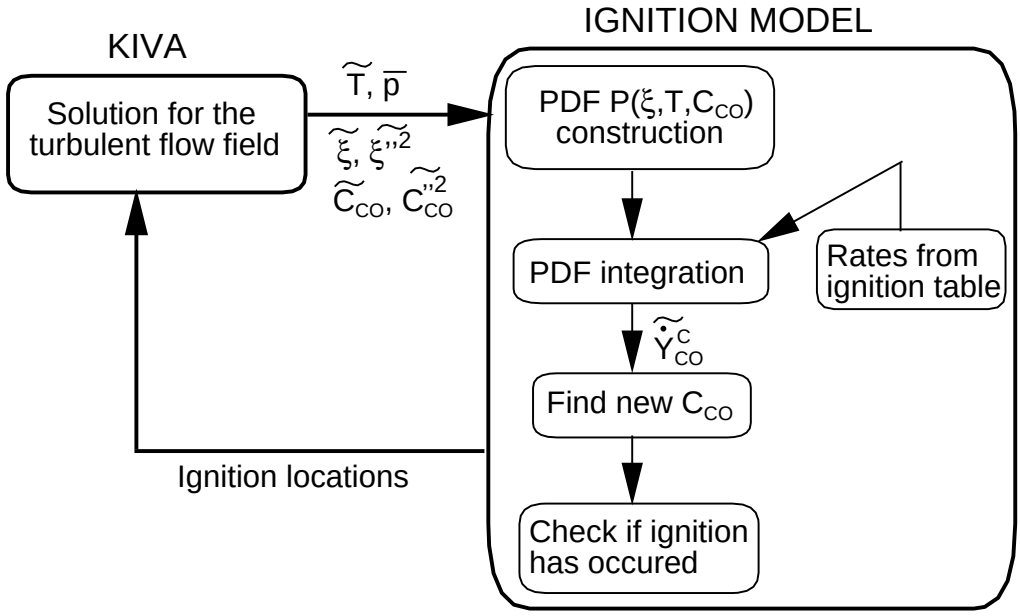

Figure 4.4: Coupling between the ignition model and KIVA

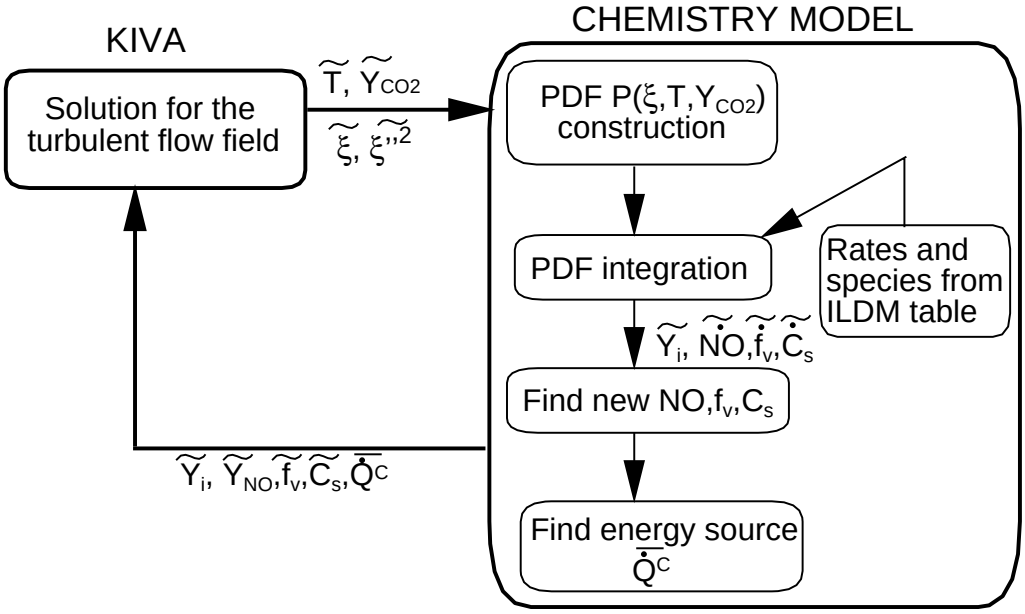

Figure 4.5: Coupling between the chemistry model and KIVA

The chemistry model requires the means of the mixture fraction ($\tilde{\xi}$), the mixture fraction variance ($\widetilde{\xi''^2}$), the temperature ($\tilde{T}$), and the progress variable ($\widetilde{Y_{CO_2}}$). These parameters enter a pdf module which constructs the pdf $\tilde{P}(\xi, T, Y_{CO_2})$. The reaction rate of the progress variable is read from the ILDM table. The new progress variable

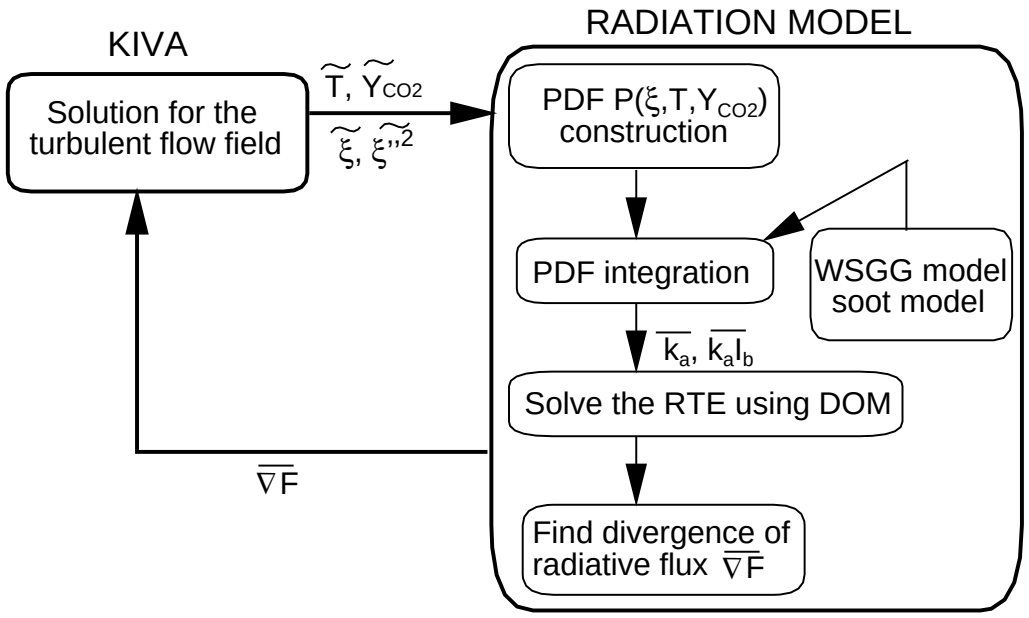

Figure 4.6: Coupling between the radiation model and KIVA

is obtained in an explicit manner (see Section 4.1), and with this new progress variable, the remaining species can be read from the ILDM table. Several variables are integrated over this pdf, i.e. the species concentrations, the NO source term and the source terms for the soot variables. From the mean species, the mean source term for the internal energy equation is calculated. These all go back to KIVA to continue the turbulent flow field calculation in Phase B and C.

The radiation model requires the temperature field and the radiative properties of the fluid. In order to obtain the mean properties (mean absorption coefficients $\overline{k}_\mathrm{a}$ and mean emissive powers $\overline{k_\mathrm{a} I_\mathrm{b}}$), these are integrated over a pdf. They are obtained from models presented in Chapter 3.4. Using these, the radiative transfer equation (RTE) is solved using the discrete ordinates method (DOM) to obtain the radiative intensity field. Using this, the divergence of the radiative flux vector ($\mathrm{div}\,\vec{F}$) can be obtained which is a sink term in the internal energy equation.

5 Results in a Diesel engine

In this chapter, the results obtained with the complete KIVA code with the new models for ignition, chemistry and radiation will be presented and compared with available experimental data. First, the data used for the simulation, i.e., the initial conditions, the engine conditions and the numerical mesh used will be presented. Then, results concerning cold flow will be presented. Next, results related to the ignition model, i.e., the ignition timing and location will be discussed. The ignition model combined with the chemistry model was then used to simulate the flame propagation and pollutant formation. The pressure in the cylinder and the total pollutants at the end of the cycle could be compared to experimentally obtained values. In the above mentioned simulations, the radiation model was not used, i.e., radiative losses were neglected. Later, the radiation model was added to the simulations. Initially, in order to test the radiation method, the method was used in a simplified geometry with known medium properties, where an analytical solution for the RTE was available, and the results were compared. Later, the radiation model was used in the engine. Instead of starting out with solving the RTE using the discrete ordinates method in the engine which was anticipated to be computationally expensive, it was assumed initially that the mixture is optically thin, and the simulations were compared to those where no radiative heat losses were assumed. On the basis of these simulations, it was seen that radiative heat transfer losses are negligible and this mode of heat transfer could be neglected with no significant loss in accuracy.

5.1 Engine specifications

The Diesel engine simulated was a Caterpillar 3406 heavy-duty truck engine, capable of producing 54 kW at a rated speed of 2100 rpm. The simulations performed were at partial load, i.e., at an engine speed of 1600 rpm. Details of the engine are given in Table 5.1. All walls were maintained at constant temperatures, which are given in Table 5.1. The in-cylinder turbulent flow at intake valve closure was assumed to be homogeneous. The initial value of the turbulent kinetic energy (k) was taken to be 10% of the kinetic energy based on the mean piston speed. The initial value of the turbulent energy dissipation (ϵ) was determined based on the assumed k and an assumed uniform length of 1.423 cm. The results are however insensitive to these initial values [32]. Five different injection timings (or start of injection, SOI) were used, and experimental data [122] were available for all five. The pressure curves (mean cylinder pressure as a function of the crank angle) and the total NO_x and soot concentrations at the end of the cycle were available from experiments.

Since the combustion chamber geometry and the six-hole injector configuration is symmetrical, the entire computational domain was divided into 6 equal sectors, and the computational domain actually simulated was only one-sixth of the total chamber with one nozzle, i.e., only 60° of the chamber in the azimuthal direction was modeled with sector-symmetric boundary conditions at 0° and 60°.

Bore	137.16 mm
Stroke	165.1 mm
Conrod length	263 mm
Piston crown	Mexican hat
Engine speed	1600 rpm
Number of nozzle orifices	6
Injection timing	-7, -4, -1, 2, 5° ATDC
Duration of injection	19.75°
Fuel injected	0.168 g/cycle
Cylinder wall temperature	433 K
Piston wall temperature	553 K
Head temperature	523 K
Initial gas temperature	361.4 K
Spray temperature	341 K
Initial gas composition	
O_2	4.6012×10^{-4} g/cm^3
N_2	1.5337×10^{-3} g/cm^3
CO_2	2.8579×10^{-6} g/cm^3
H_2O	1.2579×10^{-6} g/cm^3

Table 5.1: Caterpillar engine specifications

The numerical mesh used is shown in Figures 5.1 and 5.2. It was created using the KIVA preprocessor, K3-prep, which is especially designed for engine geometries. The cylinder contains 29 cells in the radial direction, 30 cells in the azimuthal direction, and 25 cells in the axial direction. The piston cup contains 20 cells in the radial direction, 30 cells in the azimuthal direction, and 12 cells in the axial direction. Totally, the grid contains about 27000 cells at BDC and about 9800 cells at TDC.

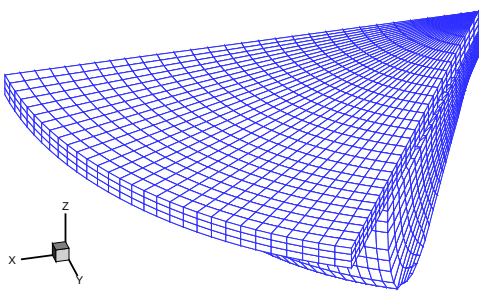

Figure 5.1: Numerical grid used at TDC

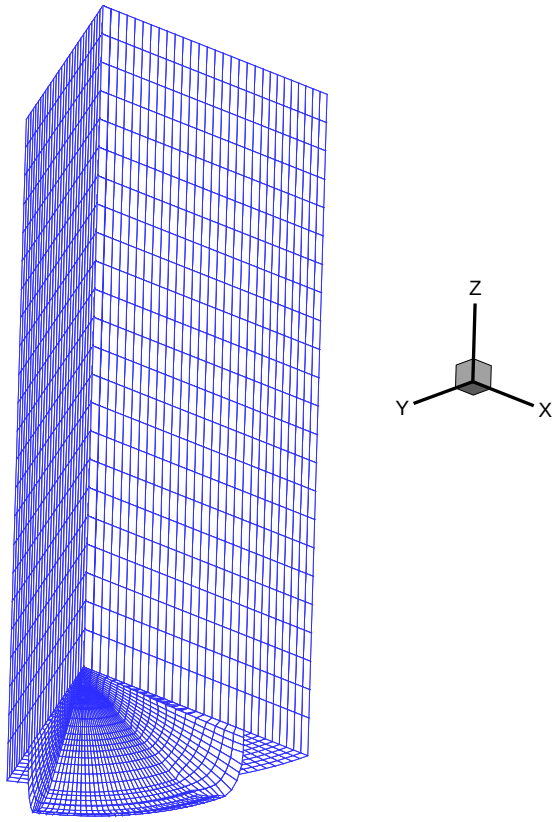

Figure 5.2: Numerical grid used at -144° ATDC (BDC)

5.2 Cold flow

Simulating the engine processes from bottom-dead-center (BDC) to the start of ignition involves simulating the fluid flow processes without the spray and the chemistry models. This means solving the Navier Stokes equations (the momentum, species and energy equations) coupled with the turbulence model. The k-ϵ turbulence model was used in the simulations, as described in Section 2.3.

Figures 5.3 and 5.4 show the turbulent kinetic energy distribution for a slice in the center of the cylinder at two different crank angles: -120° ATDC and -60° ATDC. The numerical mesh used in these slices is also seen. One can recognize a decrease in the number of cells due to the movement of the mesh indicating compression. As can be seen, the turbulent kinetic energy is maximum in the region between the piston wall and the cylinder wall due to the upward movement of the piston at both crank angles. The maximum fluid velocity is about 14.5 m/s at -120° ATDC and increases to about 16.9 m/s at -60° ATDC. One also sees the increase in turbulence with compression, indicated by the higher turbulent kinetic energy values seen at -60° ATDC as compared to those at -120° ATDC.

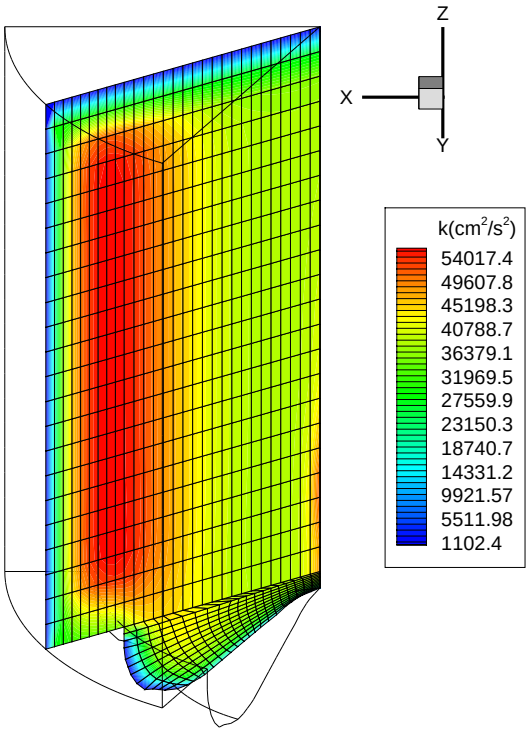

Figure 5.3: Turbulent kinetic energy distribution at -120° ATDC

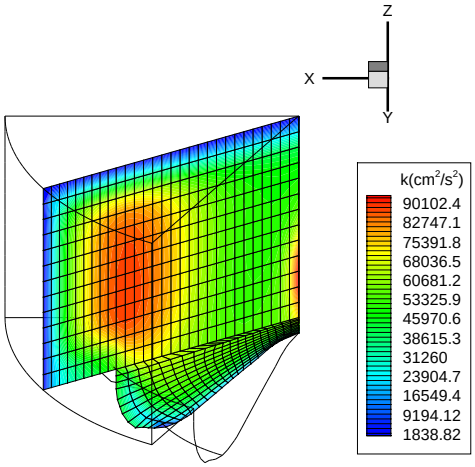

Figure 5.4: Turbulent kinetic energy distribution at -60° ATDC

5.3 Ignition results

In this section, results pertaining to the ignition model will be shown. As an example, results pertaining to the engine simulation with SOI -7° ATDC will be shown. The ignition model is started at the start of injection, and the ignition model consists of tracing a representative ignition species (here CO) whose reaction rate is obtained from detailed chemistry (see Section 3.1).

Figure 5.5 shows the variation in the maximum CO mass fraction as a function of crank angle. At the beginning of injection (in this case, -7° ATDC), a CO mass fraction of 1.0×10^{-10} is assumed as discussed in Section 3.1.3. During the ignition delay time (here 3.46° crank angle or 0.36 ms), the CO mass fraction remains almost constant, and close to ignition, the reaction rate rises rapidly due to chain reactions resulting in a steep increase in the CO mass fraction. Using the ignition criterion described in Section 3.1, ignition was assumed to have taken place when the CO mass fraction exceeded a critical CO mass fraction (assumed to be 0.1).

Figure 5.6 shows the location of the first ignition cell relative to the spray. The size of the droplets shown in the figure correspond to the actual spray droplet sizes and the droplets are colored according to temperature. The coolest and largest droplets are closer to the injector (situated on the cylinder axis). These then break up into smaller droplets as they move into the cylinder and their temperature increases due to heat transfer from the hotter compressed air. As can be seen from Figure 5.6, ignition takes place at the edge of the spray, a little downstream from the injector. Ignition of the mixture very close to the injector is not seen, as the residence time of the fuel there is too low for sufficient chemical reactions to have taken place. Also, the temperatures there are very low due to the lower temperature of the injected fuel as compared to the surrounding air. The temperatures in the fuel-rich regions are lower than in the

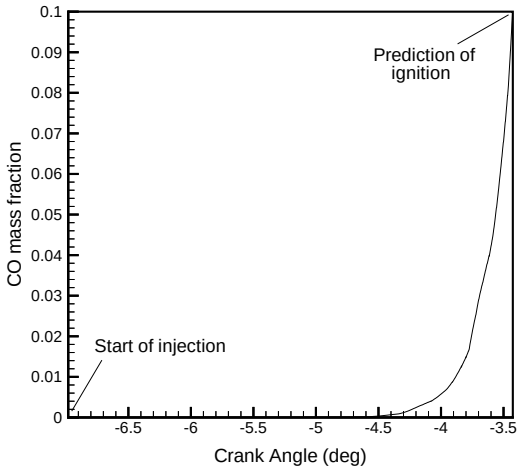

Figure 5.5: Maximum value of the ignition tracer (CO mass fraction) in the cylinder as a function of crank angle starting at injection till ignition (SOI: -7° ATDC)

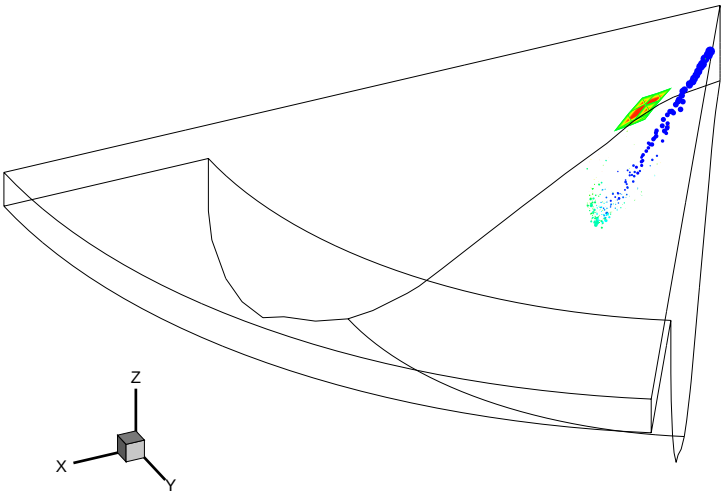

Figure 5.6: Location of the first ignition cell relative to the spray (SOI: -7° ATDC)

fuel-lean regions due to the cooling effect of the fuel. Hence, ignition occurs in the fuel-lean region. In the case shown in Figure 5.6, the first ignition cell corresponds to an equivalence ratio of 0.7 (mixture fraction of 0.043).

These trends were seen in all the cases simulated (all the possible SOI values). Table 5.2 shows the ignition delay times in terms of crank angle (CA) and in real time, and the ignition location in terms of the equivalence ratio (ϕ; $\phi = 1$ indicating a stoichiometric mixture) and the mixture fraction (ξ) for all the SOI timings. All the ignition cells are lean with equivalence ratios less than 1, which is in accordance with results in the literature [123]. The ignition delay time for the case SOI -4° ATDC is lower than that for the case SOI -7° ATDC. This is because injection takes place later in the compression stroke where the temperatures are higher, resulting in faster ignition. This trend is not seen while comparing the case SOI -4° ATDC with the case SOI -1° ATDC, where the ignition delay remains approximately the same. Although injection takes place later in the compression stroke for SOI -1° ATDC, the ignition actually takes place during the expansion stroke during which the temperatures drop. Comparing the case SOI -1° ATDC with the cases SOI +2° ATDC and SOI +5° ATDC,

SOI (° ATDC)	Ignition delay: CA / Time(ms)	Ignition location: ϕ / ξ
-7	3.46° / 0.360	0.69 / 0.043
-4	3.32° / 0.346	0.96 / 0.059
-1	3.32° / 0.346	0.66 / 0.041
+2	3.40° / 0.354	0.66 / 0.041
+5	4.25° / 0.443	0.61 / 0.037

Table 5.2: Ignition timing and location for different SOI timings

it is seen that the later the injection timing in the compression stroke, the larger is the ignition delay due to lower temperatures and pressures.

5.4 Flame propagation

After successfully testing the ignition model, the flame propagation was modeled using a combination of the ignition model and the ILDM chemistry model. Thus, not only was it possible to capture the first ignition cell, but also later ignition. The turbulent chemistry in each cell was described by applying the presumed pdf method to ILDM chemistry (see Section 3.2). Figures 5.7, 5.8 and 5.9 show the development of the flame at a particular slice through the engine at different crank angle locations. This slice was chosen as the major part of the plane does not pass through the spray, which is ideal for demonstrating the propagation of the flame as it contains a maximum equivalence ratio of about 2. A slice through the spray would only contain very rich regions (with equivalence ratios above 2, mixture fractions above 0.12) where the chemistry is not dominant, thereby having low temperatures. The figures are for the case with start of injection +2° ATDC.

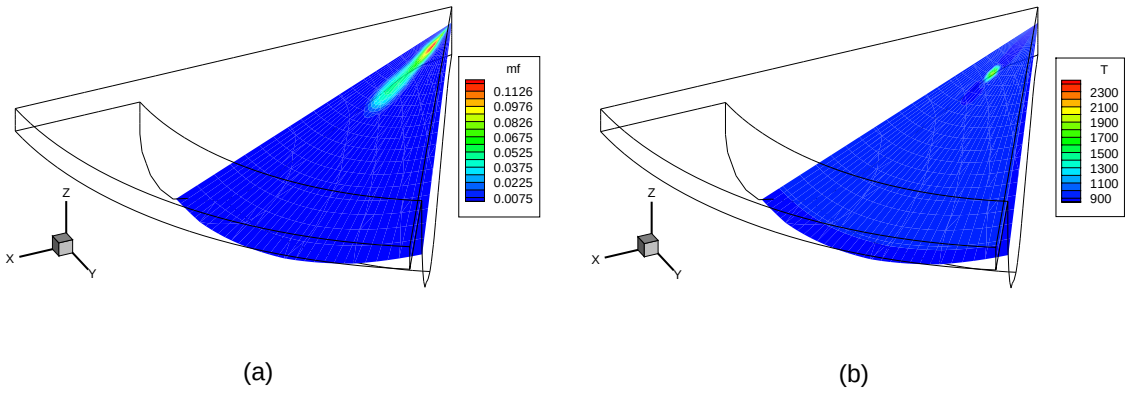

Figure 5.7: Flame propagation at crank angle +5.6° ATDC (SOI: +2° ATDC) a) Mixture fraction b) Temperature (K)

Figure 5.7 is at crank angle +5.6° ATDC (i.e., just after ignition, with ignition occurring at +5.4° ATDC), Figure 5.8 is at crank angle +7° ATDC and Figure 5.9 is at crank angle +10° ATDC. Figure 5.7(a) shows the mixture fraction field while Figure 5.7(b) shows the temperature field. One sees that ignition occurs upstream of the injector at the edge of the spray in the lean region, and the flame has just started to propagate. After about 0.14 ms (at crank angle +7° ATDC), the mixture fraction field shown in Figure 5.8(a) looks more spread out. This is not only because more fuel has been injected, but also because the high temperatures of the flame cause the fuel to evaporate more rapidly. The temperature field shown in Figure 5.8(b) shows the flame propagation clearly. The flame has spread into the lean and rich regions of the engine, with the very rich portion nearer to the injector remaining cold. Highest temperatures are seen in the stoichiometric region, as expected. The advancement of the flame after

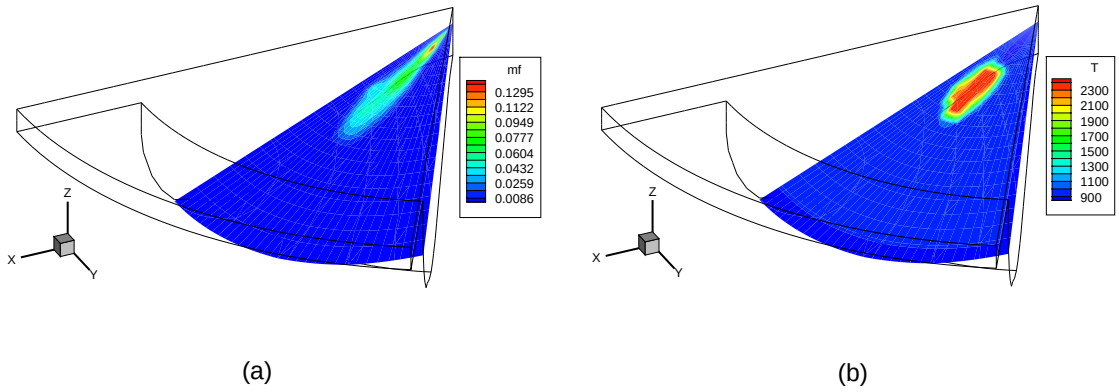

(a) (b)

Figure 5.8: Flame propagation at crank angle +7° ATDC (SOI: +2° ATDC) a) Mixture fraction b) Temperature (K)

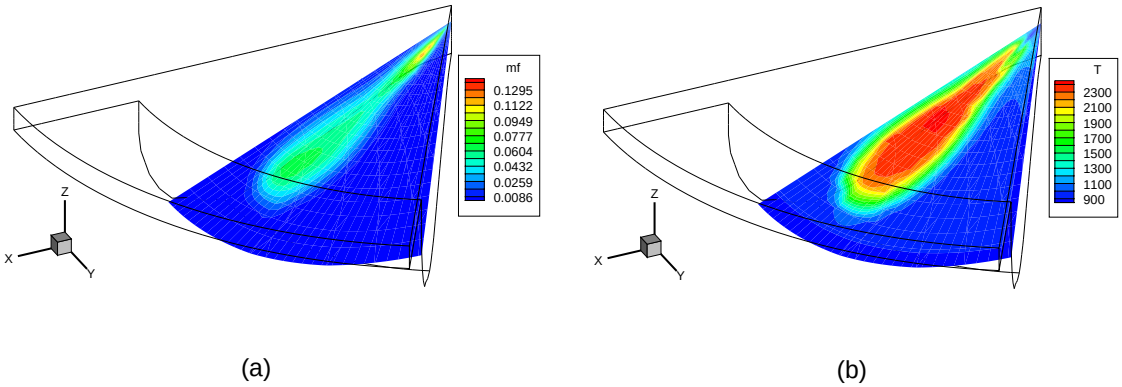

(a) (b)

Figure 5.9: Flame propagation at crank angle +10° ATDC (SOI: +2° ATDC) a) Mixture fraction b) Temperature (K)

a further 0.31 ms (at crank angle +10° ATDC) is shown in Figure 5.9(a) and (b). The fuel concentration field (analogous to the mixture fraction field) and the temperature field have spread considerably. Maximum temperatures of about 2450 K are observed. Since very few rich regions exist at this crank angle on this plane, higher temperatures are seen almost everywhere (except in the sections where no fuel exists indicated by the blue sections in mixture fraction field). Figures similar to the temperature field figures can be created for the species concentrations. The CO_2 concentration field, e.g., looks very similar to the temperature field and is therefore not shown here.

5.5 Pollutant formation

In simulating the engine, not only can be temperature field and the flame propagation be calculated, but the formation of pollutants can also be predicted. NO and soot

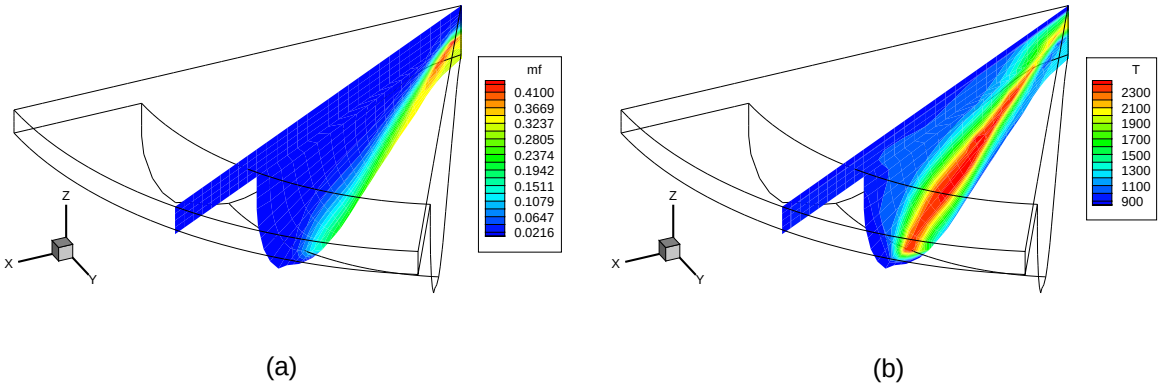

(a) (b)

Figure 5.10: At crank angle +8.5° ATDC (SOI: -1° ATDC) a) Mixture fraction b) Temperature (K)

were identified as the main pollutants. Thermal NO was predicted using the Zeldovich mechanism (see Section 3.3.1) and soot was predicted using a phenomenological model (see Section 3.3.2). In order to examine pollutant formation, a vertical slice through the engine at a particular crank angle 8.5° ATDC was plotted. The case considered is the one with start of injection -1° ATDC. This time, a slice was taken parallel to the spray and thus, much higher mixture fractions are seen here than in the previous figures. Figure 5.10(a) shows the mixture fraction field and Figure 5.10(b) shows the temperature field. The spray core which is very rich remains cold, while the surrounding slightly rich, stoichiometric and lean fluid burns.

The formation of NO is governed by two main factors: the O-atom concentration and the temperature. Thermal NO formation is extremely sensitive to the temperature due to the large activation energy of the rate-controlling reaction. Figure 5.11(a) shows the O-atom concentration field while Figure 5.11(b) shows the NO concentration

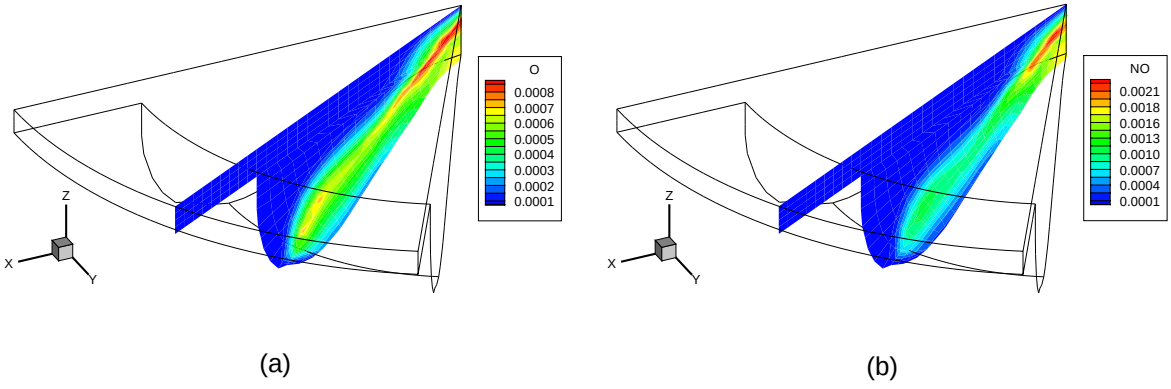

(a) (b)

Figure 5.11: At crank angle +8.5° ATDC (SOI: -1° ATDC) a) O mass fraction b) NO mass fraction

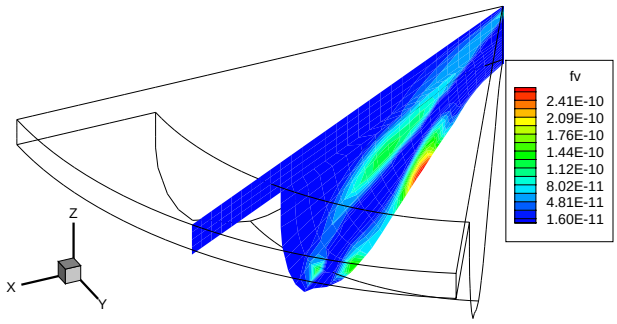

Figure 5.12: Soot volume fraction (f_v) at crank angle +8.5° ATDC (SOI: -1° ATDC)

field for the same slice as in Figure 5.10. It can be seen that the NO is formed wherever the temperature is high. The NO mass fraction is maximum where the O-atom concentration is maximum and where the temperature is high, which is in the near-stoichiometric region [7].

Figure 5.12 shows the soot volume fraction (f_v) field. Soot is formed in the relatively rich regions (where ILDM delivers a result). A gap is observed, above and below of which soot is formed. This can be explained by looking at the temperature field in Figure 5.10(b). The temperatures are relatively high in this gap, leading to soot oxidation. Thus, soot is seen to be dominant in the richer regions where the temperatures are not high enough for oxidation to take place.

Figures 5.13(a) and 5.13(b) show the mean NO concentration (in ppm) and the soot

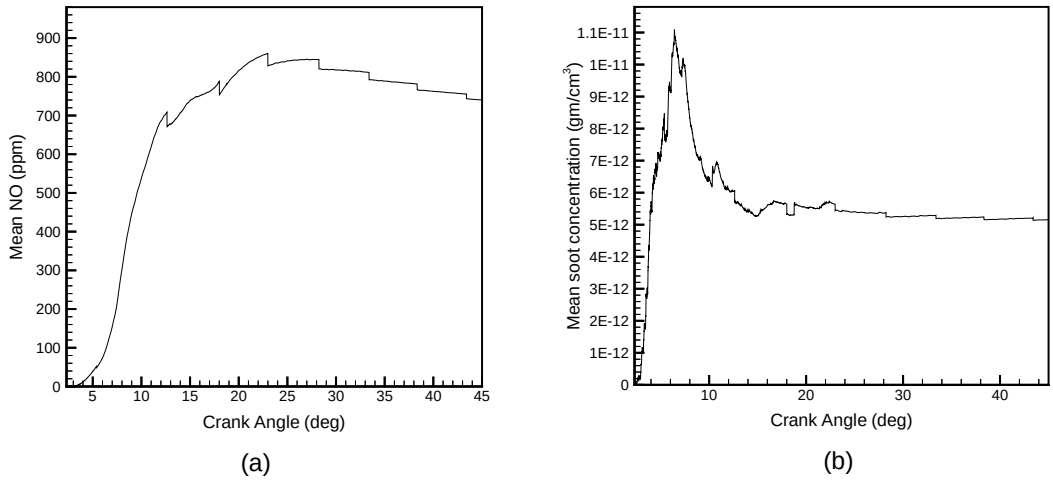

Figure 5.13: Variation of pollutant concentration with crank angle (SOI: -1° ATDC) a) NO concentration (ppm) b) Soot concentration (g/cm^3)

concentration (C_s) in the cylinder as a function of crank angle, starting from ignition, for the same case considered above (SOI: -1° ATDC). The NO concentration rises rapidly immediately after the start of combustion. NO formation rises as the cylinder pressure increases and the combustion proceeds. After the time of the peak pressure, the burned gas temperatures decrease due to expansion. The decreasing temperature due to expansion and due to the mixing of the high-temperature gas with cooler air freezes the NO chemistry and the NO concentration remains relatively constant [7]. The soot concentration, on the other hand, shows a different trend. It rises sharply after combustion and then decreases due to coagulation and oxidation. The spikes in the curves are due to the grid treatment of KIVA. As the cylinder expands, a new plane of cells is re-activated, which are cold with no pollutants. The calculation of the mean amount of pollutants therefore shows a sharp drop, and increases later.

5.6 Comparison with experiments

The ignition model combined with the ILDM model were implemented in KIVA and the combined code was used to simulate the Diesel engine. The following results do not include the radiation model, i.e., the radiative heat losses were assumed to be negligible (which is proven in Section 5.22). Experimental data were available for the mean pressure in the cylinder as a function of the crank angle. Figures 5.14, 5.15 and 5.16 show a comparison between experimental and simulated pressures.

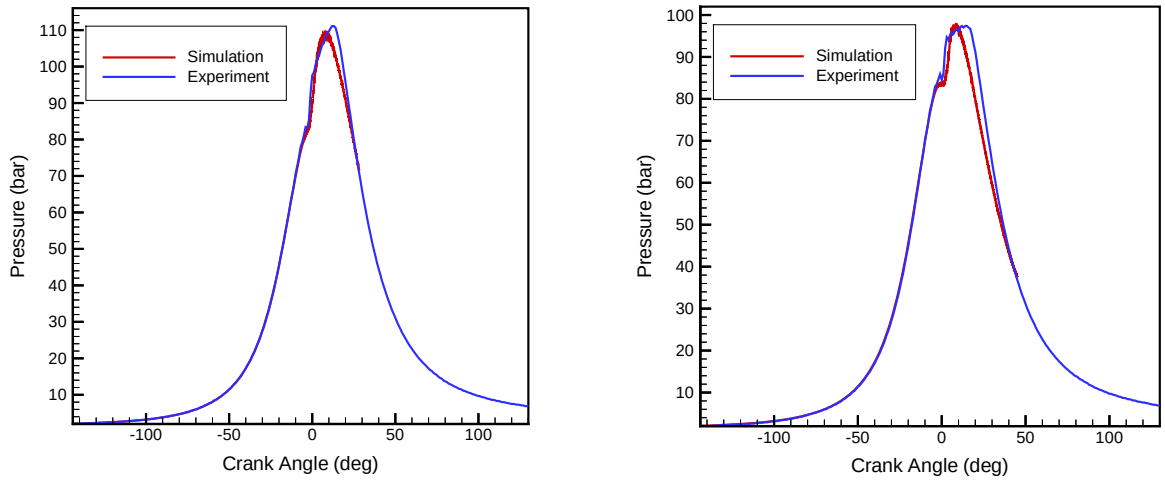

Figure 5.14: Comparison between experimental and simulated pressure curves a) SOI: -7° ATDC b) SOI: -4° ATDC

As can be seen, there is a good agreement between the experimental and simulated results. Starting from BDC, the agreement is nearly perfect, indicating the accuracy of KIVA for Diesel engine simulations. Small deviations are seen, especially nearing

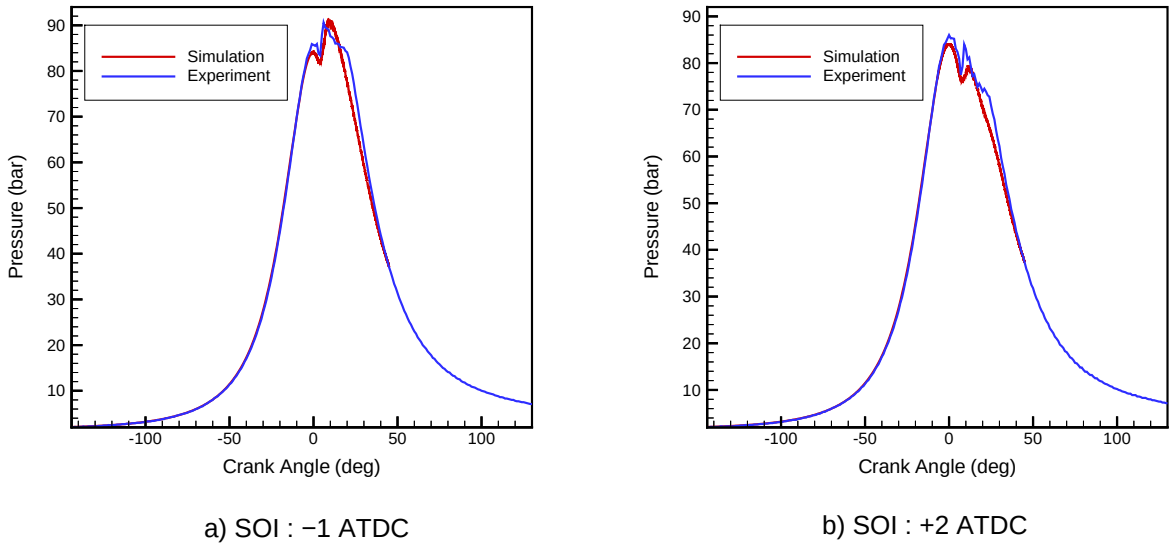

Figure 5.15: Comparison between experimental and simulated pressure curves a)SOI: -4° ATDC b) SOI: +2° ATDC

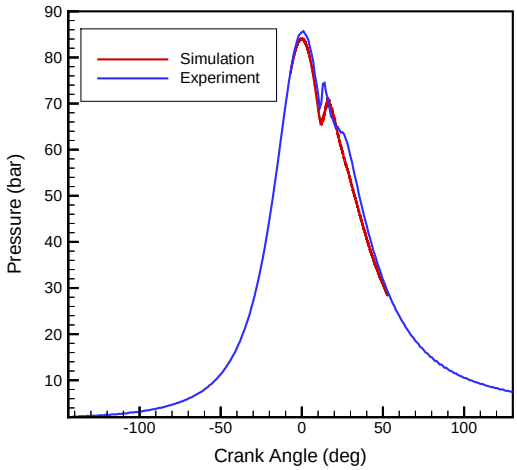

Figure 5.16: Comparison between experimental and simulated pressure curves (SOI: +5° ATDC)

TDC and after injection. This could be due to slight faults in the numerical grid, as well as due to deficiencies in the spray model. The spray model contains certain parameters which need to be specified, which determine the rate of breakup of the spray, etc. These parameters are often changed from case to case in order to match the experimental data. However, in the simulations shown here, all the parameters were maintained constant. Also, the ILDM method has problems as described in Section

3.2.3, and certain assumptions needed to be made to overcome these difficulties. These could also be the cause of the slight deviations seen.

Experimental data is also available for the total amount of pollutants at the end of the cycle. Figure 5.17 shows the mean NO at the end of the cycle as a function of the injection timing and compares it to the experimental data. The later the injection timing is, the lower is the temperature reached. Since the formation of thermal NO is favored at higher temperatures, higher concentrations of NO are observed at earlier injection timings. A good agreement is seen between experiments and simulations, considering the uncertainties in the spray model, etc. A maximum deviation of about 20 % was observed.

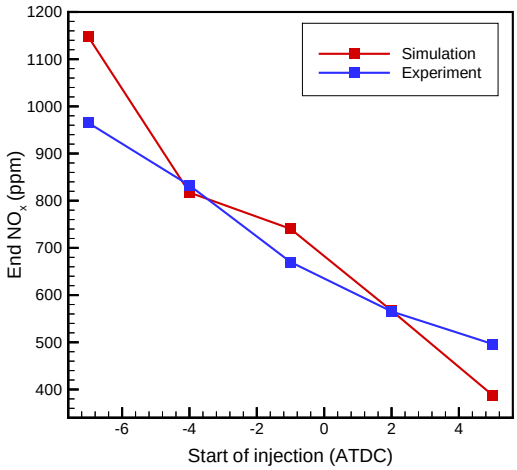

Figure 5.17: The mean end NO_x as a function of injection timing: Comparison between experiments and simulations

Figure 5.18 shows the mean soot at the end of the cycle as a function of the injection timing and compares it to the experimental data. The later the injection timing is, the lower is the temperature reached. Since soot oxidation is dominant at higher temperatures, the dependence of the soot concentration on the injection timing is exactly opposite of that shown by the NO concentration. Thus, later injection timings show more soot due to the lower temperatures reached which do not favor oxidation.

As can be seen from Figure 5.18, soot concentrations are highly under-predicted. Soot modeling usually under-predicts soot concentration as some soot is formed by the lubricating oil [7], which cannot be predicted by such models. However, this contribution is only a small percentage of the total soot concentration. The main reason for the discrepancy seen is the chemistry model used. As described in Section 3.2.3, the ILDM method has numerical problems in the rich region, where soot formation dominates. Thus, only equivalence ratios up to 1.6 (mixture fraction 0.1) could be described by ILDM. This range is sufficient to predict the heat release and the NO precursors, explaining the good agreement between the experimental and simulated pressure curves and the NO concentrations. However, the formation of soot precursors, i.e., C_3H_3 and

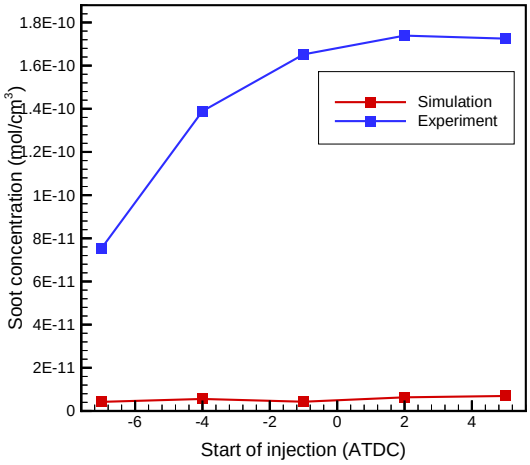

Figure 5.18: The mean end soot as a function of injection timing: Comparison between experiments and simulations

C_2H_2, as predicted by the detailed chemical mechanism used, is negligible in the stoichiometric and lean regions and begins at equivalence ratios of 1.3 (mixture fraction 0.08). Their formation is also confined to lower temperatures (lower than 2000 K), as they are oxidized at higher temperatures. ILDM fails in precisely these regions (see Figure 3.7(b)), explaining the under-prediction of soot in the engine.

5.7 Radiation results

The above results presented were assuming the absence of radiative heat losses, i.e., the radiation model was not used. Before using the radiation model directly in the Diesel engine, the accuracy of this model was tested in a simplified geometry. After testing it, a simpler version of the radiation model was used in the engine to test if the assumption of no radiation heat losses is justified.

5.7.1 Radiation in a simplified geometry

In order to evaluate the numerical method (the discrete ordinates method), it needs to be tested in a case, where there are no uncertainties concerning the fluid properties (such as temperature and concentrations) and the radiative properties (such as wall emissivities, fluid absorption coefficients, etc.). The exact solution of the RTE is a formidable task, and is usually possible only in simple 2-dimensional geometries [113]. These usually have a uniform temperature and concentration field with black walls. However, an accurate test for the radiation model would be to test it in a 3-dimensional geometry and under conditions typical of combustion devices. Typical combustion chambers show non-homogeneous temperature fields with walls which are at different temperatures. This is also the case in the engine simulated, where strong temperature

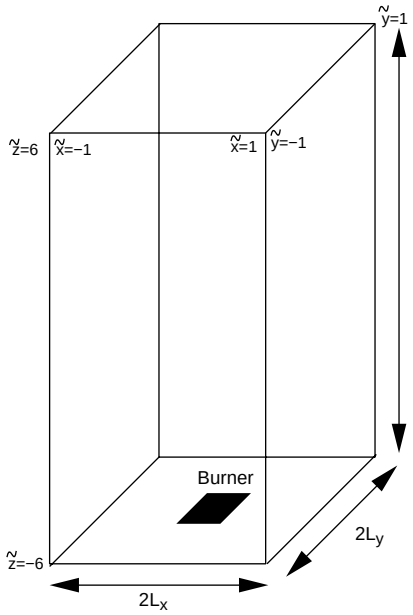

Figure 5.19: Schematic representation of the furnace used for radiation study

gradients exist after ignition, and where the piston and cylinder walls are at different temperatures (see Table 5.1). The equations should, however, be simple enough to be amenable to an analytical solution. A perfect test for the radiation model was found in the literature [115,124]. Here, a 3-dimensional geometry is defined with known medium properties and an analytical solution to the RTE is described.

The physical situation to be considered is that of a rectangular furnace which is fired from the center of the bottom wall and operates at atmospheric pressure. The four side walls are water-cooled and the burner and back end walls are refractory. The furnace is filled with an absorbing-emitting, radiatively grey medium whose absorption coefficient is the same at all points, and of known magnitude. Values of the black-body emissive power are assumed to be available at all points within the enclosed medium, and at all points on the walls. All walls are assumed to be black. A schematic representation of the furnace is shown in Figure 5.19. The origin is taken to be in the center of the furnace, and the walls have lengths $2L_x$, $2L_y$ and $2L_z$ respectively. One can define a reference length (L_0), in order to have dimensionless lengths ($\tilde{x}$, $\tilde{y}$ and $\tilde{z}$),

$$\tilde{x} = x/L_0 \quad , \quad \tilde{y} = y/L_0 \quad \text{and} \quad \tilde{z} = z/L_0 \ . \tag{5.1}$$

First, the temperature distribution in the furnace needs to be defined. As the burner is fired along the z axis, the variation of gas temperatures about this axis is symmetrical. The peak temperature occurs on the axis of symmetry along which the burner is fired. This maximum temperature is chosen as the reference temperature value (T_0), thus producing maximum dimensionless temperature, black-body emissive power (E_0) and intensity (I_0) in the enclosure. These can be used to define a dimensionless temperature

($\tilde{T}$) and intensity ($\tilde{I}$) using

$$\tilde{T} = T/T_0 \quad \text{and} \quad \tilde{I} = I/I_0 \ . \tag{5.2}$$

Axially, the temperature shows an increase from the burner wall, and then decreases to the exit gas temperature T_e. Radially, the temperature is maximum at the axis and decreases towards the walls. This distribution is achieved using the representation

$$\tilde{T}_{\rm G}(x,y,z) = [a(z') - \tilde{T}_{\rm e}]f(r/R) + \tilde{T}_{\rm e} \ . \tag{5.3}$$

All the quantities with a tilde indicate dimensionless quantities. Here, $\tilde{T}_{\rm G}$ is the dimensionless medium temperature. $f(r/R)$ is a functional form employed for the representation of gas temperature in the circular region ($R = L_x = L_y$) normal to the sides of the furnace. Outside the circular region, the dimensionless gas temperature is assumed to be equal to the dimensionless exit temperature $\tilde{T}_{\rm e}$. z' is a dimensionless distance ($z' = z/L_z$) and $a(z')$ is a function accounting for the axial variation of the temperature. In order to describe the radial distribution of temperature, the used functional form for $f(r/R)$ is [124]

$$f(r/R) = 1 - 3(r/R)^2 + 2(r/R)^3 \ , \tag{5.4}$$

which expresses the fact that the temperature is maximum at the axis ($r = 0$, $f(r/R) = 1$) and falls to the exit temperature at the walls ($r = R$, $f(r/R) = 0$). The axial variation of temperature can be described by using the following functional form for a(z') [124]:

$$\begin{aligned} a(z') &= 1 + (1 - \tilde{T}_{\rm i})(\frac{z' + z'_{\rm max}}{1 - z'_{\rm max}})^3 \quad \text{for} \quad -1 \le z' \le z'_{\rm max} \\ &= 1 - [d_{\rm e}(1 + z'_{\rm max}) + 3(1 - \tilde{T}_{\rm e})](\frac{z' + z'_{\rm max}}{1 + z'_{\rm max}})^2 \\ &\quad + [d_{\rm e}(1 + z'_{\rm max}) + 2(1 - \tilde{T}_{\rm e})](\frac{z' + z'_{\rm max}}{1 + z'_{\rm max}})^3 \quad \text{for} \quad -z'_{\rm max} \le z' \le 1 \ , \end{aligned} \tag{5.5}$$

where $\tilde{T}_{\rm i}$ is the dimensionless inlet temperature, $d_{\rm e}$ is the slope of the axial temperature curve at the exit and $z'_{\rm max}$ is the location of the maximum on the z axis. The above equation indicates that the temperature along the axis increases from the inlet temperature to its maximum located at $z'_{\rm max}$, and then decreases to the exit temperature. The actual data used for the temperature distribution as well as the absorption coefficient used, etc. is listed in Table 5.3.

Dimensions of the furnace	$\tilde{L}_x = 1$, $\tilde{L}_y = 1$, $\tilde{L}_z = 6$
Optical thickness	$\tau_0 = 1/6$
Wall black-body intensities	$(\tilde{I}_{\mathrm{bw}})_{\mathrm{side}} = 0.0020$ $(\tilde{I}_{\mathrm{bw}})_{\mathrm{burner}} = 0.0574$ $(\tilde{I}_{\mathrm{bw}})_{\mathrm{end}} = 0.0167$
Gas temperatures	$\tilde{T}_{\mathrm{i}} = 0.1775$ $\tilde{T}_{\mathrm{e}} = 0.6222$ $\tilde{T}_{\mathrm{max}} = 1$
Position of the peak	$z'_{\mathrm{max}} = 0.8$
Slope of gas temperature at exit	$d_{\mathrm{e}} = -0.220$

Reference values used to make the data dimensionless:
$L_0 = 0.48$ m, $T_0 = 1673$ K, $I_0 = 1.4139 \times 10^5$ Wm^{-2}sr^{-1}

Table 5.3: Dimensionless data for furnace specifications [124]

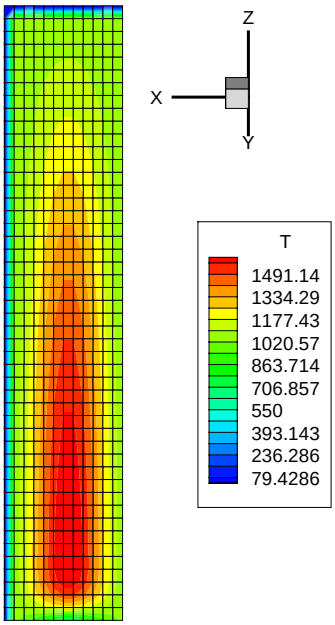

Figure 5.20: Temperature distribution in a slice through the center of the furnace

The obtained temperature distribution is shown in Figure 5.20 along with the grid used. The furnace was approximated using a $12 \times 12 \times 48$ grid. The dimensionless flux density can be solved for analytically and its values at particular locations in the furnace are available [124]. These are reported for the side wall ($\tilde{x} = 1$), at two

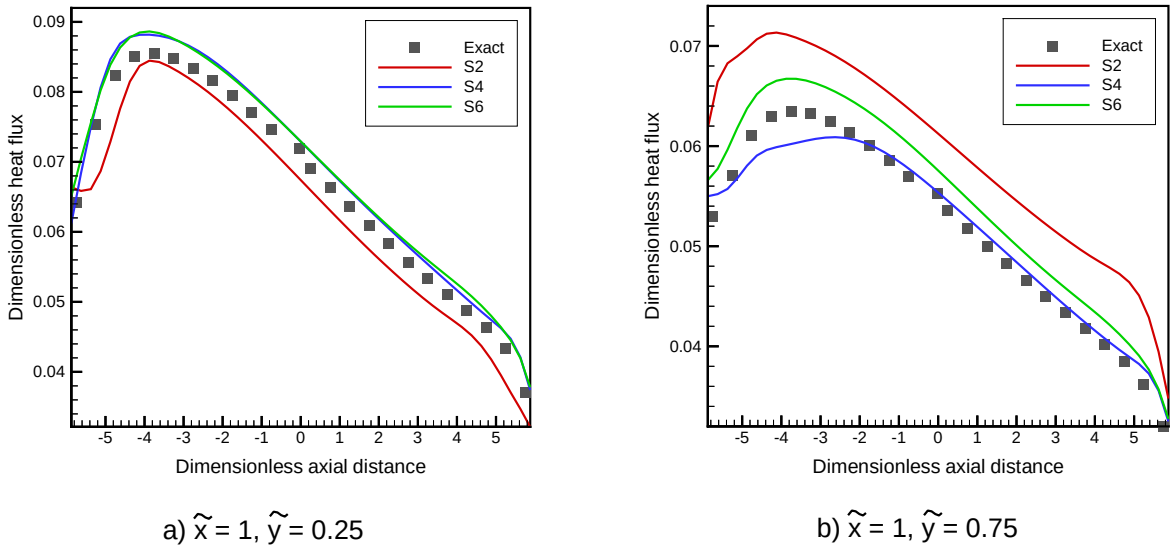

Figure 5.21: Comparison between the exact and simulated dimensionless flux a) $\tilde{x} = 1$, $\tilde{y} = 0.25$ b) $\tilde{x} = 1$, $\tilde{y} = 0.75$

particular y locations ($\tilde{y} = 0.25$ and $\tilde{y} = 0.75$) as a function of the axial furnace length ($\tilde{z}$), i.e. $q_r(1, 0.25, \tilde{z})$ and $q_r(1, 0.75, \tilde{z})$ is reported.

The radiative intensity distribution in the furnace was also solved for using the discrete ordinates method described in Section 3.4.2. Three different methods were used: S2, S4 and S6. The three methods differ in the number of directions used to approximate the 4π solid angle. The S2 method involves 8 directions, the S4 involves 24 directions and the S6 involves 48 directions. Increasing the number of directions is expected to increase the accuracy of the discrete representation of the angular dependence of the intensity.

Figure 5.21 shows the comparison between the exact solutions and the simulations using S2, S4 and S6. The dimensionless wall heat flux is plotted as a function of the dimensionless axial distance. As can be seen, the flux increases from the burner wall ($\tilde{z} = -6$) to a maximum and then decreases towards the exit. This is the same behavior shown by the gas temperature as shown in Figure 5.20. Thus, the maximum of the radiative heat flux corresponds to the maximum of the gas temperature. The fluxes at $\tilde{y} = 0.25$ are higher than those at $\tilde{y} = 0.75$, as the gas temperature is maximum at along the furnace axis and decreases towards the walls. The plane $\tilde{y} = 0.25$ lies closer to the axis $\tilde{y} = 0$ than $\tilde{y} = 0.75$, and thus has higher temperatures. A good agreement is seen between the discrete ordinates method and the exact solutions, especially for the higher order methods. The S2 method shows significant discrepancies due to the relatively coarse discretization of the solid angle. The agreement is much better with S4 and S6, indicating that these methods are accurate enough to be used in engine calculations. However, further refinement of the solid angle was not attempted (for e.g. S8 or S10), as the increase in the number of directions drastically increases the computational time.

Also, further refinement in angular quadrature may not necessarily yield more accurate results unless accompanied by a corresponding refinement in spatial discretization [114, 119]. The slight deviations between the numerical results and the exact solutions occur due to "ray effects" [113]. The ray effect is an outcome of the discrete ordinates method arising from the finite discretization of the angular divergence operator in the radiative transfer equation. Thus, the DOM replaces a continuously varying differential operator by a discrete and finite set of equations. Radiation is allowed to stream only along these directions. Thus, radiation from an isolated source may be unseen by a point, unless the point and the source lie along an ordinate direction. However, as seen from Figure 5.21, increasing the number of directions reduces these effects, leading to accurate results with the S4 and the S6 method.

5.7.2 Radiation in the engine

In the previous section, it was shown that the discrete ordinates method is an accurate solution method for the radiative transfer equation. The importance of the radiative mode of heat transfer in an engine depends on the temperatures attained and the concentrations of the radiating species. Radiation is considered to be negligible in spark-ignition engines [80] due to the very small amounts of soot formed, and because gas radiation is not significant enough to make radiation an important mode of heat transfer. In Diesel engines, this situation may change due to the presence of soot. However, as seen in Section 5.5, the soot concentrations are highly under-predicted. Thus, the assumption that radiative losses can be neglected, may be justified in these simulations. Also, although the discrete ordinates method is computationally not as expensive as other RTE solution methods, its use in an engine simulation may not be justified, where the RTE needs to be solved at every time step in the cycle.

In order to test the importance of radiative transfer in the Caterpillar engine, one case was chosen where the soot concentrations are sufficiently high (soot concentrations are higher at later SOI timings), but the temperatures reached are also sufficiently high (temperatures are higher at earlier SOI timings). The case of SOI -1° ATDC was chosen. The accuracy of the discrete ordinates method was already tested in Section 5.7.1, and here only the importance of the radiative heat transfer mode was tested. In order to test that, the complete RTE does not need to be solved. As described in Section 3.4, when the medium is optically thin, the RTE does not need to be solved, and the source term for the energy equation is

$$\operatorname{div} \vec{F} = \int_0^\infty 4\pi k_{\mathrm{a},\lambda} I_{\mathrm{b},\lambda} \mathrm{d}\lambda \ . \tag{5.6}$$

The absorption coefficients $k_{\mathrm{a},\lambda}$ and the black-body intensities $I_{\mathrm{b},\lambda}$ are only functions of the local temperatures and radiative species concentrations. The wavelength dependence was treated with the WSGGM (see Section 3.4.1), where the entire spectrum was divided into bands. The absorption coefficient was then predicted in these bands

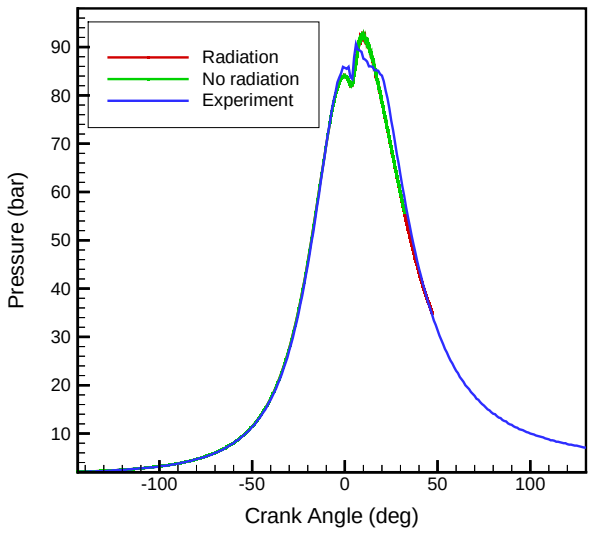

Figure 5.22: Cylinder pressure in the engine with and without radiation (SOI: -1° ATDC)

while the total black-body intensity was weighted to obtain the black-body intensity in each band. The above source term was integrated over a pdf in order to allow its use in turbulent flows. The assumption of an optically thin medium over-predicts the radiative heat losses as the medium is only assumed to emit radiation, without re-absorbing [84]. This approach was used to simulate an engine cycle, as this would be a true test of the importance of radiation in the engine.

Figure 5.22 shows a comparison between the pressure curves assuming no radiative heat losses and using the optically-thin radiation model. One sees no discernible differences in the pressures (and hence in the temperatures). The pollutant concentrations also remained practically unchanged. Radiative heat losses did not exceed 1% of the total energy. The assumption of low optical thickness is probably justified in the engine, as the absorption coefficients are small (due to the low concentrations of soot predicted) and due to the small characteristic length of an engine cylinder, especially compressed. An exact check of the optical thickness is difficult due to the absence of exact definitions for the mean beam length L_e (see Equation 3.54). Thus, it is safe to conclude that radiative heat losses are negligible in the Caterpillar engine, especially with the low quantities of soot predicted.

6 Conclusions and recommendations

The aim of this dissertation was to develop and implement new models in an existing three-dimensional simulation code, suitable for Diesel engine simulations. Three areas were identified, where existing simulations could be improved: the ignition model, the chemistry model and the radiation heat transfer model. In the ignition model, a model based on a detailed chemical mechanism was used, but which is based on a single representative species which is traced to predict the location and the timing of ignition. For flame propagation, the intrinsic low-dimensional manifold method (ILDM) was used as a chemistry model, which is a dynamic local reduction of a detailed chemical mechanism based on an time scale (eigenvalue) analysis. The radiation model used involves a discrete ordinates method for the solution of the radiative transfer equation and a weighted sum of grey gases model to treat the wavelength dependence of the radiative intensity. The discrete ordinates method is based on the discretization of the solid angle into discrete directions, which enables its incorporation into control-volume based CFD codes. In addition to the above models, a probability density function (pdf) method was used in order to account for turbulence effects.

In order to test the above models, they were used to simulate a Caterpillar Diesel engine, for which experimental pressure curves and the concentration of pollutants at the end of the cycle are available. A one-dimensional manifold was used with n-heptane as the model fuel for Diesel. The ignition results show that ignition takes place in lean-to-stoichiometric region at the edge of the spray, slightly downstream from the injector. The use of the ignition model along with the ILDM chemistry model showed that the pressure curves are well predicted over a range of injection timings. Pollutant prediction for NO (using the Zeldovich mechanism) and soot (using a phenomenological model) were done. NO formation occurs mainly in the high temperature, close to stoichiometric region. Soot formation occurs in the rich, low temperature region where oxidation does not occur. The mean NO and soot concentrations at the end of the cycle were compared to experiments. NO predictions were satisfactory, however soot was highly underpredicted. This can be attributed to the numerical problems ILDM experiences in the rich regions where the formation of soot precursors is important. The discrete ordinates method was tested in a furnace with strong temperature gradients and a known temperature and radiative property field, and for which an analytical solution was available. Good agreement was seen between the exact and the simulated radiative fluxes at the wall, especially when the number of discrete directions was increased. In order to test the importance of radiation in the engine, the weighted sum of grey gases model was used along with the assumption of optically thin medium, which overpredicts the radiative heat loss. Due to the low concentrations of soot predicted, radiative losses were found to be negligible. The pollutant concentrations were not affected by these losses.

Several improvements can be made to the above models in order to improve the results. The most valuable improvement would be in the numerical methods used to solve the ILDM equations. Due to numerical problems, especially in the rich region, a 1-dimensional manifold could not be identified in several points in the state space. Since

an ILDM could mostly be identified in the stoichiometric, slightly lean and slightly rich regions, the flame propagation could be sufficiently reproduced (as indicated by the pressure curves). However, the formation of soot precursors, which is dominant in the rich region, could not be predicted, leading to an underprediction of soot in the Diesel engine. Also, the failure of ILDM at lower temperatures necessitated the use of a simpler model (1-step chemistry) as a bridge between ignition and ILDM. The pdf used could also be improved. The splitting of the three-dimensional pdf into three one-dimensional pdfs is not valid, if the variables are not statistically independent. The sensitivity of the results to this assumption should be examined.

References

[1] Warnatz J., *Eighteenth Symposium (Intl.) on Combustion*, The Combustion Institute, Pittsburgh, pp 369 (1981).

[2] Warnatz J., *Twenty-fourth Symposium (Intl.) on Combustion*, The Combustion Institute, Pittsburgh, pp 553 (1992).

[3] Smooke, M. D., Mitchell, R. E. and Keyes, D. E., *Combust. Sci. Technol.*,**67**, 85 (1989).

[4] Saxena V. and Pope, S. B., *Twenty-Seventh Symposium (Intl.) on Combustion*, The Combustion Institute, Pittsburgh, pp 1081 (1999).

[5] Piquet, J., *Turbulent Flows*, Springer (1999).

[6] Amsden, A. A., O'Rourke, P. J. and Butler, T. D., *KIVA-II: A Computer Program for Chemical Reactive Flows with Sprays*, Los Alamos National Laboratory Report LA-11560-MS (1989).

[7] Heywood, J. B., *Internal Combustion Engine Fundamentals*, McGraw Hill (1988).

[8] Dixon-Lewis, G., Fukutani, S., Miller, J. A., Peters, N., Warnatz, J. et al., *Twentieth Symposium (Intl.) on Combustion*, The Combustion Institute, Pittsburgh, pp 1893 (1984).

[9] Maas, U. and Pope, S. B., *Combustion and Flame*, **88**, 239 (1992).

[10] Maas, U. and Pope, S. B., *Twenty-Fourth Symposium (Intl.) on Combustion*, The Combustion Institute, Pittsburgh, pp 103 (1992).

[11] Borghi, R., Argueyrolles, B., Gauffie, S. and Souhaite, P., *Twenty-First Symposium (Intl.) on Combustion*, The Combustion Institute, Pittsburgh, pp 1591 (1986).

[12] Siegel, R. and Howell, J. R., *Thermal Radiation Heat Transfer*, Hemisphere Publishing Corporation (1992).

[13] Chandrasekhar, S., *Radiative Transfer*, Dover (1960).

[14] Choi, E. C. and Baek, S. W., *Combust. Sci. Technol.*, **115**, 297 (1996).

[15] Bird, R. B., Stewart, W. E. and Lightfoot, E. N., *Transport Phenomena*, John Wiley and Sons (1960).

[16] Williams, F. A., *Combustion Theory*, Addison-Wesley (1985).

[17] Stull, D. R. and Prophet, H., *JANAF Thermochemical Tables*, U.S. Department of Commerce/National Bureau of Standards, NSRDS-NBS37 (1971).

[18] Gill, A., *Modellierung der Verbrennung in einem Schlichtlade-Motor unter Verwendung detaillierter chemischer Reaktionsmechanismen*, Dissertation, ITV, Universität Stuttgart (1995).

[19] Libby, P. A. and Williams, F. A., *Turbulent Reacting Flows*, Springer (1980).

[20] Launder, B. E. and Spalding, D. B., *Mathematical Models of turbulence*, Academic Press (1972).

[21] Prandtl, L., *Zeitschrift für Angewandte Mathematik und Mechanik*, **5**, 136 (1925).

[22] Launder, B. E., Reece, G. J. and Rodi, W., *J. Fluid Mech*, **68**, 537 (1975).

[23] Görner, K., *Technische Verbrennungssysteme*, Springer (1991).

[24] Jones, W. P. and Launder, B. E., *Int. J. Heat Mass Transfer*, **15**, 301 (1972).

[25] Hämmerle, T. G., *Vergleich statistischer Modelle mit PDFs bei der Simulation turbulenter Methan-Luft-Flammen*, Diplomarbeit, Universität Heidelberg (1997).

[26] El Tahry, S. H., *A Comparison of Three Turbulence Models in Engine-like Geometries*, COMODIA **85**, 203, Tokyo (1985).

[27] Amsden, A. A., Butler, T. D., O'Rourke, P. J. and Ramshaw, J. D., *SAE Technical Paper* 850554 (1985).

[28] Bracco, F. V., *SAE Technical Paper* 850394 (1985).

[29] O'Rourke, P. J., *Collective Drop Effects in Vaporizing Liquid Sprays*, Ph.D. Thesis, Princeton University (1981).

[30] Reitz, R. D., *Atomisation and Spray Technology*, **3**, 309 (1987).

[31] Reitz, R. D. and Diwakar, R., *SAE Technical Paper* 870598 (1987).

[32] Xin, J., Ricart, L. and Reitz, R. D., *Comb. Sci. Technol.*, **137**, 171 (1998).

[33] Pinchon, P., *Modeling of Fluid Dynamics and Combustion in Piston Engines*, Int. Symposium COMODIA, **90**, 31 (1990).

[34] Kamimoto, K. and Kobayashi, H., *Prog. Energy Comb. Sci.*, **17**, 163 (1991).

[35] Gosman, A. D. and Harvey, P. S., *SAE Technical Paper* 820036 (1982).

[36] Warnatz, J., *Joint Meeting of the British and German Sections of the Combustion Institute*, The Combustion Institute (1993).

[37] Westbrook, C. K. and Dryer, F. L., *Combust. Sci. Technol.*, **27**, 31 (1981).

[38] Warnatz, J., Maas, U. and Dibble, R. W., *Combustion*, 2nd Edition (1999).

[39] Borghi, R., *Prog. Energy Combust. Sci.*, **14**, 145 (1988).

[40] Vulis, L. A., *Explosion, Combustion and Shock Waves* (Russian issue), **8** (1972).

[41] Pope, S. B., *Prog. Energy Combust. Sci.*, **11**, 119 (1985).

[42] Pope, S. B., *Twenty-Third Symposium (Intl.) on Combustion*, The Combustion Institute, Pittsburgh, pp 591 (1990).

[43] Pope, S. B., *Eighteenth Symposium (Intl.) on Combustion*, The Combustion Institute, Pittsburgh, pp 1001 (1981).

[44] Jones, W. P. and Kakhi, M., *Unsteady Combustion*, pp 411 (1996).

[45] Girimaji, S. S., *Combust. Sci. Technol.*, **78**, 177 (1991).

[46] Lockwood, F. C. and Naguib, A. S., *Combust. Flame*, **24**, 109 (1975).

[47] Janicka, J. and Kollman, W., *Seventeenth Symposium (Intl.) on Combustion*, The Combustion Institute, Pittsburgh, pp 421 (1979).

[48] Khalil, E. E., Spalding, D. B. and Whitelaw, J. H., *Int. J. Heat Mass Transfer*, **18**, 775 (1975).

[49] Elsden, M. R., Gutheil, E., Nehse, M. and Warnatz, J. *Internal Combustion Engines (ICE)*, Naples, Italy (1997).

[50] Vranos, A., *Combust. Sci. Technol.*, **84**, 323 (1992).

[51] Soong, H. C. and Chang, K. C., *Int. J. Turbo Jet Engines*, **9**, 227 (1992).

[52] Gutheil, E., *Modellierung turbulenter Kohlenstoffmonoxid/Luft Diffusionsflammen*, Dissertation, TH Darmstadt (1988).

[53] Eswaran, V. and Pope, S. B., *Physics of Fluids*, **31(3)**, 506 (1988).

[54] Gutheil, E., *Personal Communication*, Universität Heidelberg (1998).

[55] Smooke, M. D., Ed., *Reduced Kinetic Mechanisms and Asymptotic Approximations for Methane-Air Flames*, Lecture notes in Physics, **384**, Springer (1991).

[56] Maas, U., *Automatische Reduktion von Reaktionsmechanismen zur Simulation reaktiver Strömungen*, Habilitationsschrift, Universität Stuttgart (1993).

[57] Rawat, R., *Modeling Finite-Rate Chemistry in Turbulent Reacting Flows*, Dissertation, The University of Utah (1997).

[58] Lam, S. H. and Goussis, D. A., *Twenty-second Symposium (Intl.) on Combustion*, The Combustion Institute, Pittsburgh, pp 931 (1988).

[59] Niemann, H., *Dissertation in preparation*, Universität Heidelberg (2000).

[60] Schmidt, D., *Modellierung reaktiver Strömungen unter Verwendung automatisch reduzierter Reaktionsmechanismen*, Dissertation, Universität Heidelberg (1996).

[61] Correa, C., Niemann, H., Schramm, B. and Warnatz, J., *Twenty-eighth Symposium (Intl.) on Combustion (accepted)*, The Combustion Institute, Pittsburgh (2000).

[62] Bowman, C. T., *Twenty-fourth Symposium (Intl.) on Combustion*, The Combustion Institute, Pittsburgh, pp 859 (1992).

[63] *Soot Formation in Combustion: Mechanisms and Models*, Springer (1994).

[64] *Prog. Energy Combust. Sci.*, **23**, 95 (1997).

[65] Khan, I. M. and Greeves, G., *Heat Transfer in Flames*, Afgan, A. H. and Beer, J. M., Eds., Scripta (1974).

[66] Yoshihara, Y., Kazakov, A., Wang, H. and Frenklach, M., *Twenty-fifth Symposium (Intl.) on Combustion*, The Combustion Institute, Pittsburgh, pp 941 (1994).

[67] Pitsch, H., Wan, Y. P. and Peters, N., *SAE Technical Paper* 952357 (1995).

[68] Pitsch, H., Barths, H. and Peters, N., *SAE Technical Paper* 962057 (1996).

[69] Stein, S. E., Walker, J. A., Suryan, M. M. and Fahr, A., *Twenty-third Symposium (Intl.) on Combustion*, The Combustion Institute, Pittsburgh, pp 85 (1990).

[70] Moss, J. B., Stewart, C. D. and Syed, K. J., *Twenty-second Symposium (Intl.) on Combustion*, The Combustion Institute, Pittsburgh, pp 413 (1988).

[71] Syed, K. J., Stewart, C. D. and Moss, J. B., *Twenty-third Symposium (Intl.) on Combustion*, The Combustion Institute, Pittsburgh, pp 1533 (1990).

[72] Young, K. J. and Moss, J. B., *Combust. Sci. Technol.*, **105**, 33 (1995).

[73] Stewart, C. D., Syed, K. J. and Moss, J. B., *Combust. Sci. Technol.*, **75**, 211 (1991).

[74] Moss, J. B., Stewart, C. D. and Young, K. J., *Combust. Flame*, **101**, 491 (1995).

[75] Bressloff, N. W., Moss, J. B. and Rubini, P. A., *Twenty-sixth Symposium (Intl.) on Combustion*, The Combustion Institute, Pittsburgh, pp 2379 (1996).

[76] Kellerer, H., Müller A., Bauer, H.-J. and Wittig, S., *Combust. Sci. Technol.*, **114**, 67 (1996).

[77] Sojka, J., *Dissertation in preparation*, Universität Heidelberg (2000).

[78] Haynes, B. S. and Wagner, H. G., *Prog. Energy Combust. Sci.*, **7**, 229 (1981).

[79] Jander, H., *Personal Communication*, Universität Göttingen (1999).

[80] Borman, G. and Nishiwaki, K., *Prog. Energy Combust. Sci.*, **13**, 1 (1987).

[81] Viskanta, R. and Mengüç, M. P., *Prog. Energy Combust. Sci.*, **13**, 97 (1987).

[82] Kerker, M., *The Scattering of Light and Other Electromagnetic Radiation*, Academic Press (1969).

[83] De Ris, J., *Seventeenth Symposium (Intl.) on Combustion*, The Combustion Institute, Pittsburgh, pp 1003 (1978).

[84] Marracino, B. and Lentini, D., *Combust. Sci. Technol.*, **128**, 23 (1997).

[85] Tien, C. L. and Lee, S. C., *Prog. Energy Combust. Sci.*, **8**, 41 (1982).

[86] Adams, B. R. and Smith, P. J., *Combust. Sci. Technol.*, **109**, 121 (1995).

[87] Mengüç, M. P. and Viskanta, R., *Combust. Sci. Technol.*, **51**, 51 (1987).

[88] Boyd, R. K. and Kent, J. H., *Twenty-first Symposium (Intl.) on Combustion*, The Combustion Institute, Pittsburgh, pp 265 (1986).

[89] Sivathanu, Y. R., Kounalakis, M. E. and Faeth, G. M., *Twenty-third Symposium (Intl.) on Combustion*, The Combustion Institute, Pittsburgh, pp 1543 (1990).

[90] Song, T. H. and Viskanta, R., *J. Thermophysics and Heat Transfer*, **1**, 56 (1987).

[91] Ludwig, C. B., Malkmus, W., Reardon, J. G. and Thomson, J. A., *Handbook of Infrared Radiation from Combustion Gases*, R. Goulard and J. A. L. Thomson (Eds.), NASA SP-3080, Washington D. C. (1973).

[92] Kim, T. K., Menart, J. A. and Lee, H. S., *J. Heat Transfer*, **115**, 184 (1991).

[93] Zhang, L., Soufiani, A. and Taine, J., *Int. J. Heat Mass Transfer*, **31**, 2261 (1988).

[94] Lallemant, N., Sayre, A. and Weber, R., *Prog. Energy Combust. Sci.*, **22**, 543 (1996).

[95] Song, T. H. and Viskanta, R., *ASME Paper* 86-WA/HT-36 (1986).

[96] Edwards, D. K., *Advances in Heat Transfer*, T. F. Irvine and J. P. Harnett (Eds.), Vol. 12, Academic Press (1976).

[97] Leckner, B., *Combust. Flame*, **19**, 33 (1972).

[98] Hottel, H. C. and Sarofim, A. F., *Radiative Transfer*, McGraw-Hill (1967).

[99] Modest, M. F., *J. Heat Transfer*, **113**, 650 (1991).

[100] Taylor, P. B. and Foster, P. J., *Int. J. Heat Mass Transfer*, **17**, 1591 (1974).

[101] Smith, T. F., Shen, Z. F. and Friedman, J. N., *J. Heat Transfer*, **104**, 602 (1982).

[102] Coppalle, A. and Vervisch, P., *Combust. Flame*, **49**, 101 (1983).

[103] Soufiani, A. and Djavdan, E., *Combust. Flame*, **97**, 240 (1994).

[104] Markstein, G. H., *Fifteenth Symposium (Intl.) on Combustion*, The Combustion Institute, Pittsburgh, pp 1285 (1974).

[105] Yuen, W. W. and Tien, C. L., *Sixteenth Symposium (Intl.) on Combustion*, The Combustion Institute, Pittsburgh, pp 1481 (1976).

[106] Dalzell, W. H. and Sarofim, A. F., *J. Heat Transfer*, **91**, 100 (1969).

[107] Brosmer, M. A. and Tien, C. L., *Combust. Sci. Technol.*, **51**, 21 (1987).

[108] Felske, J. D. and Tien, C. L., *Combust. Sci. Technol.*, **7**, 25 (1973).

[109] Howell, J. R. and Perlmutter, M., *J. Heat Transfer*, **86**, 116 (1964).

[110] Steward, F. R. and Cannon, P., *Int. J. Heat Mass Transfer*, **14**, 245 (1971).

[111] Lockwood, F. C. and Shah, N. G., *Eighteenth Symposium (Intl.) on Combustion*, The Combustion Institute, Pittsburgh, pp 1481 (1981).

[112] Koch, R., *Berechnung des mehrdimensionalen spektralen Strahlungswärmeaustausches in Gasturbinen-Brennkammern: Entwicklung und Überprüfung von grundlagenorientierten Ansätzen und Methoden*, Dissertation, Universität Karlsruhe (1992).

[113] Fiveland, W. A., *J. Heat Transfer*, **106**, 699 (1984).

[114] Jamaluddin, A. S., Smith, P. J., *Combust. Sci. Technol.*, **59**, 321 (1988).

[115] Selçuk, N. and Kayakol, N., *Int. J. Heat Mass Transfer*, **40**, 213 (1997).

[116] Jamaluddin, A. S., Smith, P. J., *Combust. Sci. Technol.*, **62**, 173 (1988).

[117] Adams, B. R. and Smith, P. J., *Combust. Sci. Technol.*, **88**, 293 (1993).

[118] Lathrop, K. D. and Carlson, B. G., *Discrete Ordinates Angluar Quadrature of the Neutron Transport Equation*, Los Alamos National Laboratory Report LA-3186 (1965).

[119] Carlson, B. G. and Lathrop, K. D., *Transport theoty - the method of discrete ordinates*, in *Computing Methods in Reactor Physics*, H. Greenspan, C. N. Kelber and D. Okrent (Eds.), Gordon and Breach Science Publishers (1968).

[120] Hirt, C. W., Amsden, A. A. and Cook, J. L., *J. Comput. Phys.*, **14**, 227 (1974).

[121] Patankar, S. V., *Numerical Heat Transfer and Fluid Flow*, Hemisphere Publishing Corporation (1980).

[122] Reitz, R. *Personal Communication*, Engine Research Center, University of Wisconsin (1999).

[123] Bi, Hongfeng and Agrawal, A., *Combust. Flame*, **113**, 289 (1998).

[124] Selçuk, N., *J. Heat Transfer*, **107**, 648 (1985).

Acknowledgements

I would like to thank the following persons who made this work possible:

Prof. Dr. Dr. h.c. Jürgen Warnatz for accepting me in his research group and for giving me the opportunity to work on this interesting and challenging topic.

Prof. Dr. Bernhard Schramm for his interest in my work and for agreeing to be my examiner.

Prof. Dr. Rolf Reitz from the Engine Research Center, University of Wisconsin-Madison, for providing experimental data for the Caterpillar engine to compare my simulations with.

The Graduiertenkolleg "Modellierung und Wissenschaftliches Rechnen in Mathematik und Naturwissenschaften" for their financial support.

Privatdozent Dr. Frank Behrendt for his support and advice.

Dr. Miles Elsden for answering all my initial questions regarding the KIVA code.

Dipl.-Ing. Holger Niemann and Dipl.-Phys. Berthold Schramm for their advice and help with the ILDM code.

Dipl.-Ing. Stefan Kleditzsch for solving all my computer-related problems.

All the other people in the group Reaktive Strömung at the IWR for their friendship and help.

My parents and family for their (long-distance) support and Andreas Fechtenkötter for his (short-distance) support.

Erklärung:

Hiermit versichere ich, daß ich die Arbeit selbständig verfaßt und keine anderen als die angegebenen Quellen und Hilfsmittel verwendet habe.

Heidelberg, den

Chrys Correa